# On the Behaviour of Porcine Adipose and Skeletal Muscle Tissues under Shock Compression

**James Michael Wilgeroth**

Department of Engineering and Applied Science,

Cranfield Defence and Security, Cranfield University

Submitted for the Degree of Doctor of Philosophy

# Abstract

The response of porcine adipose and skeletal muscle tissues to shock compression has been investigated using the plate-impact technique in conjunction with manganin foil pressure gauge diagnostics. This approach has allowed for measurement of the levels of uniaxial stress imparted to both skeletal muscle and rendered adipose tissue by the shock. In addition, the lateral stress component generated within adipose tissue during shock loading has also been investigated. The techniques employed in this study have allowed for equation-of-state relationships to be established for the investigated materials, highlighting non-hydrodynamic behaviour in each type of tissue over the range of investigated impact conditions. While the adipose tissue selected in this work has been shown to strengthen with impact stress in a manner similar to that seen to occur in polymeric materials, the skeletal muscle tissues exhibited a flow strength, or resistance to compression, that was independent of impact stress. Both the response of the adipose material and tested skeletal muscle tissues lie in contrast with the shock response of ballistic gelatin, which has previously been shown to exhibit hydrodynamic behaviour under equivalent loading conditions.

Plate-impact experiments have also been used to investigate the shock response of a homogenized variant of one of the investigated muscle tissues. In the homogenized samples, the natural structure of skeletal muscle tissue, i.e. a fibrous and anisotropic composite, was heavily disrupted and the resulting material was milled into a fine

2

paste. Rather than matching the response of the unaltered tissues, the datapoints generated from this type of experiment were seen to collapse back on to the hydrodynamic response predicted for skeletal muscle by its linear equation-of-state ($U_s = 1.72 + 1.88u_p$). This suggests that the resistance to compression apparent in the data obtained for the virgin tissues was a direct result of the interaction of the shock with the quasi-organized structure of skeletal muscle.

A soft-capture system has been developed in order to facilitate post-shock analysis of skeletal muscle tissue and to ascertain the effects of shock loading upon the structure of the material. The system was designed to deliver a one-dimensional, flat-topped shock pulse to the sample prior to release. The overall design of the system was aided by use of the non-linear and explicit hydrocode ANSYS® AU-TODYN. Following shock compression, sections of tissue were imaged using a transmission electron microscope (TEM). Both an auxetic-like response and large-scale disruption to the I-band/Z-disk regions within the tissue's structure were observed. Notably, these mechanisms have been noted to occur as a result of hydrostatic compression of skeletal muscle within the literature.

# Acknowledgements

Firstly, I would like to thank my family for their loving support and for allowing me the opportunity to achieve the goals that I set myself in life. Secondly, I would like to thank Lauren for all the advice, companionship, and love that she has given me over the past few years - it has certainly helped me to focus and remain *compos mentis* whilst working towards my Doctorate. Finally, I extend my deepest thanks and appreciation to Paul and Gareth for all of the professional support and guidance that they have given me during the course of my research.

# Contents

# List of Tables

# List of Figures

## Nomenclature

$U_s$ - shock velocity

$u_p$ - particle velocity

P - pressure

V - volume

E - energy

$\lambda$ - wavelength

c - speed of sound in a given medium

$\rho$ - density

T - temperature

u - velocity

$P_0$ - initial pressure

$\rho_0$ - initial density

$E_0$ - initial energy

$U_0$ - initial shock velocity

$u_0$ - initial particle velocity

$V_0$ - initial volume

Z - shock impedance

$\sigma$ - stress

$\sigma_x$ - longitudinal stress

$\sigma_y$ - lateral stress

$C_0$ - bulk sound speed

S - slope of principal ($U_s$-$u_p$) Hugoniot

$C_L$ - longitudinal wave speed

$C_s$ - shear wave speed

K - bulk modulus

E (elastic constant calculations) - modulus of elasticity

$\nu$ - Poisson's ratio

G (elastic constant calculations) - shear modulus

$V_{imp}$ - velocity of impactor

$dR_i$ - relative change in resistance

$Y_g$ - yield surface of manganin

$\epsilon_v$ - volumentric strain

$\Delta R$ - relative change in resistance

$R_0$ - initial resistance

$\mu_m$ - Poisson's ratio of matrix material

$M_m$ - longitudinal modulus of matrix material

$M_g$ - longitudinal modulus of lateral gauge element

$G_g$ - shear modulus of lateral gauge element

f - frequency

h - Planck's constant

$m_e$ - electronic mass

F - force

B - flux density (strength of magnetic field)

V (electromagnetic calculations) - voltage

$\epsilon$ - strain

$\dot{\epsilon}$ - strain-rate

A (Johnson-Cook strength model) - yield strength at zero plastic
strain

B (Johnson-Cook strength model) - strain hardening constant

n (Johnson-Cook strength model) - strain hardening exponent

C (Johnson-Cook strength model) - strain rate constant

$T_H$ (Johnson-Cook strength model) - homologous temperature

m (Johnson-Cook strength model) - thermal softening exponent

T (Johnson-Cook strength model) - temperature

$T_m$ (Johnson-Cook strength model) - temperature of material

$\epsilon_p$ (Johnson-Cook strength model) - equivalent plastic strain

$\dot{\epsilon}_p$ (Johnson-Cook strength model) - plastic strain-rate

# Chapter 1

# Introduction

## 1.1 Background

The response of the body's soft tissues and of tissue simulants to compression has long been an area of interest within the scientific community. There is an ongoing requirement to more deeply understand the physical response of soft tissues/tissue simulants during high speed impact events such as contact sports, automotive collisions, and insult from ballistic injury (e.g. the effect of blast waves upon the human body). Consequently, this area remains topical today. Undertaking impact experiments of this nature within the laboratory, however, is an inherently complex process. In addition, due to the type of experimental apparatus and diagnostics that are typically required, these trials are often expensive. As such, there is a strong drive towards simulation (where possible). It is vital that the response of soft tissues to dynamic loading conditions be understood in order to develop or improve upon hydrocode simulations of these types of impact events.

The two main advantages of simulating impact/dynamic loading

upon the body are: (i) flexibility, i.e. the ability to model a wide range of impact conditions/dynamic scenarios, and; (ii) the minimal ethical implications that are promoted as a result of simulated studies. However, numerical simulations are typically only as accurate as the material data that is specified for the modelled parts. Despite this, it seems reasonable to suggest that by gaining accuracy through improved material models and simulations, a number of beneficial outcomes are possible. These may include the development of new mitigation systems and an increase in the levels of protection that may be afforded by the individual. Such developments are of great worth. Consequently, a wide range of research seeking to provide insight into the response of soft tissues to dynamic loading may be found within the literature. In this study, the primary materials of interest were skeletal muscle and adipose tissue. Consequently, the following discussion largely focuses on these materials.

This chapter aims to: (i) introduce the reader to the composition of both skeletal muscle tissue and triglyceride fat; (ii) provide an overview of scientific literature relevant to the discussed cause; (iii) highlight any similarities or differences that may exists between separate research studies, and; (iv) provide rationale to this research project.

## 1.2 Skeletal Muscle Tissue

Skeletal muscle tissue is responsible for locamotion, facial expressions, respiratory motions, and is, to a large degree, voluntary in function. It is also known as striated muscle, due to its striated or 'banded' appearance when stained sections of the tissue are viewed through a light microscope. While the percentage mass of skeletal muscle may vary from person to person, it is a major constituent ($\sim$40 % by mass [1]) of the human body. As such, the response of skeletal muscle (of bovine, porcine, and human origin) to compression at various rates of strain has been an area of great interest within the scientific community. High strain-rate compression studies have sought to provide insight into the effects of impact events such as automotive crashes and sports injuries on the body. Further, the data obtained from these high-rate studies is often used to provide more accurate models and simulations of such collision events. A review of the research that has been conducted on the compressive response of skeletal muscle is presented in Section 1.3.

### 1.2.1 Structural Composition

Skeletal muscle tissue is essentially composite in nature, comprising three main elements. These are: (1) protein-based fibres, with each fibre comprising smaller myofibrils and yet smaller actin and myosin myofilaments; (2) connective tissues, i.e. the epimysium, endomysium,

and perimysium, and; (3) a fluid layer, itself composed of a cellular fluid known as sarcoplasm. In addition, blood vessels and nerve cells are interwoven into the tissue network. Figure 1.1 [2] highlights both the structural complexity of a skeletal muscle and the lack of homogeneity in its composition. These attributes contrast with the uniform and intimately mixed make-up of tissue simulants, such as gelatin and ballistic soap, which are often used to represent the body during ballistic and high-strain rate experiments.

One of the early pioneers of research into the cellular and structural composition of skeletal muscle tissue was Huxley [3, 4]. Huxley was one of the first to identify that skeletal muscle is comprised largely of two proteins, actin and myosin, and that neither of these proteins extends continuously along the complete length of the muscle. Adoption of phase-contrast/interference light microscopy techniques allowed Huxley to identify that each protein is organised into separate filaments, each of which were further arranged in overlapping arrays. It was this discovery that first highlighted the banded or 'striated' appearance of skeletal muscle under the light microscope. Using conventional techniques, light micrographs of thin sections of muscle (a requirement for transmission through cellular structures) appear translucent and provide no real insight into the structure of the tissue. However, the contrasting techniques employed by Huxley and Hanson [4] gave early explanation of the contraction mechanism of skeletal muscle tissue - a mechanism that was validated upon the discovery of the existence of cross-bridges between actin and myosin filaments.
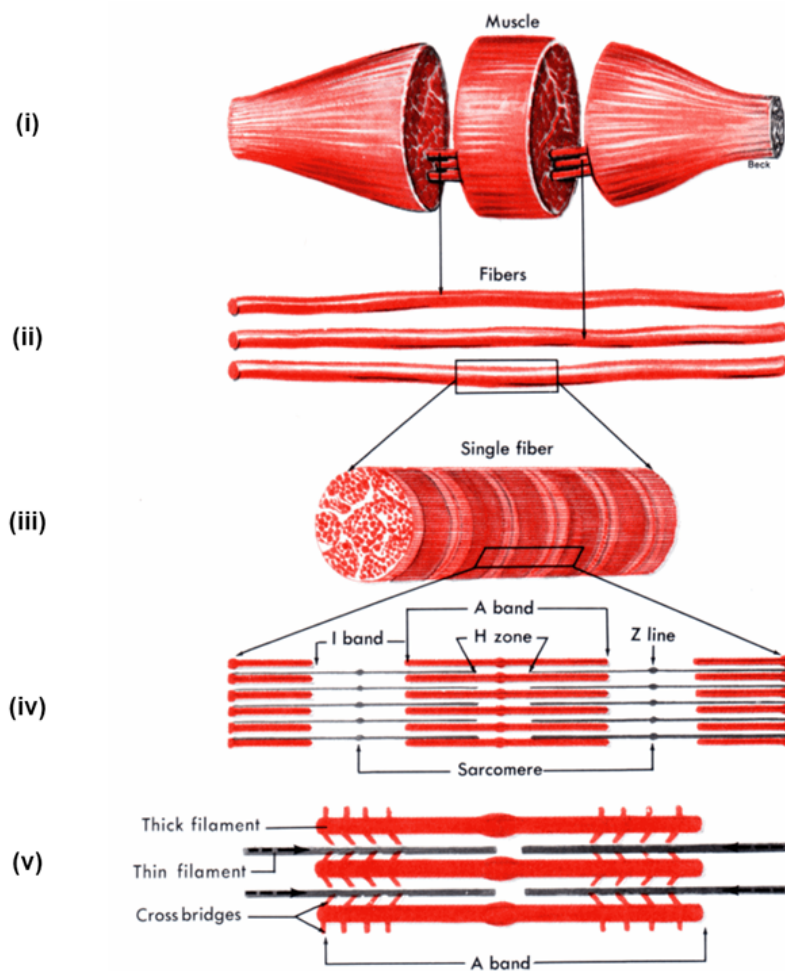
Figure 1.1: Skeletal muscle structure:

**(i)** Skeletal muscle - comprised of individual fibres;

**(ii)** Individual fibres (enlarged);

**(iii)** Increased magnification of a single muscle fibre - showing myofibrils and straited appearance;

**(iv)** Increased magnification of an individual myofibre - highlighting that the striated appearance of muscle fibres is due to overlapping of the thick and thin myofilaments (A-bands appear dark, I-bands appear light);

**(v)** Increased magnification of myofilaments - showing cross-bridges.

[2]

Myofibrils are typically 1-3 $\mu$m in diameter and the actin and myosin myofilaments that comprise the myofibril are typically 8 and 12 nm in diameter, respectively [1]. During muscle contraction, energy is provided to the cross-bridges that exist between the actin and myosin myofilaments by adenosine triphosphate (ATP). This causes a power stroke in which the ratchet-like motion of the cross-bridges slide the myofilaments past one another. This acts to shorten the sarcomere, i.e. the functional unit of muscle contraction, and hence the length of the muscle fibres. This process is known as the sliding filament model [4, 5]. Under the light microscope, separation of the striations, or 'bands', observed in contracted tissue is lesser than in relaxed tissue. This is due to increased overlapping of the myofilaments, thus reducing the size of the (light) I-band region (see Figure 1.1).

The fibrous components of muscle tissue are bound by many connective tissues. The overall trunk of a skeletal muscle is bound by a dense layer of connctive tissue known as the deep fascia. The deep fascia acts in combination with an underlying layer of tissue (the epimysium) to confine each individual muscle. Within the muscle there exist sub-units called fascicles, each of which are surrounded by a sheath of connective tissue known as the perimysium. Fascicles contain bundles of muscle fibres. These fibres are further separated from one another by sheaths of connective tissue called the endomysium. The epimysium, perimysium, and endomysium all work together to provide a framework that supports and holds the muscle together. As was previously mentioned, blood-containing vessels (e.g. arteries, veins, cap-
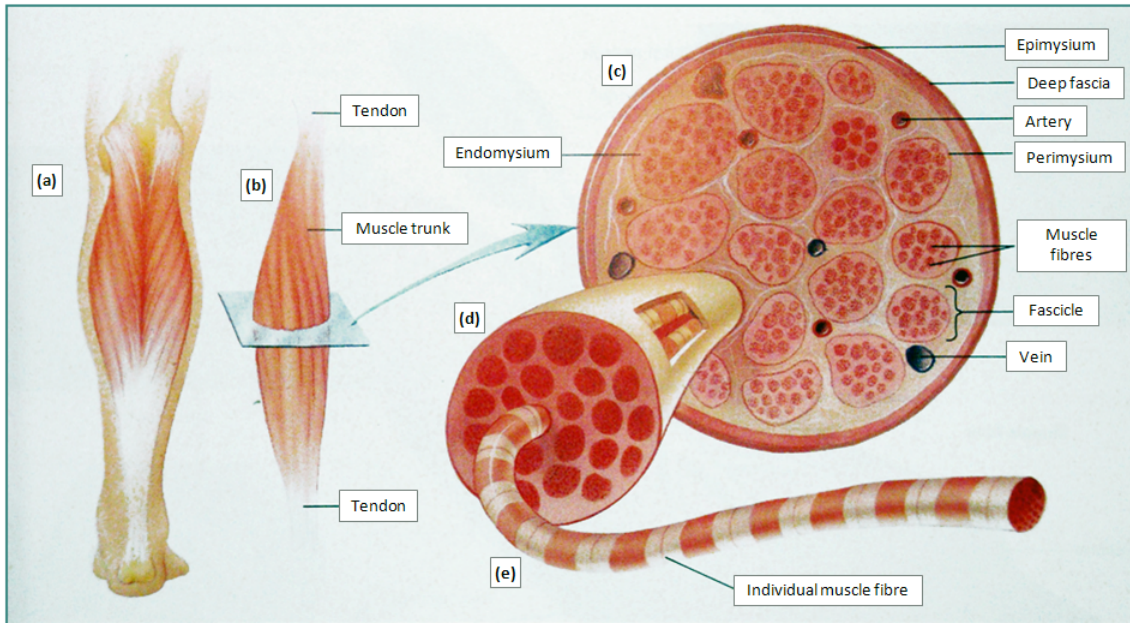
Figure 1.2: Structure of a skeletal muscle
(taken from [2])

illaries) and nerves are interwoven into the tissue matrix. These all
pass through the layers of connective tissues within a muscle, provid-
ing nutrients and the nerve impulses that control muscle contraction
[2]. Figure 1.2 illustrates the structure of a skeletal muscle in trans-
verse orientation, i.e. end-on.

## 1.3 The Dynamic Behaviour of Skeletal Muscle

McElhaney [6] looked at the response of bovine muscle tissue when impacted by an air-driven piston. His conclusions related the cellular structure of the muscle to humped regions witnessed in the stress-strain curve of the material at specific strain rates, suggesting that, as strain increases, inhibition of fluid movement between cells and the interstitial spacing between them eventually lead to cell rupture and the observed incongruities in the stress-strain response.

Saraf et al. [7] used Split-Hopkinson Pressure Bar (SHPB) methods to investigate the dynamic bulk and shear response of tissues removed from the stomach, heart, liver, and lungs of cadavers. The SHPB typically allows for strain rates of $10^3$-$10^4$ s$^{-1}$ to be investigated and was used by Saraf et al. to construct linear stress-volumetric strain relationships and calculate bulk moduli for their investigated materials. Results from dynamic shear experiments were presented as a series of highly non-linear shear stress-shear strain curves, highlighting the strain-rate-dependent response of soft biological tissues.

Song et al. [8] investigated the effect of fibre alignment upon the dynamic response of muscle tissue at similar strain-rates to those investigated by Saraf et al. [7]. These authors made use of a modified SHPB apparatus to investigate both the dynamic and quasi-static compressive response of porcine muscle tissue. Use of annealed copper disks and tubes by Song et al. allowed for: (i) minimisation of radial inertia effects; (ii) dynamic stress equilibrium, and; (iii) a near constant rate of compression. Additionally, Song et al. sought to

form their samples of muscle tissue into annular disks. This approach further reduced the effects of radial inertia, which have been seen to occur within other soft, non-shaped sample materials under high-rate axial compression, e.g. ballistic gelatin [9].

Van Locke et al. [10] also investigated the effect of fibre orientation, having interrogated the stress-relaxation behaviour of skeletal muscle tissue following compression. These authors suggested that movement of the fluid component of muscle tissue (sarcoplasm) may be easier along, rather than perpendicular to, the direction of the fibres. Thus, during compression in the cross-fibre direction, the fluid is free to re-arrange itself. Conversely, upon compression in the in-fibre direction, the fluid is confined by the connective tissues that surround the fibrous components of the tissue (e.g. the perimysium and endomysium). Essentially, it was suggested that this physical attribute acts to increase material stiffness during compression in the in-fibre direction.

While little work appears to have been conducted regarding the dynamic tensile behaviour of skeletal muscle, Morrow et al. [11] performed low-rate (0.05 % s$^{-1}$) tensile tests upon *extensor digitorum longus* muscles from New Zealand White rabbits. This study into the 'passive' properties of skeletal muscle provided data for the ultimate tensile strength of the selected muscle in both the longitudinal and transverse direction. Results showed that the ultimate tensile stress, and thus longitudinal modulus, of the tissue was significantly greater in the longitudinal direction (163 ± 75.7 KPa) than in the transverse

direction ($27.5 \pm 9.9$ KPa).

## 1.4 Triglycerides/Body Fat

Triglycerides or triacylglycerols are the most common form of fat in the body, accounting for approximately 95 % of all body fat [12], [1]. This type of fat comprises a structure that is essentially a biological polymer - see Figure 1.3 - and serves three main functions within the body. Firstly, if intake exceeds requirement, fat deposits build up within the body. These act as chemical energy stores, allowing energy to be extracted by hydrolysis reactions as and when it is required, e.g. at times when food is scarce. The secondary function of (subcutaneous) fat is as an insulator - preventing heat loss in extreme conditions. Finally, visceral fat, which surrounds the body's vital organs, cushions and provides protection against physical insult.

The chemical structure of triglycerides and the mechanism of their formation is highlighted in Figure 1.3. Via a dehydration reaction, i.e. the removal of water, three fatty acid groups join with one unit of glycerol. Glycerol is a three carbon molecule with a hydroxyl group (-OH) attached to each carbon atom. Fatty acids consist of a straight chain of carbon atoms with a carboxyl group (-COOH) attached at one end. Fatty acids differ from one another in both length and the percentage saturation of their carbon chains. A fatty acid is said to be saturated when only single covalent bonds exist between its carbon atoms. Conversely, a fatty acid is said to be unsaturated when one or
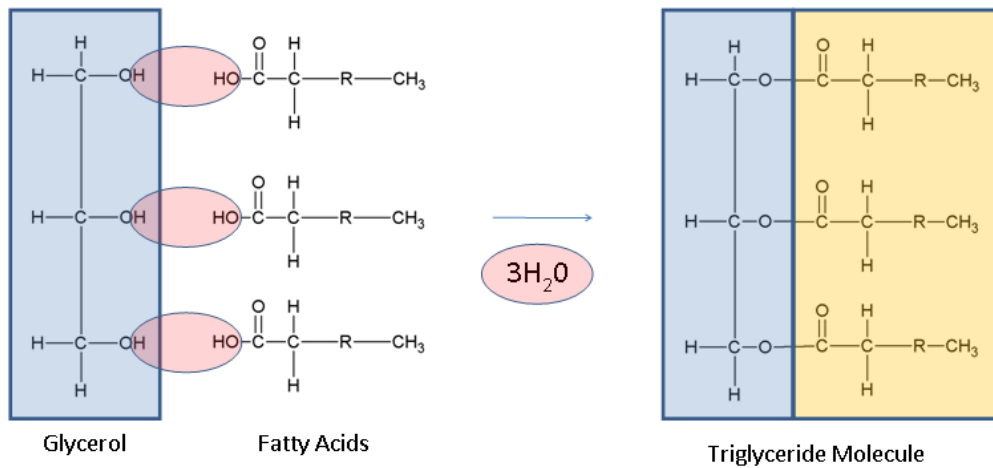
Note: 'R' substitutes a repeating $CH_2$ Carbon chain

Figure 1.3: Trigliceride formation (adapted from [12])

more double covalent bonds exist between any of its carbon atoms. It has been shown elsewhere that it is the percentage saturation of the fatty acids present within a fat type that governs the firmness of the material [13]. Specifically, as the percentage saturation of the fatty acids increases, so too does the firmness of the material (i.e. an increase in measured stress resulted during the compression of samples possessing a higher percentage saturation of fatty acids than those with lower percentage saturation at equal levels of strain).

## 1.5   On the Behaviour of Fatty Tissues

The literature regarding the compressive response of fatty tissues is limited. Quantitative analysis of dynamic loading on the material is also limited. However, Nishioka and Irie [13] did demonstrate that,

under low (strain) rates of compression, the firmness of porcine perirenal fat increases with the percentage of saturated fatty acids within the material. Additionally, Miller et al. [14] performed quasi-static, stress-relaxation, and rapid ($10^2$ s$^{-1}$) compression tests on human calcaneal (heel) fat. These tests allowed for viscoelastic time constants and relaxation coefficients to be established for the tissue. In addition, the calcaneal fat pad exhibited both hyper-elastic and non-linear behaviour over the range of examined loading conditions.

Unlike fatty tissues, the behaviour of polymeric materials during shock loading has been extensively studied. This is useful as the basic structure of triglycerides, or triaglycerols, is that of a biological polymer. Millett and Bourne [15] investigated the shock response of polyethylene, polypropylene, and polystyrene by plate-impact methods and related increasing resistance to shock compression with the complexity of the side chain attachment present within the polymer, i.e. polyethylene to polystyrene. In addition, Carter et al. [16] investigated the dynamic response of various polymeric materials during shock compression to pressures within the range of 20-30 GPa. One of the main findings by Carter et al. was that the U$_s$-u$_p$ (shock-velocity-particle velocity) Hugoniots of all of the investigated polymers extrapolated to higher bulk sound speeds than the values which were measured experimentally using ultrasonics. This behaviour was attributed to both two dimensional compression of the polymeric structure and the form of the inter-chain interaction potential.

## 1.6 The Dynamic Behaviour of Tissue Simulants

The dynamic behaviour of tissue simulants has been investigated most frequently using SHPB apparatus. For example, Kwon et al. [17] used SHPB apparatus incorporating polymeric bars (i.e. PSHPB) to investigate the strain-rate sensitivity of ballistic gelatin to compression. While also looking at the quasi-static response of gelatin, these authors used the PSHPB apparatus to investigate the response of the tissue simulant at rates of strain ranging from 2000 $s^{-1}$ to 3200 $s^{-1}$. The change in compressive strength, i.e. bulk modulus, from 3 KPa at 0.0013 $s^{-1}$ (quasi-static) to 6 MPa at 3200 $s^{-1}$ measured by Kwon et al. was discussed as being related to the shear thickening behaviour of the material. Further the shear-thickening observed at higher rates of strain was argued on the mechanism of hydrocluster formation and differences in internal energy dissipation, which have been suggested to occur within polymer-gels by others [18, 19, 20].

In addition to the investigations by Kwon et al. [17], Salisbury and Cronin [21] also used PSHPB apparatus to investigate the dynamic compressive response of ballistic gelatin. Specifically, these authors examined the response of both 10 and 20 % ballistic gelatin formulations at strain-rates ranging from 1000 - 4000 $s^{-1}$. While the primary aim of the research presented by Sailisbury and Cronin was to validate their PSHPB apparatus as a method for testing low impedance materials at relatively high rates of strain, their results both highlighted the strain-rate dependence of the material and, for the 20 % formulation at lower strain-rates, held agreement with results found elsewhere

[22].

Examples of research into the dynamic behaviour of other polymeric gels than ballistic gelatin are also present within the literature. In particular, research conducted by Moy et al. [9] examined the dynamic behaviour of a number of physically associating gels (PAGs). These gels have been formulated as alternatives to gelatin, which possesses a number of undesirable properties. Namely: (i) its short shelf-life; (ii) its deterioration under prolonged exposure to room temperature, and (iii) the degree of variability in its viscoelasticity which may result from inconsistencies in its formulation [9]. Moy et al. used a pulse-shaping technique to compare the high and low rate compressive response of ballistic gelatin with two separate PAGs. The two PAGs investigated in the study by Moy et al. were both formulated from commercially-available copolymers consisting of polystyrene and polyisoprene. While agreement in terms of the stress-strain response of all three materials (i.e. the ballistic gelatin and the two PAG formulations) was apparent at 2500 s$^{-1}$, a markedly different response was observed between each of the materials at a lower strain-rate of 1 s$^{-1}$. These results suggested that, while possessing more desirable passive properties than ballistic gelatin, the examined PAGs showed a higher strain-rate sensitivity than the frequently employed tissue simulant (gelatin).

## 1.7 Rationale: The Shock Response of Soft Tissues

Despite the range of data available on the compressive response of soft tissues and tissue simulants, there is an apparent paucity of information regarding their response to shock compression. The primary aim of this work was to ascertain the shock response of both porcine adipose and skeletal muscle tissues using the plate-impact technique. The Hugoniot relationships for these materials will be invaluable in future hydrocode simulations seeking to investigate the interaction of shock waves with the body, e.g. numerical simulation of exposure to improvised explosive devices. Following the generation of equation-of-state data, the secondary objective of this work was to develop a soft-capture system that would successfully allow for the recovery of shocked materials. The motivation behind this stemmed from the desire to perform post-shock analysis upon recovered material and to ascertain the effects of shock compression upon its structure.

# Chapter 2

# Shock Waves

## 2.1 Shock Wave Formation

The most common examples of shock waves that are experienced on Earth include the "sonic boom" caused by an aeroplane flying overhead at supersonic speed and the audible crash produced when lightning strikes. These audible events are actually the result of decaying shock waves produced at the source of each disturbance. In essence, shock waves are nature's way of dissipating large amounts of energy in the form of non-linear waves that propagate faster than the speed of sound within a specific medium. In order to describe shock formation, which may occur when an aircraft, for example, travels at a velocity that is greater than the speed of sound in air, we must firstly consider the Doppler effect.

The Doppler effect is a phenomenon that results from the change in frequency of a sound observed by a listener when the constant frequency source ($f_s$) of the sound and the listener are in motion relative to one another [23]. For example, as a car approaches a

stationary observer $(v)$ at a constant velocity $(v_s)$ with its horn sounding, the wave crests of the source are compressed together. This reduces the wavelength of the disturbance, thus increasing the observed frequency - see Equation 2.1. Conversely, as the car passes and moves away from the observer, the wave crests rarefy. This has the opposite effect of increasing the wavelength of the disturbance and reducing frequency observed by the listener - see Equation 2.2. Equation 2.3 expresses the frequency heard by the listener $(f_l)$ in relation to the frequency of the source $(f_s)$, where $(v)$ is wave speed relative to the medium and its wavelength. In Equation 2.3, signs must be chosen to produce an up-shift in observed frequency $(f_l)$ when the source and the receiver are approaching one another, and vice versa.

$$\lambda = \sqrt{\frac{v - v_s}{f_s}} \tag{2.1}$$

$$\lambda = \sqrt{\frac{v + v_s}{f_s}} \tag{2.2}$$

$$f_l = \frac{v \pm v_l}{v \pm v_s} f_s \tag{2.3}$$

As the speed of an object $(v_s)$ approaches the speed of sound $(c)$ in a given medium, e.g. a jet approaching the sound barrier in air, wavelength reduces towards zero and the wave crests pile up on each

other. By substituting $c$ for $v$ in Equation 2.3 we can see that when $v_s \geq c$, i.e. the point at which the source is travelling faster than the speed of sound, $f_l$ becomes infinite. At this point a shock wave is formed.

Glass [24] describes a shock wave as a thin front in which molecular collisions bring about an abrupt change in the state of a gas, from an initial state of low pressure, density, and temperature to a final state in which all of these properties have a markedly higher value. Shock waves, however, are able to propagate not only through gases, but solids, liquids, and plasmas, where the aforementioned (abrupt) changes in the medium associated with this type of propagation remain valid. For a shock wave propagating through air at sea-level, Glass [24] states that the mean free path (average distance travelled by a moving particle between successive collisions) is only c.7 millionths of a centimetre (6.6 x $10^{-6}$ cm). Meyers [25] simply defines a shock wave as a discontinuity in pressure, temperature (internal energy), and density.

Shock waves possess the following two fundamental properties: (i) they are compressive, and; (ii) the flow velocity relative to the shock front is supersonic at the front side and subsonic at the rear side [26]. Compressive disturbances of differing densities ($\rho$) travel with different velocities through a given medium. Specifically, those of higher density propagate faster than disturbances of lesser density.

The example of a self-steepening finite-amplitude wave caused by a single compressive pulse is shown in Figure 2.1. It can be seen

that the density at point A is higher than the density at point B. Thus, point A propagates at a velocity faster than point B through the medium. From this we can also state that each point on the waveform is propagating at local wave speed. Non-linear behaviour causes the change in the shape of the wave seen at 2.1 (b), which might ultimately result in the wave shape seen at (c). This scenario is not physically possible, however. In reality, the result of high energy compression is the formation of an infinitely steep singularity known as a shock wave - seen at 2.1 (d).

Shock waves whose amplitudes lie perpendicular to the plane of propagation within a medium are known as normal shocks (see Figure 2.2). Such shock waves exhibit one-dimensional flow, i.e. the flow-field properties of pressure (P), temperature (T), density ($\rho$), and velocity (u) are functions of the x-coordinate direction only. From Figure 2.1 it can be seen that the propagation of normal shocks promotes two distinct regions within the medium. These are: (i) material ahead of the shock, in which conditions are denoted with the subscript "1", and; (ii) material behind the shock, in which conditions are denoted with subscript "2". The physical processes associated with the propagation of a shock through a material are governed by the equations of conservation of mass, momentum, and energy, which are detailed in Section 2.2.

Shock propagation within solids must account for both the deviatoric and hydrostatic components of stress as, unlike fluids, they are able to sustain shear disturbances. This property promotes a
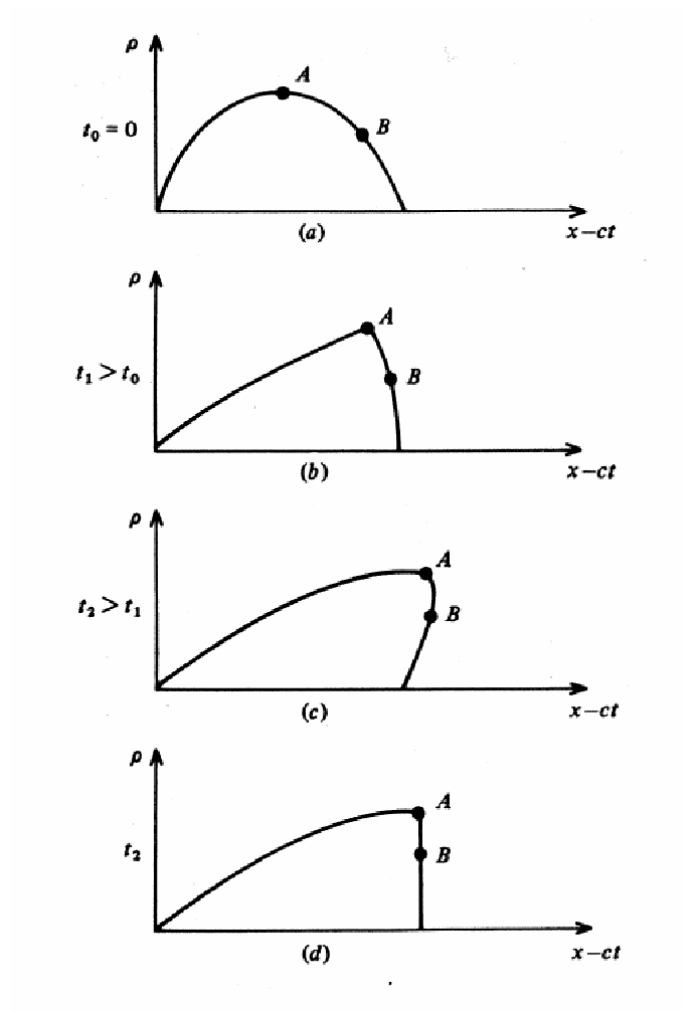
Figure 2.1: Self steepening finite-amplitude wave (taken from [27])

$P_1$
$T_1$
$\rho_1$
$u_1$

$M_1 > 1$

$P_2 > P_1$
$T_2 > T_1$
$\rho_2 > \rho_1$
$u_2 > u_1$

x-direction

$M_2 < 1$

1

2

Given
conditions
ahead of the
shock wave

Normal Shock

Unknown
conditions
behind the
shock wave
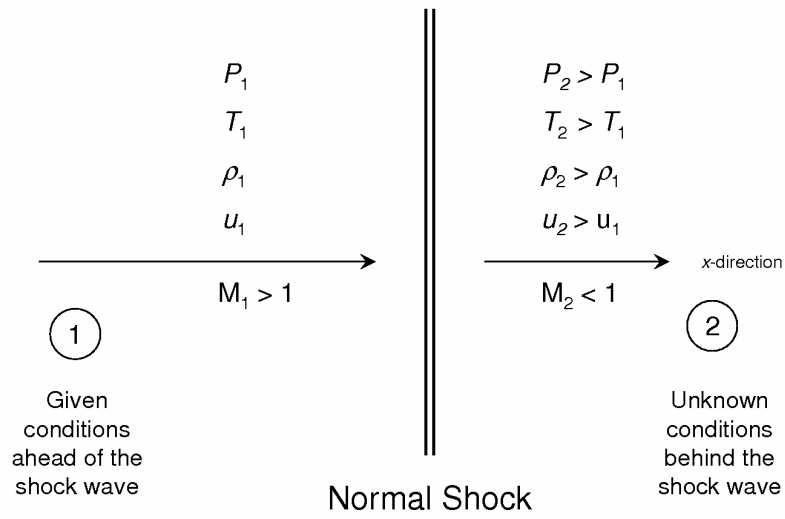
Figure 2.2: Illustrative representation of the conditions both ahead and behind of a normal shock wave (adapted from [28])

resistance to shear i.e. strength. However, magnitudes of hydrostatic stress generated within solids due to shock wave propagation often exceed the deviatoric stress component. In such situations the response of the material is stated as being hydrodynamic, i.e. the material behaves without strength or like fluid.

## 2.2  The Conservation Equations

In their finite difference forms, the Rankine-Hugoniot equations apply to a shock discontinuity such that: (i) the mass of material flowing into the discontinuity is equal to the mass flowing out; (ii) the rate of change of momentum of the stream is equal to the pressure, and; (iii) the change in energy of the stream is equal to the work done [29]. Essentially, the conservation equations govern the propagation of shock waves in compressible fluids [28], [25], [30]. These equations, or 'jump conditions', are best described using the example of a piston moving into a cylinder containing a compressible fluid (see Figure 2.3).

In Figure 2.3 conditions of pressure, density, energy, and shock velocity ahead of the shock are $P_0$, $\rho_0$, $E_0$, and $U_0$, whilst the corresponding conditions behind the shock are denoted by P, $\rho$, E, and $U_s$. At time t = $t_0$ the piston is at rest, after which it is pushed into the compressible fluid, which is initially at pressure $P_0$, density $\rho_0$ and having internal energy $E_0$. The velocity at which the piston is pushed into the compressible fluid is $u_p$.

After time t = $t_1$ the piston has moved a distance $u_p t_1$ into the compressible fluid, resulting in propagation of a shock by a distance of $(U_s\text{-}u_p)t_1$ ahead of the piston. This compressed region has pressure P and density $\rho$ . Various models of shock motion exist to describe the movement of a shock front away from the compressive source responsible for its generation; the most common of which is that of a snow plough. If a snow plough moves at a velocity equal to $u_p$, the packed snow ahead of it also moves at a velocity $u_p$. Given this, the
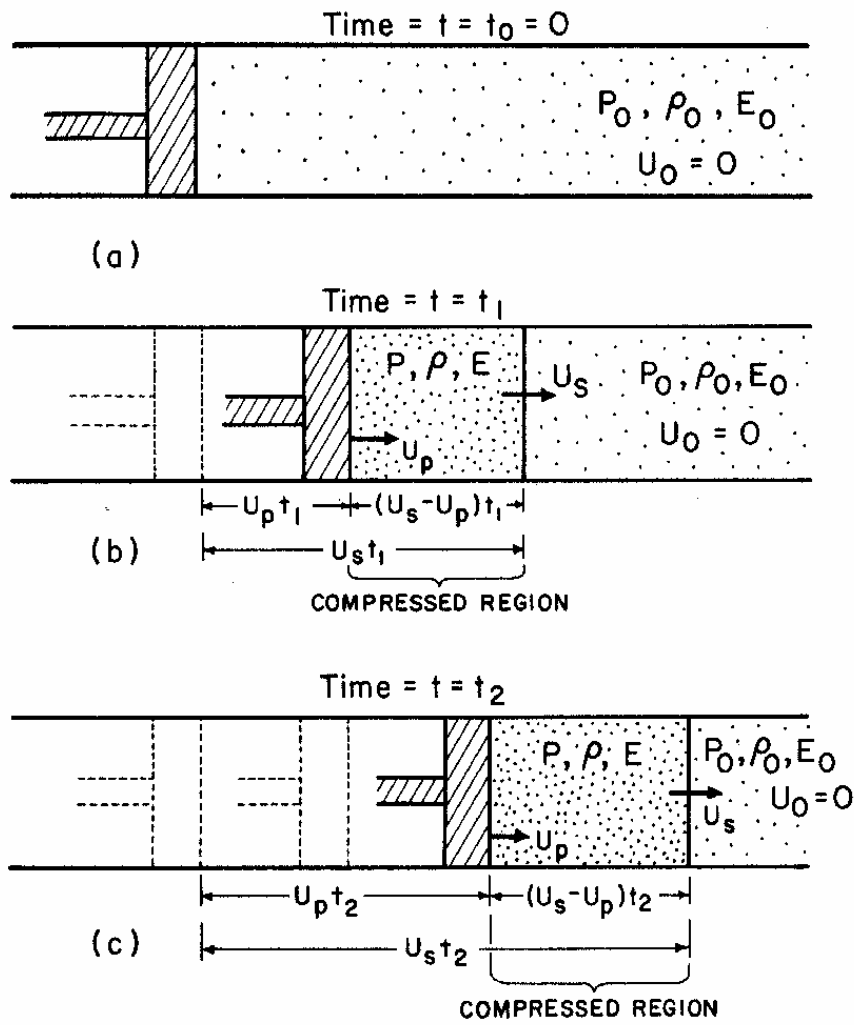
Figure 2.3: Successive positions of an idealized piston moving into a cylinder containing a compressible fluid [25]

continuous addition of snow to the packed region dictates that the fresh snow will travel at a greater velocity $(U_s)$ than the velocity of the vehicle $(u_p)$. Thus, the velocity of the shock is always greater than that of the particle velocity within compressible materials.

### 2.2.1 Conservation of Mass

In Figure 2.3 material enters the shock front, which is propagating at speed $U_s$. From this it can be shown that the mass of material entering the shock is given by $\rho_0 A U_s dt$, where A is the cross-sectional area of the shock and $\rho_0$ is the initial density of the material. Similarly, the mass leaving the shock is given by $\rho_0 A(U_s\text{-}u_p)dt$. This conservation of mass across the discontinuity is expressed by Equations 2.4 and 2.5. Equation 2.4 is the finite difference form of the conservation of mass.

$$\delta(\rho U_s) = 0 \tag{2.4}$$

$$\rho_0 U_s = \rho(U_s - u_p) \tag{2.5}$$

Notably, the un-shocked fluid may not be at rest but travelling at an initial velocity $u_0$. In this case, the conservation of mass across a shock is

$$\rho_0(U_s - u_0) = \rho(U_s - u_p) \tag{2.6}$$

## 2.2.2 Conservation of Momentum

Momentum is defined as the product of mass and velocity. Conservation of momentum requires that the rate of change of momentum within a system is equal to the rate of change of impulse across the shock.

$$Impulse = Fdt = (PA - P_0A)dt \qquad (2.7)$$

Change in momentum equals

$$(momentum)_1 - (momentum)_0 = \rho A(U_s - u_p)u_p dt \ldots$$
$$-\rho_0 A(U_s - u_0)u_0 dt \qquad (2.8)$$

Equating change in momentum with impulse, we obtain

$$\rho A(U_s - u_p)u_p dt - \rho_0 A(U_s - u_0)u_0 dt = (PA - P_0A)dt \qquad (2.9)$$

This can be further simplified to either

$$\rho(U_s - u_p)dt u_p - \rho_0(U_s - u_0)dt u_0 = (P - P_0)dt, \qquad (2.10)$$

or

$$\rho(U_s - u_p)u_p - \rho_0(U_s - u_0)u_0 = (P - P_0) \qquad (2.11)$$

From the conservation of mass (Equation 2.20) we know that $\rho_0 U_s$ = $\rho(U_s\text{-}u_p)$. Thus,

$$\rho_0(U_s - u_0)(u_p - u_0) = (P - P_0) \qquad (2.12)$$

Hence, if $u_0$=0

$$(P - P_0) = \rho_0 U_s u_p \qquad (2.13)$$

The relationship is the equation for the conservation of momentum, where $\rho_0 U_s$ is the shock impedance $(Z)$.

## 2.2.3   Conservation of Energy

Energy can neither be created nor destroyed, only converted from one form to another. From this physical law, the conservation of energy across a shock is defined such that the work done by the pressure from $P_0$ to P is equal to the difference in total energy (kinetic plus internal) across the shock front. The difference in work done is given by:

Work done by the pressure $(\delta W)$ = $(PA)(u_p \; dt)$ - $(P_0A)(u_0 \; dt)$

Mass into the shock per unit time = $\rho_0 A(U_s\text{-}u_0)$

Kinetic Energy (KE) acquired per unit time = $\frac{1}{2}\rho_0 A(U_s\text{-}u_0)u_0^2$

However, the same applies behind the shock. Thus, the change in kinetic energy across the shock per unit time equals

$$\frac{1}{2}\rho A(U_s - u_p)u_P^2 - \frac{1}{2}\rho_0 A(U_s - u_0)u_0^2 \qquad (2.14)$$

and the change in total energy per unit time equals

$$[(\frac{1}{2}\rho A(U_s-u_p)u_p^2 + E A\rho(U_s-u_p)) - (\frac{1}{2}\rho_0 A(U_s-u_0)u_0^2 + E_0 A\rho_0(U_s-u_0))]$$
$$(2.15)$$

Equating work done ($\delta$W) to the difference in total energy ($\delta$E) and taking $u_0 = 0$ gives either

$$PAu_p - \frac{1}{2}\rho A(U_s - u_p)u_p^2 + EA\rho(U_s - u_p) - E_0 A\rho_0(U_s) \qquad (2.16)$$

or

$$Pu_p = \frac{1}{2}\rho(U_s - u_p)u_p^2 - E_0\rho_0 U_s + E\rho(U_s - u_p) \qquad (2.17)$$

However, from the principle of conservation of mass (Equation 2.20) we know that $\rho_0 U_s = \rho(U_s - u_p)$ . Substituting this into the above gives

$$Pu_p = \frac{1}{2}\rho_0 U_s u_p^2 - E_0\rho_0 U_s + E\rho U_s \qquad (2.18)$$

or

$$Pu_p = \frac{1}{2}\rho_0 U_s u_p^2 + \rho_0 U_s(E - E_0) \qquad (2.19)$$

**In summary, the conservation equations are:**

Conservation of mass:

$$\rho_0 U_s = \rho(U_s - u_p) \tag{2.20}$$

Conservation of momentum:

$$(P - P_0) = \rho_0 U_s u_p \tag{2.21}$$

Conservation of energy

$$P u_p = \frac{1}{2}\rho_0 U_s u_p^2 + \rho_0 U_s (E - E_0) \tag{2.22}$$

## 2.3 Planar Shocks in Materials

This thesis directly explores the propagation of shock waves within biological tissues, i.e. solids. Consequently, it is necessary that the fundamentals of shock wave propagation within materials be understood. This section highlights; (i) a brief historical overview of the development of shock wave theory; (ii) the mathematics involved in planar shock wave propagation, and; (iii) the type of material data that one may begin to obtain through shock wave experiments.

A concise, historical account of the development of non-linear flow, i.e. shock wave theory, is provided by Courant [30]. Evidence suggests that Riemann (1860) was one of the earliest to develop the theory of shock waves. However, it appears that he incorrectly assumed that the transition across a shock was both adiabatic and reversible. Rankine (1860) clearly presented accurate forms of the conservation equations for mass, momentum, and energy for normal shocks (see Figure 2.2 in Section 2) in his paper titled "On the Thermodynamic Theory of Waves of Finite Longitudinal Disturbance", which was published in the Philosophical Transactions of the Royal Society [28]. Rankine also correctly assumed that shocks are not an isentropic/adiabatic process but rather regions of dissipation in which heat is communicated from one particle to another. This discovery henceforth defined the shock as an irreversible process.

Hugoniot (1887) showed that entropy across a shock must change for the law of conservation of energy to apply, successfully relating the thermodynamic properties across a shock (see Equation 2.25). From

the second law of thermodynamics, Lord Rayleigh (1910) further developed the work of Hugoniot surmising that, as entropy increases across a shock, rarefaction shocks are not physically possible. Thus, the Rankine-Hugoniot relations apply only to compressive shocks in which the pressure behind the shock is always greater than the pressure ahead of it.

The conservation equations (outlined in Section 2.2) are fundamental to understanding the propagation of shock waves within fluids, i.e. materials behaving without strength. However, they do not contain any information about the behaviour of the material itself under shock conditions. In order to understand material behaviour under one-dimensional (1D) shock conditions, the Rankine-Hugoniot Equations must be employed. These equations denote the physical states of the material both ahead and behind the shock and thus its response to the propagating wave. Notably, there are five key shock parameters that we must consider in order to define the behaviour of the shocked material. These are; shock velocity ($U_s$), particle velocity ($u_p$), pressure (P), density ($\rho$), and internal energy (E). Additionally, volume (V) may also be considered. The Rankine-Hugoniot equations conveniently allow that only two of the five key shock parameters be known in order to derive the three remaining unknowns. Useful forms of the Rankine-Hugoniot Equations are provided by Equations 2.23, 2.24, and 2.25, in which un-subscripted terms denote conditions behind the shock and subscripted terms denote conditions ahead of the shock.

$$U_s^2 = V_0^2 \frac{P - P_0}{V_0 - V} \tag{2.23}$$

$$u_p = \frac{P - P_0}{\rho_0 U_s} = [(P - P_0)(V_0 - V)]^{\frac{1}{2}} \tag{2.24}$$

$$E - E_0 = \frac{1}{2}(P + P_0)(V_0 - V) \tag{2.25}$$

Equations 2.23 and 2.24 give both the dynamic and thermodynamic quantities associated with the propagation of the shock within a material, while Equation 2.25 relates to the thermodynamic properties alone. Additionally, as energy is a function of pressure and volume alone, Equation 2.25 defines the P-V Hugoniot curve of a shocked material from an initial given state $P_0$, $V_0$. Essentially, this Hugoniot is the locus of all P-V states attainable by a single shock transition from the initial state.

Figure 2.4 shows the schematic for a P-V Hugoniot relationship and also includes both the isentropic form of compression (i.e. without heat addition) and the release isentrope, which occurs after shock compression. It can be seen that as volume decreases, the Hugoniot climbs above the isentrope. Thus, for a given decrease in specific volume, a shock creates a higher pressure increase than isentropic compression. Usefully, Figure 2.4 shows the difference between the assumption made by Riemann, i.e. the existence of the shock as a reversible process, and the correct assumption made by both Rankine
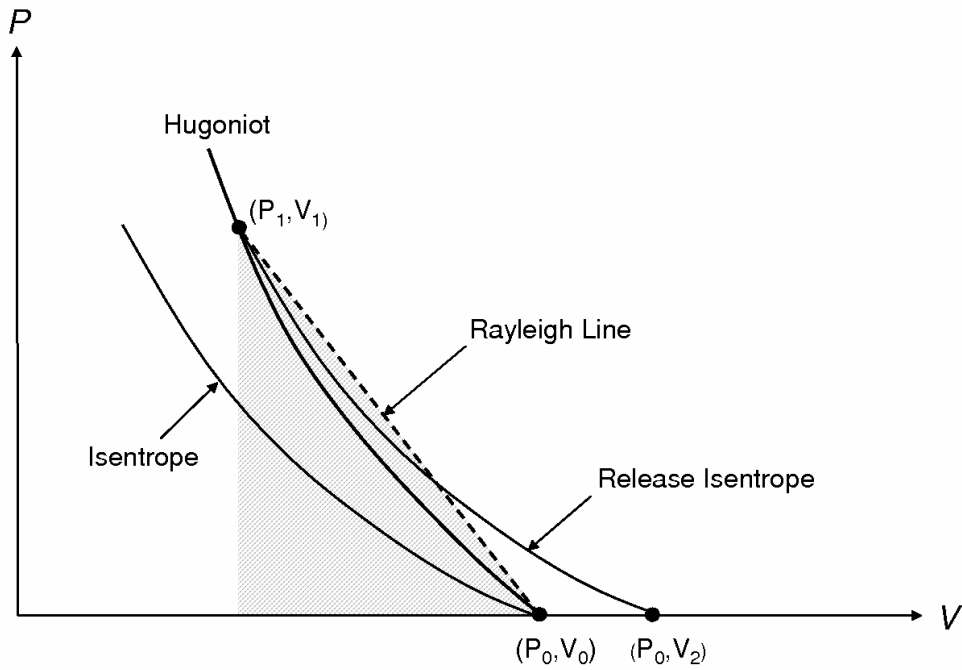
Figure 2.4: The Pressure-Volume Hugoniot Plane (adapted from [26])

and Hugoniot, which correctly defines the shock as a non-adiabatic and irreversible process. Pressure, density, entropy, and temperature are always greater behind the shock front than ahead of it. The degree to which these properties are seen to increase is directly linked to the intensity of the shock.

The Rayleigh line $(U_s \rho_0)^2$ is the straight line between the initial $(P_0, V_0)$ and the final $(P_1, V_1)$ shocked state of a material. Skidmore [29] noted two important attributes of the Rayleigh line. Firstly, he noted that the change in internal energy across a shock is equal to the area below the Rayleigh line (i.e. Equation 2.25). This satisfies that energy is conserved across the discontinuity. Secondly, he noted that the adiabat through the shocked state $P_1$, $V_1$ passes between both the Hugoniot and the Rayleigh line, thus determining that C + u > U >

$C_0$ (where C is the velocity of sound relative to material moving with a particle velocity u, U is the shock velocity, and $C_0$ is the bulk sound speed). This essentially dictates that shock waves are supersonic with respect to the material ahead of them and subsonic with respect to the material behind.

The Equation-of-State (EoS) for a material subjected to one-dimensional shock is provided by Equation 2.26. Here, $C_0$ is the sound velocity within the material at zero pressure, i.e. the minimum wave velocity required for shock propagation; $U_s$ and $u_p$ are the shock and particle velocities, respectively; and S determines the gradient of the relationship between the shock and particle velocities.

$$U_s = C_0 + Su_p \qquad (2.26)$$

Typically, the EoS of a shocked material is represented by a linear curve in the $U_s$-$u_p$ or 'principal' Hugoniot, although regions of non-linearity may be observed in some materials. Non-linear response may result from a phase change within a shocked material or due to shock-induced interactions within the material's structure, such as the coalescence of particles within a mixture or the collapse of porous spacings. Additionally, non-linear response may relate in a particular manner to the nature of the atomic bonds present within the material (e.g. covelant, ionic, hydrogen, disulphide, etc.). For materials that exhibit non-linear response, e.g. polymeric materials at low particle

velocities [31], [16], the function of the EoS becomes polynomial, i.e. $U_s = C_0 + S_1 \, u_p + S_2 \, u_p^2...$ Significantly, the EoS is unique for a given material and may provide useful information about its behaviour under shock conditions.

The sound speed ($C_0/C_B$) of a material may be calculated from measured longitudinal ($C_L$) and shear wave ($C_S$) velocities at zero shock pressure (1 atm) using Equation 2.27. Given the influence of both bulk modulus (K) and density ($\rho$) upon the sound speed of a material (see Equation 2.28), it is unsurprising that the linear intercept ($C_0$) of the equation-of-state for type 304L steel within the $U_s$-$u_p$ plane presents a significantly higher value than the corresponding linear intercept for Perspex (4.55 and 2.22 mm/$\mu$s, respectively). The process of determining the bulk sound speed from measured longitudinal and shear wave velocities is useful as it provides an indication of the shock velocity at zero particle velocity, i.e. the minimum velocity at which a shock can exist within a particular material. This, however, is not always the case and examples of materials in which this principle is not maintained are discussed at the end of this section. Longitudinal ($C_L$) and shear ($C_s$) wave velocities for a material may be calculated using Equations 2.29 and 2.30, respectively: where E is the modulus of elasticity, $\nu$ is Poisson's ratio, $\rho$ is density, and G is the shear modulus of the material.

$$C_0 = \sqrt{C_L^2 - \frac{4}{3}C_S^2} \qquad (2.27)$$

$$C_0 = \sqrt{\frac{K}{\rho}} \tag{2.28}$$

$$C_L = \sqrt{\frac{E(1 - \nu)}{\rho(1 + \nu)(1 - 2\nu)}} \tag{2.29}$$

$$C_s = \sqrt{\frac{E}{2\rho(1 + \nu)}} \; or \; \sqrt{\frac{G}{\rho}} \tag{2.30}$$

As discussed, S defines the gradient of the linear relationship between shock velocity and particle velocity. It is interesting to note that this property has been tentatively linked to material behaviour under shock loading, with lower values of S relating to increased resistance to compression and material stiffness [32]. Millett et al. [32] have also suggested that higher values of $C_0$ may also result in increased resistance to shock compression.

The five key shock parameters required to define the passage of a shock through a material ($U_s$, $u_p$, P, $\rho$, and E) have been discussed previously. In practical terms, it is possible to measure the shock velocity and shock pressure/stress ($\sigma_x$) experimentally using manganin foil pressure gauges in conjunction with the the plate-impact technique (see Section 3.1). The additional application of the impedance matching technique (covered in Section 3.2) to this approach further allows the particle velocity for a particular plate-impact/shock event using manganin gauge diagnostics to be calculated. Thus, an individual plate-impact experiment may provide a single $U_s$-$u_p$ datapoint

within the principal Hugoniot plane. As both $U_s$ and $u_p$ are seen to increase with impact velocity, a curve may be plotted through the datapoints that result from testing over a range of impact conditions. This curve will typically be of the form depicted by Equation 2.26 and is known as the 'Hugoniot curve', or simply the 'Hugoniot' of a material. For any shocked material previously occupying an initial state of $P_0 - V_0$, the curve that is generated is known as the principal Hugoniot. The Hugoniot is the locus of all attainable shocked states for a material over the range of shock and particle velocities for which measured data exists. In circumstances in which a material is shocked more than once, each successive Hugoniot is re-centred on the previous state.

The principal Hugoniot plane contains no information about the stress imparted by the shock or the strength of the shocked material. As such, any other permeatations of the material's principal Hugoniot, e.g. the P-$u_p$ or P-V plane, will reflect its hydrodynamic or 'predicted' response. Conversely, stress levels imparted to a target material during plate-impact (measured by manganin foil pressure gauges) will show a more representative material response.

Usefully, the linear relationship established for most materials within the principal Hugoniot (see Equation 2.26) allows for the construction of pressure-particle velocity (P-$u_p$) and pressure-volume (P-V) Hugoniot relationships. In each case, the hydrodynamic pressure is calculated using Equation 2.31. In the P-V plane volume is calculated using Equation 2.32. Within the P-$u_p$ plane, values for particle veloc-

ity are incremental and specified to cover an appropriate range by the user, i.e. a range suiting a set of experimental datapoints. Notably, differences between the predicted and measured pressure/stress for a material may highlight material strength and provide information which can be related to microstructural changes within the material during shock compression. Similarly, any difference between measured and predicted response may bear a close relationship to the nature of atomic and/or chemical bonding present within a compressed material.

$$P = \rho_0 U_s u_p \tag{2.31}$$

$$V = V_0 \left( \frac{U_s - u_p}{U_s} \right) \tag{2.32}$$

The $U_s$-$u_p$ Hugoniots for G13 WC-Co (tungsten carbide) and PG1190 polyurethane replacement resin (PRR) are shown in Figures 2.5 and 2.6, respectively. Notably, the response of the tungsten carbide ceramic [33] appears to be largely bilinear, although an initial elastic region up to $u_p = 0.03$ mm/$\mu$s is also apparent within the data. The bilinear response of the material has been attributed to the interplay of the two components/phases within the material, with the response of the WC particles becoming dominant at higher particle velocities. Of further interest is that the Hugoniot does not intercept the bulk sound speed (where $C_B = C_0$), but rather the higher elastic

wave speed of the material. Essentially, this data allows that a greater shock velocity may exist within the material than would otherwise be predicted by the linear portion of the Hugoniot at particle velocities greater than c.0.2 mm/$\mu$s. Again, the principle of a predicted linear intercept between the $U_s$-$u_p$ Hugoniot and the bulk sound speed of a material is not maintained in certain polymeric materials, such as PRR (polyurethane replacement resin). While largely linear in nature, curvature of Hugoniot for PRR has been observed at lower particle velocities (see Figure 2.6). This phenomenon has been linked to the effect of steric hindrance, i.e. compression of the side chains within the polymeric structure of the material at lower particle velocities prior to secondary compression of the carbon back-bone chain at shock states of increased magnitude.
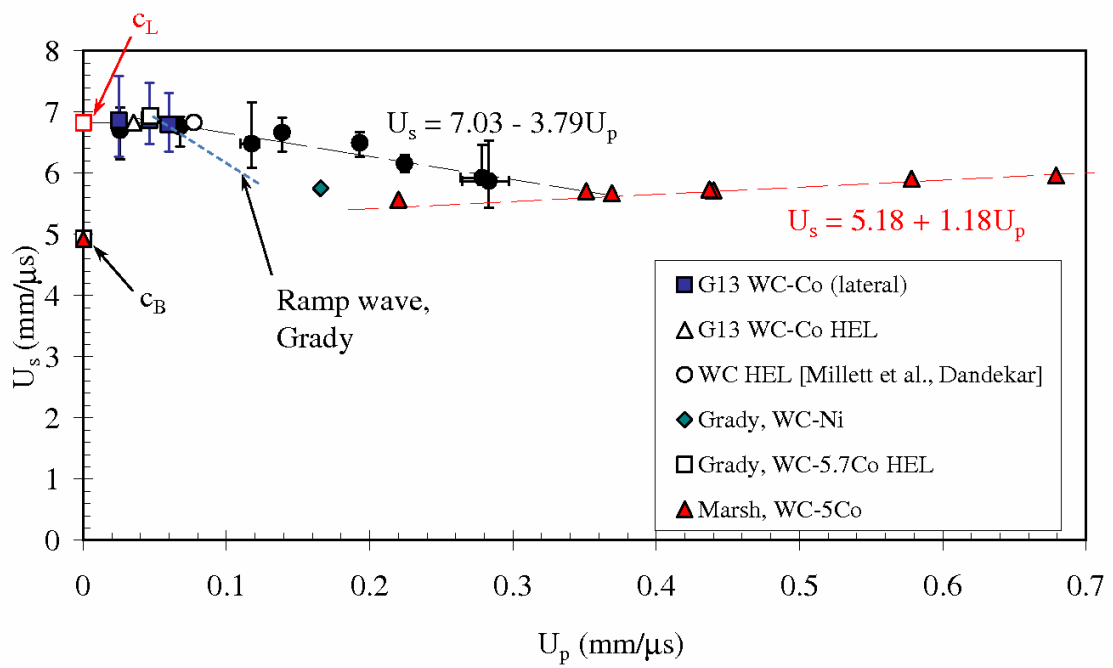
Figure 2.5: $U_s$-$u_p$ relationship for G13 WC-Co plus comparative relationships - taken from [33] (Comparative results taken from [34, 35, 36, 37])
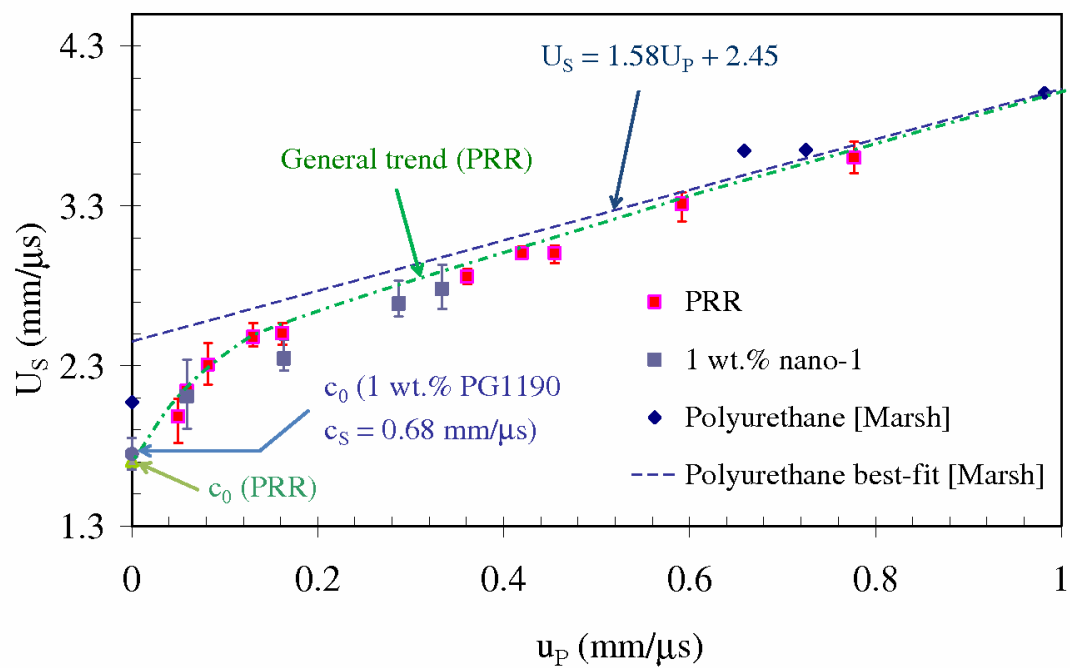
Figure 2.6: $U_s$-$u_p$ Hugoniot for pure and 1 wt.% PG1190 Polyurethane Replacement Resin (PRR) - adapted with permission from [31]. Comparative data is taken from [36]

## 2.4 The Shock Wave Profile

Processes that lead to abrupt rises in pressure or temperature within a body, such as high energy collisions or electrical/radiation discharge of sufficient energy, will inevitably lead to the formation of shock waves. An 'ideal' shock wave profile is considered to comprise three main elements: (i) an infinitely steep rise, signifying the passage of the shock front; (ii) an elevated and constant Hugoniot stress/pressure; (iii) a uniform release from the shocked state back to ambient conditions. This forms the basis of the square-topped pulse, which is shown in Figure 2.7. In reality, however, the broad-ranging nature of materials (e.g. metals, ceramics, polymers, biological tissues, energetic materials) dictates that real shock wave profiles do not always adhere to this strict wave profile. Conversely, real shock profiles tend to reflect artifacts occurring within the material as a result of shock compression. These may include such processes/changes as structural alterations, damage mechanisms, and shock-induced chemical changes (e.g. phase changes within powder mixtures or chemical solutions). In addition, features both within the shock wave profile and which pertain to material behaviour during shock compression may include the Hugoniot elastic limit (HEL), spall signals, and elastic-plastic transitions occurring during release. Essentially, the shock wave profile is an intimate reflection of material response during dynamic compression.

Grady [38] provided a useful discussion of the role/importance of the shock profile in determining the dynamic behaviour of several hot-pressed silicon carbide ceramics and a reaction bonded silicon carbide

ceramic. His analysis of the shock profiles for the tested ceramics revealed marked differences in the structure of the elastic precursor wave - detected using diffused velocity interferometry (VISAR) methods. In addition, Grady's analysis of the post-HEL structure of the precursor wave identified differences in the hardening characteristics of the ceramics and showed that the finest-grained, hot-pressed ceramic exhibited the highest dynamic strength. Other examples of work relating features within shock profiles to the behavior of materials during shock compression include: Hayun et al. [39], who examined the effect of varying microstructures despite similar phase composition within boron-carbide composites; Grady [40], who examined phase-transitions, spall failure, and shear fracture within brittle solids; and Hereil et al. [41], who looked at experimental characterisation of the shock wave behaviour of porous aluminium. Two examples of real world shock profiles are provided in Figures 2.8 (a) and (b), respectively. Figure 2.8 (a) shows shock compression profiles for aluminium oxide - ranging from a lowest peak pressure of 10 GPa to a highest peak pressure of 40 GPa. In addition, Figure 2.8 (b) highlights the effect of multiple phase changes within an aluminium nitride ceramic upon the structure of the compressive wave profile.
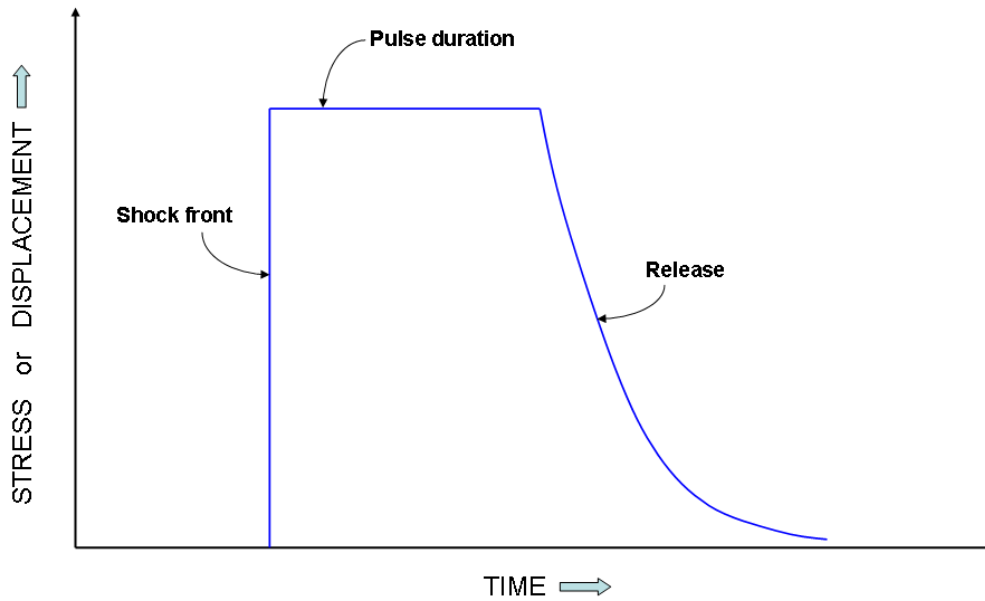
Figure 2.7: Idealised shock wave profile [25]
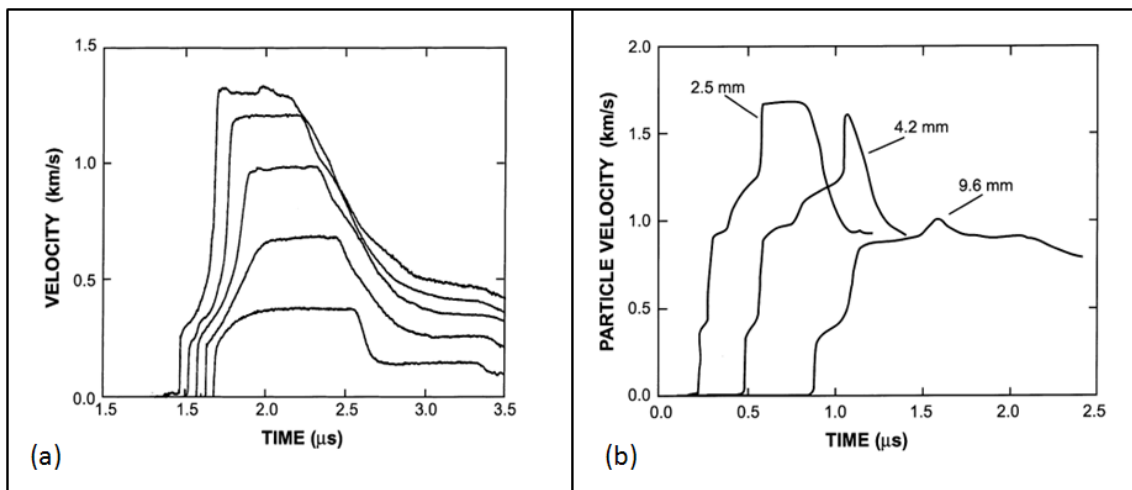


Figure 2.8: Examples of non-idealised shock wave profiles: (a) shock compression profiles for aluminium oxide (10 GPa lowest peak pressure, 40 GPa highest peak pressure); (b) wave profiles measured in differing thicknesses of an aluminium nitride ceramic sample (impacted at the same velocity)

# Chapter 3

# Experimental Methods in Shock Wave Studies

## 3.1 The Plate-Impact Technique

In order to simplify investigation of the high strain-rate deformation of materials, loading mechanisms such as tension and compression are often studied individually. Notably, the response of certain materials (e.g. carbon-fibre composites) often differs significantly with respect to the loading direction. It is also the case that physical response often relates closely to the structural composition of the material. For example, the behaviour of a carbon fibre-composite during dynamic loading may be influenced by the nature of the weave present within the fibres, the type of resin in which the fibres are bound, and the volume fraction of resin within the composite material. Accordingly, the behaviour of a material to a specific type of loading will also typically be investigated in the X, Y, and Z orientations individually. Determination of the uniaxial response of a material with respect to

its anisotropy may provide a greater understanding of behaviours that may be apparent during complex (three-dimensional) loading regimes.

The plate-impact technique allows for one-dimensional shock-loading of materials at strain-rates of $10^6$ to $10^7$ s$^{-1}$ [42]. With respect to the properties of the shocked material, the technique can yield pressure states in the order of hundreds of gigapascals (GPa). The basis of the technique involves induction of a planar shock within the target material by impacting it with a flyer-plate that has been machined sufficiently flat [43]. Both the front and rear surfaces of flyer and the target are typically flat and parallel to one another to a tolerance of <10 $\mu$m. Parallel surfaces ensure that all points of the surface of the flyer and the target make contact simultaneously. Such measures, when combined with the inertial confinement of the sample, dictate that a state of uniaxial strain is imparted to the target. This state will exist until release waves enter the shocked material, either from the rear of the flyer or the periphery of the sample. It is important to note that shock waves are not sustainable; that is, the velocity of the release wave is always greater than that of the propagating shock. In plate-impact experiments, the duration of one-dimensionality is typically governed by the thickness of the flyer and/or the diameter of the sample and flyer.

Figure 3.1 shows the sequence of events occurring during flyer-plate impact. Prior to impact, i.e. at t < 0, the flyer is moving at velocity $v$ towards a stationary target. Compressive shocks form in both the flyer and the target materials after impact. These shocks propagate

67
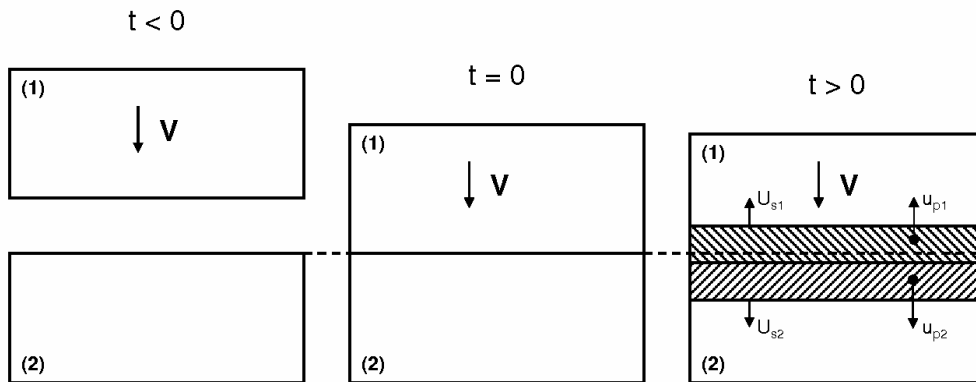
Figure 3.1: Sequence of events occurring during plate-impact (adapted from [25])

through the flyer and the target material with velocity $U_{s1}$ and $U_{s2}$, respectively. In addition, a particle velocity ($u_p$) is imparted to both the flyer and the target materials. If both the flyer and the target are comprised of the same material, e.g. copper, the shock and particle velocities ($U_{s1}$, $U_{s2}$ and $u_{p1}$, $u_{p2}$) will equate. However, these values will differ significantly if the flyer and target are comprised of dissimilar materials. In order to calculate the pressure, shock velocity, and particle velocity within the respective elements, a set of quadratic equations are required. The mathematics involved in such calculations forms the basis of the impedance matching technique, which is covered in Section 3.2. Notably, flyers are typically accelerated by gas gun systems [43, 44, 45], the detonation of explosive charges [46], or by laser methods [47].

## 3.2   The Impedance Matching Technique

In likeness with the conservation equations, - see Section 2.2 - the calculation of material properties using the impedance matching technique requires that the shock conditions be one dimensional. It has been shown previously that $P = \rho_0 U_s u_p$, where $\rho_0 U_s$ is the impedance ($Z$) of the shocked material. Further, during planar shock interactions, $P$ is equal to the uniaxial stress normal to the propagating wave.

Usefully, diagnostic techniques are available for the determination of particle velocity during symmetric plate-impact. These include velocity interferometry systems (VISAR) [48] and heterodyne velocimetry (HetV) [49]. Manganin foil pressure gauges are also frequently utilized during plate-impact experiments due to their ability to measure both shock velocity and the stress imparted to the target material. The recent development and implementation of particle velocity gauges [50, 51] has addressed the inability of longitudinal manganin foil gauges to measure particle velocity directly. When using longitudinal gauges alone, particle velocity is derived from measured values of impact and shock velocity using the impedance matching technique.

It is often necessary to calculate the shock conditions expected within a material prior to experiment. If the Hugoniot of a material is sufficiently well characterized and accuracy is not of particular importance, shock parameters may be calculated without experiment at all. Isbell [26] stated that, for a symmetric impact event where a specimen of material is launched at velocity $v$ onto a specimen comprised of the same material, a shock wave will be induced with particle velocity

equal to exactly one half the impact velocity, or

$$u_p = 1/2v \qquad (3.1)$$

Provided the Hugoniot of the material is known, it is also possible to calculate the stress within both the target and the impactor.

Flyer-plate launch/accelerator systems such as gas guns have a maximum operational velocity. As such, the maximum pressure/stress that may be imparted to a target material by the 'like-for-like' impact approach is limited. In order to obtain pressures higher than those created by 'like-for-like' impact, a target must be impacted with a flyer constructed from a material of higher shock impedance/density. Conversely, if a lower shock pressure is required, a flyer of lower impedance may be selected. If the Hugoniot of the impactor material is known, measurement of the impact velocity and the shock velocity is sufficient to calculate a point on the Hugoniot for the target material. However, this approach necessitates the use of a cover-plate comprised of the same material and shock impedance as the flyer. The calculated Hugoniot point determined using this method gives the particle velocity that will be introduced into both the cover-plate and the specimen by the impact event (i.e. $P = \rho_0 U_s u_p$, where $u_p$ is determined from the known impactor Hugoniot). This approach is known as the impedance matching technique [52].

For a given plate-impact experiment, e.g. a 500 m/s copper flyer

impacting a polyethylene target with a copper cover-plate, the shock velocity within the cover (copper) and the target material (polyethylene) will differ. As the initial density is known, measurement of both the shock and impact velocities will allow for the calculation of the particle velocity and the resultant pressure/longitudinal stress ($P = \rho_0 U_s u_p$) imparted to the target material. The shock velocity in plate-impact experiments involving two longitudinal manganin foil pressure gauges (one at both the front and rear surface of the sample) is determined by their temporal response to shock arrival. Notably, the impedance matching technique assumes that the shocked materials exhibit hydrodynamic behaviour. As such, gauges may highlight any potential difference between predicted and measured stress levels and provide insight into material behaviour.

Meyers [25] provides both a useful descriptive and graphical overview of the impedance matching technique. Graphically, the technique may be depicted in the pressure-particle velocity ($Pu_p$) plane. Figure 3.2 provides an example of this and predicts the shock conditions expected when specimens of copper, aluminium, and PMMA (polymethyl-methacrylate) are impacted by a copper flyer at 800 m/s, respectively.

Initially, the reverse Hugoniot of the flyer material must be constructed and offset by the impact velocity. This is satisfied using Equation 3.2. Following this, it is possible to construct Hugoniots for the specimen materials over an appropriate particle velocitiy range (Equation 3.3). This provides an indication of the stress and particle

velocity expected upon impact. It is then necessary to calculate the precise pressure/stress and particle velocity at which the two Hugoniot curves overlap. Thus, polynomial coefficients for the the specimen materials ($P = Au_p^2 + Bu_p + C$) and the reversed Hugoniot of the flyer material ($P = Au_p^2 - Bu_p + C$) must be determined. Having obtained these values, it is possible to use the 'goalseek' function within Microsoft Excel to set the difference between $P_{impactor}$ and $P_{specimen}$ to zero. Such action provides pressure/stress and particle velocity values at the intercept of the Hugoniot of the flyer material and the specimen.

$$P = \rho_0 C_0 (V_{imp} - u_p) + \rho_0 S (V_{imp} - u_p)^2 \tag{3.2}$$

$$P = \rho_0 (C_0 + S u_p) u_p \tag{3.3}$$

The particle velocity for an experimental datapoint may be derived using measured values of shock and impact velocity. This approach yields much greater accuracy than when using predicted impact conditions, e.g. as per the previous 500 m/s copper impact example. Notably, manganin foil pressure gauges - the primary diagnostic used in this body of work - may be used to determine shock velocity. In addition, impact velocity may be experimentally determined by the velocity measurement system employed by the 50 mm single-stage gas gun used to conduct all plate-impact experiments in this body of work
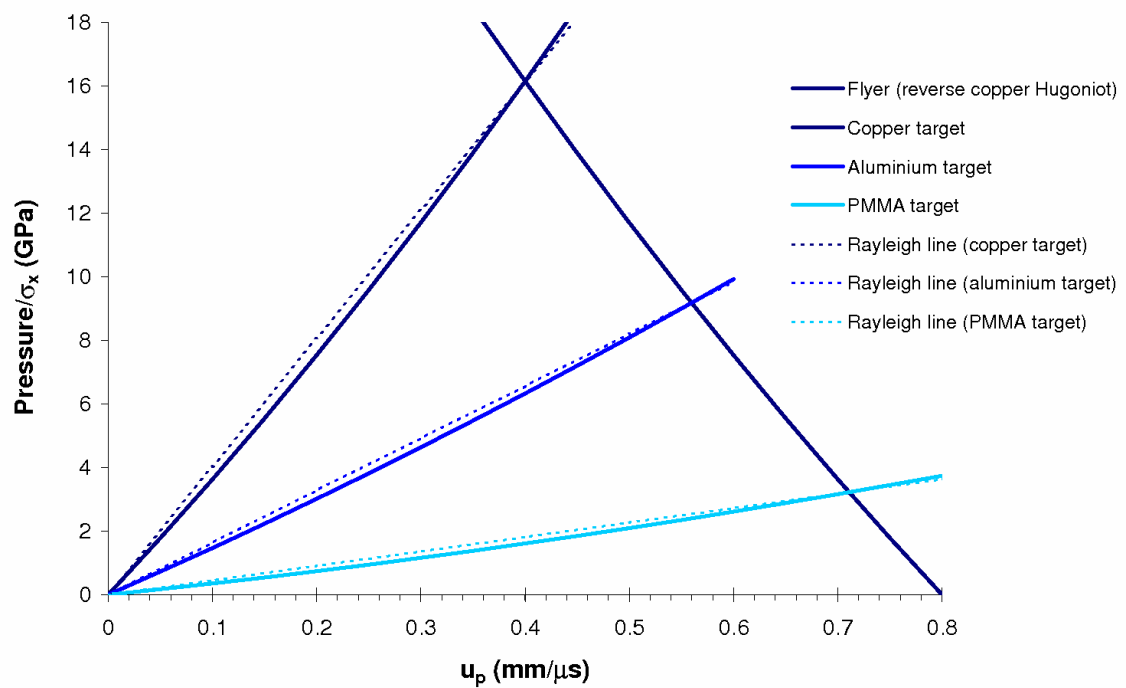
Figure 3.2: The impedance matching technique - graphical representation of a copper flyer impacting specimens of different shock impedance

(see Section 4.1).

Calculating the particle velocity from experimental values is performed by firstly equating the intersection of the reversed Hugoniot of the flyer ($P = Au_p^2 - Bu_p + C$) and the Raleigh line ($P = \rho_0 U_s(u_p + V_{imp})$) - see Equation 3.4. By rearranging and collecting like terms, a new quadratic is given (Equation 3.5) where: $a = A$; $b = (-B - \rho_0 U_s)u_p$, and; $c = (C - \rho_0 U_s V_{imp})$. Values for A, B, and C in this relationship are obtained from a quadratic fit to the Hugoniot of the flyer material. A graphical representation of this process is provided by Figure 3.3

As mentioned, both shock velocity ($U_s$) and impact velocity ($V_{imp}$) are measured experimentally. The solution to Equation 3.5 provides the offset particle velocity for a given shock interaction (see point 'I' in Figure 3.3. The correct particle velocity is obtained by removing the shift along the particle velocity axis, i.e. $u_p = u'_p + V_{imp}$.

$$Au_p^2 - Bu_p + C = \rho_0 U_s(u_p + V_{imp}) \tag{3.4}$$

$$Au_p^2 + (-B - \rho_0 U_s)u_p + (C - \rho_0 U_s V_{imp}) = 0 \tag{3.5}$$
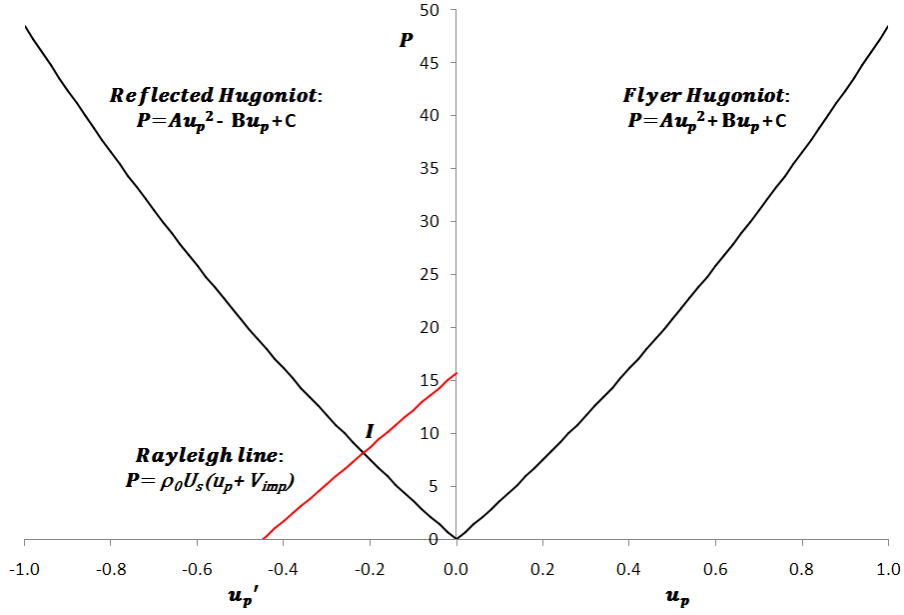
Figure 3.3: Experimental approach towards the calculation of particle velocity using the Impedance Matching Technique

## 3.3  Shock-Recovery Techniques

Shock-recovery or soft-capture methods are typically employed in conjunction with plate-impact techniques as a means to investigate the microstructural changes that occur within materials as a result of shock-loading. In such circumstances, the shock impulse is typically tailored so that the target material experiences a simple square-topped pulse that loads and then completely releases back to ambient conditions. Further, globally one-dimensional (1D) loading is typically desirable. In this study, a soft-capture system has been developed in order to facilitate the shock-recovery of skeletal muscle tissue. The capture system has been developed using the broad range of information on shock-recovery techniques that may be found within the literature. This current section provides a useful overview of the avail-

able literature and the techniques that have allowed for the successful shock-recovery of a number of materials in conjunction with the plate-impact technique. Notably, one method that has repeatedly allowed for the recovery of shocked materials is the baseline design [53], [54], [55]. An optimized variation of the baseline design is shown in Figure 3.4.

A useful assessment of the baseline design is provided by Bourne and Gray III [56]. These authors highlight the key features of the arrangement as: (i) the use of momentum-trapping rings, which serve the purpose of trapping or reducing the effects of radial release waves from the periphery of the target, and (ii) the use of a spall element at the rear of the target, which acts to reduce the magnitude of longitudinal releases from the rear of the target. Numerical simulations presented by Bourne and Gray III [56], also highlight two shortcomings with the geometry of the baseline design for a copper on copper impact event. Firstly, significant levels of lateral unloading were shown to occur within the target material by the authors, despite the use of momentum-trapping rings. Such unloading is undesirable within the specimen as it reduces the one-dimensionality of the shock imparted to the target material. The authors also noted that trapping of the longitudinal tensile release that occurs from the rear of the target was incomplete, despite the engineered inclusion of a spallation plate at the rear of the target assembly. In light of these results, Bourne and Gray III [56] provided a series of numerical models aiming to optimise the baseline design. Their results showed that the replacement of a
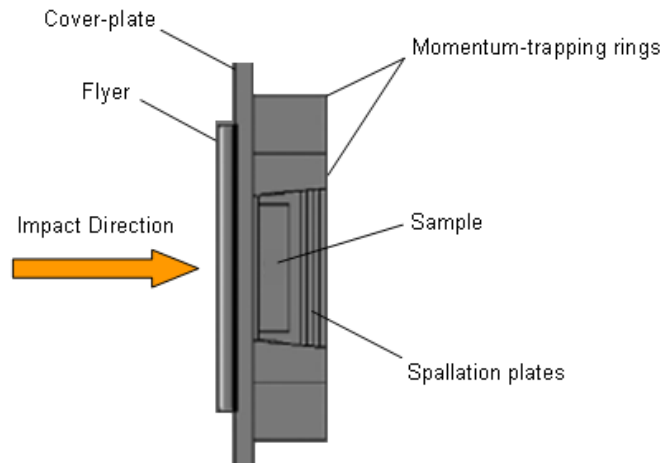
Figure 3.4: Schematic representation of an optimised baseline design for use in shock-recovery experiments [56]

single spallation with multiple stacked plates enhanced the ability to trap tensile release waves from the rear of the target assembly. In addition, the use of two external rings was shown to minimise radial release waves from developing at the peripheral regions of the target. This modification ensured a more complete state of uniaxial strain within the sample material during impact.

In another paper by the same authors [57], numerical optimization of the baseline design successfully allowed for the soft-capture of polymethyl-methacrylate (PMMA) and a composite material comprising glass and hydroxy-terminated polybutadiene (HTPB). In addition, subsequent structural analysis provided insight into the effects of one-dimensional shock loading upon the recovered materials. The authors detailed the requirement for rapid cooling of the sample materials following shock compression in order to prevent the material

77

from annealing (a process which would have significantly modified the as-shocked microstructure). In contrast with fully-recovered PMMA and HTPB samples, the spallation plates recovered from the rear of the modified baseline target assemblies were shattered. This provided positive indication that they had absorbed the tensile stresses introduced into the target by the release waves of the shock.

As previously discussed, the baseline design makes use of momentum-trapping rings around the target to ensure that the wave profile within the material remains both uninfluenced by peripheral release waves and planar in nature. In contrast with this technique, Raiser et al. [58] sought to minimize cylindrical release waves from the target periphery by using a complimentary momentum trap and star-shaped flyer technique. During their soft-capture investigation of microcracking effects within alumina, Raiser et al. [58] measured stress wave profiles within their targets via laser interferometry. The experimental approach and diagnostic methods employed showed that only a central octagonal region within the target was subjected to the planar pulse with little or no effect from peripheral waves. Additionally, the analysis of recovered specimens via electron microscope showed that microcracking along grain boundaries had occurred within the ceramic as a result of the inelastic loading conditions.

Another example of the nature of research involving the shock-recovery of materials is provided by Kurita et al. [59] who investigated the effect of shock on mixtures of nickel and boron powders. A total of three plate-impact experiments were conducted upon powdered mix-

tures at impact velocities of 0.7 - 1.4 km/s in the mentioned work. This resulted in a range of impact pressures from approximately 4 - 11 GPa. Sample material was initially confined within a copper capsule before secondary confinement within a mild steel capsule holder. In likeness with Raiser et al. [58], Kurita et al. also make use of a momentum trap in order to capture reflective waves from the rear of the target arrangement. However, in contrast, the authors did not significantly attempt to remove or reduce the effect of peripheral shock interactions within the sample material. A combination of optical microscopy and transmission electron microscopy were used to highlight differences between shock-synthesised material within two distinct regions of the recovered mass. These were: (i) globally planar, and; (ii) peripherally influenced sites of shock interaction. Findings showed that nickel boride was formed at higher shock pressures and that, as a result of the shock conditions evolved during the highest impact velocity experiment, a large part of the nickel particles were interconnected and formed bubble-like structures. A diagram of the experimental setup used by Kurita et al. in their investigation into the effect of shock compression on powdered mixtures of nickel and boron is presented in Figure 3.5.

Shock-recovery methods have also been employed during investigations into the effect of shock wave compression on microorganism-loaded broths and emulsions [60]. In contrast with the baseline approach mentioned previously, Hazell et al. employed a type AISI 304L steel capsule design in two distinct types of experiments involving bac-
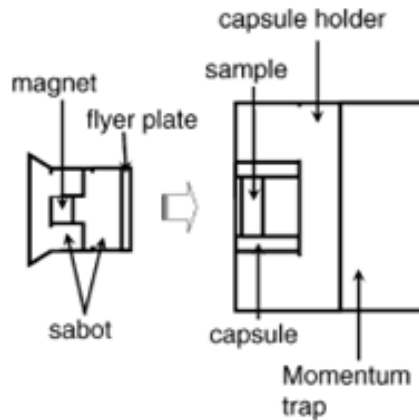
Figure 3.5: Schematic showing the cross-sectional area of the projectile and shock-recovery capsule used by Kurita et al. [59]

terial broths. Their initial experiment involved shock-compression of samples to high pressures with active suppression of any cavitation within the fluid layer. A second experiment provided deliberate inclusion of an air cavity, thus allowing cavitation within the sample. ANSYS® AUTODYN hydrocode simulations of each type of experiment were performed in order to visualise shock wave interaction in the fluid. This allowed direct comparison between the extent of deformation imparted to the capsule lid in both the experimental and numerical trials. Good agreement was apparent between both sets of results.

A schematic for the capsule employed by Hazell et al. is shown in Figure 3.6. The overall dimensions of the vessel; the use of a copper cover-plate, to which the flyer material was matched; and the inclusion of a (manganin foil) stress gauge at the front surface of the capture vessel are also highlighted in the diagram. The stress-time data from
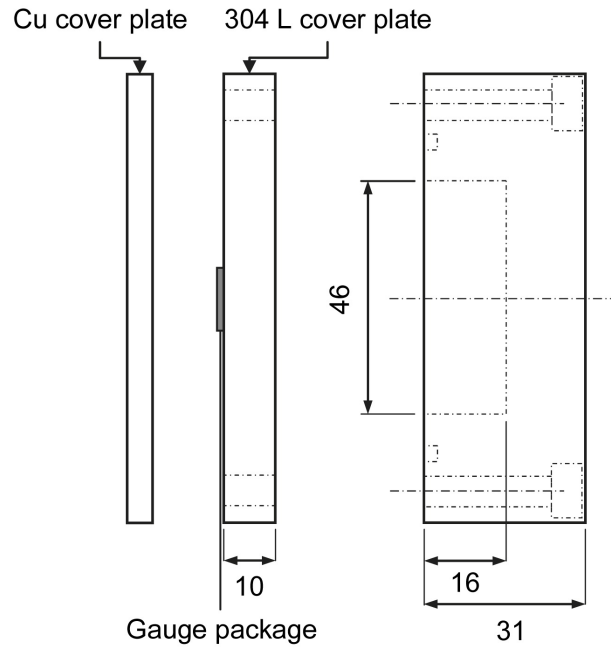
Figure 3.6: Soft-capture system used to investigate the effect of shock wave compression on bacterial-loaded broths and emulsions [60]

the gauges employed in experiments was later used to validate the numerical simulations that were presented by the authors.

One key difference between the baseline design and the capsule used by Hazell et al. is the loading profile experienced by the sample materials in the respective techniques. Whereas the baseline design was specifically designed to induce a square-topped pulse prior to release, the capsule design of Hazell et al. allowed for the 'ring-up' of shock pressure (shock reflection) within the sample cavity. This property, however, was clearly a design feature that reflected the purpose of the experiments conducted using the 304L steel capsule, i.e. the main aim of the experiments was to assess the survivability of bacteria to elevated shock pressures, not to impart a tailored wave profile to the sample.

As discussed previously, in order to simplify the analysis of experimental results in shock wave experiments, loading conditions are typically planar (i.e. one-dimensional). This approach seems particularly applicable to shock studies involving complex biological tissues such as skeletal muscle, which is both anisotropic and comprises a convoluted structure. As such, the shock-recovery experiments in this body of work were designed to impart a uniaxial shock profile similar to that of the baseline design. A detailed overview of the development of the a soft-capture system allowing for the shock recovery of skeletal muscle is provided in Section 6.

# Chapter 4

# Experimental Apparatus, Diagnostics, and Modelling Software

## 4.1   50 mm Single-Stage Gas Gun

Shock loading of target materials during this research project was achieved using the 50 mm single-stage gas gun located at Cranfield University within the Defence Academy of the United Kingdom, Shrivenham. An overview of the system is provided by Bourne [43]. During operation, a sabotted flyer-plate, comprising material of known equation-of-state and of 5 - 10 mm typical thickness, was accelerated towards the target by the rapid yet controlled expansion of compressed gas. Variation of gas pressure and type (typically helium or air) along with projectile mass allowed accurate control of projectile impact velocity. Just prior to impact, flyer velocity was measured via a sequential set of (spatially separate by 12mm) shorting graphite ($\leq 600$ m/s) or brass (>600 m/s) pins connected to a digital oscilloscope. Using
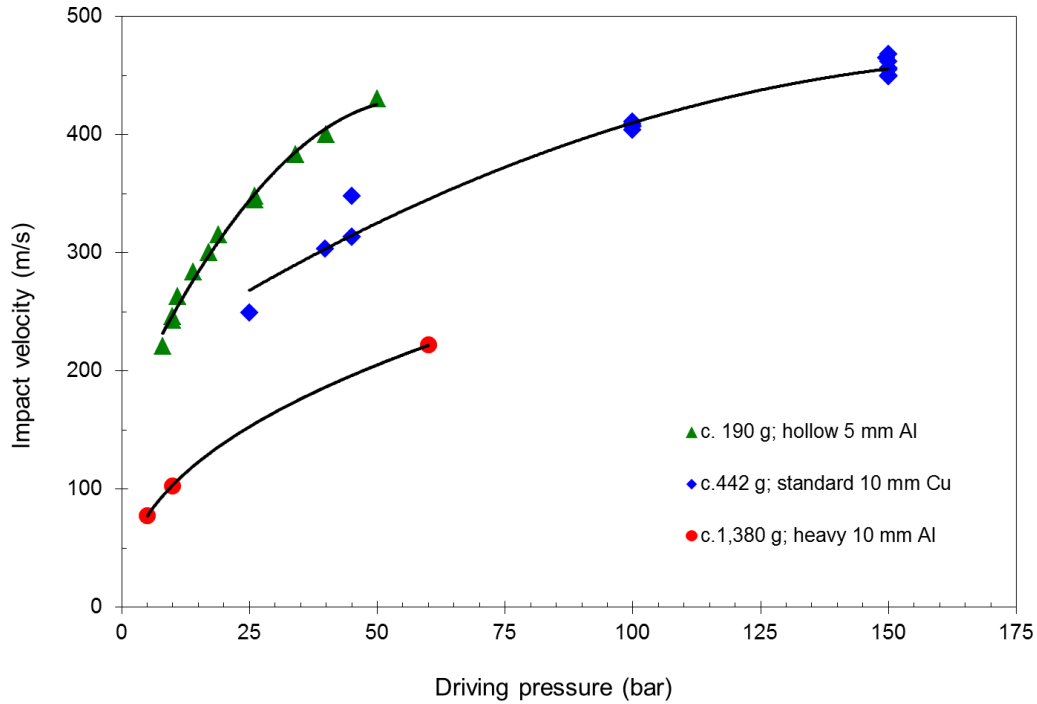
Figure 4.1: Air performance curves for the 50 mm single-stage gas gun

this method, velocities could be measured to $\pm 5$ m/s. Air and helium performance curves for a range of projectiles are shown in Figures 4.1 and 4.2, respectively.

A schematic of the 50 mm single-stage gas gun used in this research project is presented in Figure 4.3. Features to note include the 5 metre barrel, which limits the duration that the expanding gas may effectively act upon the projectile, and also the expansion chamber at the rear of the system. Under firing conditions, the expansion chamber, barrel, and target chamber are all reduced to vacuum. This occurs in two stages. Firstly, a large vacuum pump reduces the rear section of the system, i.e. the expansion tank and the target chamber. The overall design of the system is such that evacuation to 400 mbars is sufficient to prevent any overpressure during maximum velocity 350 bar
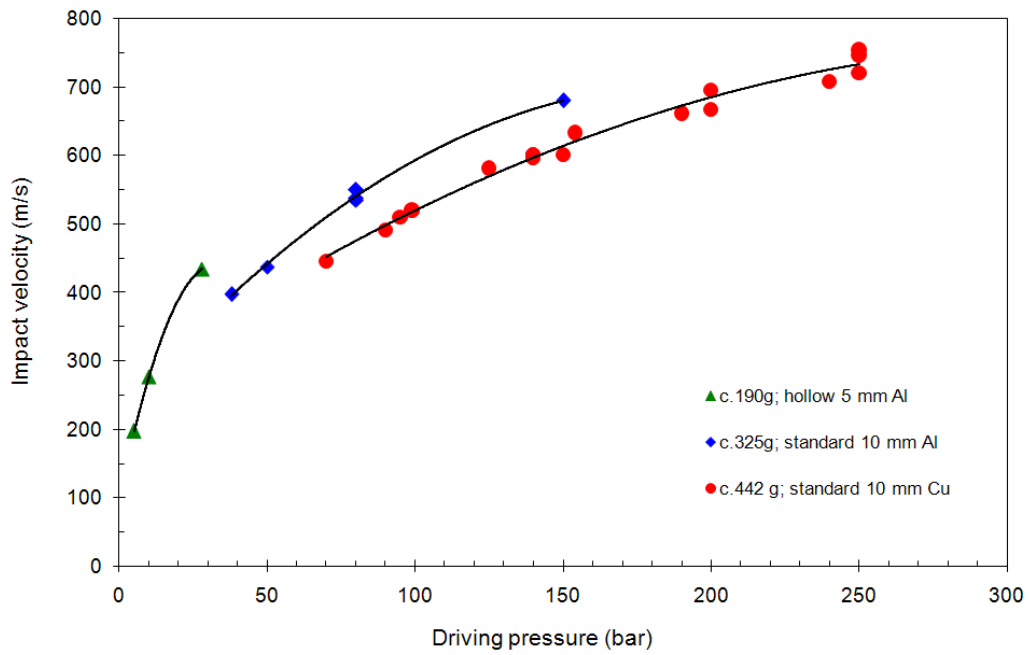
Figure 4.2: Helium performance curves for the 50 mm single-stage gas gun
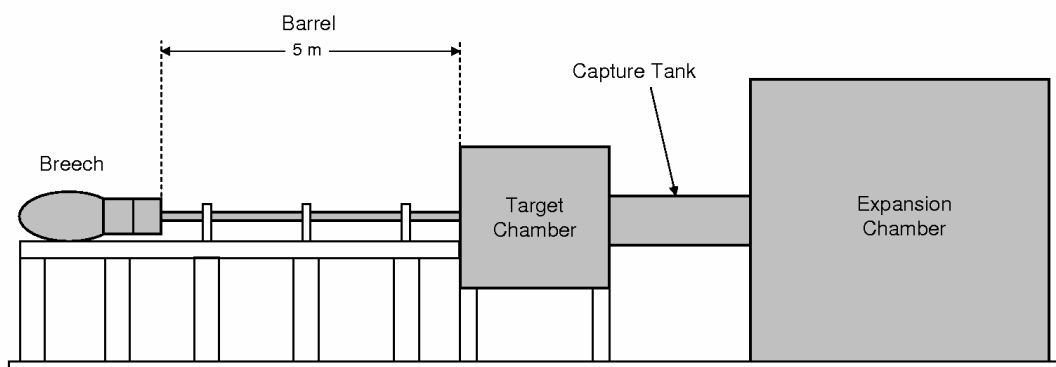


Figure 4.3: Schematic of 50mm single-stage gas gun

(breech pressure) shots. Secondly, a smaller vacuum pump evacuates the air within both the barrel of the gun and a sealed section mounted at the end of the barrel. Notably, this section contains the mounted target and incorporates a Perspex backing-plate, which is designed to fail after impact and allow the sabot and target debris to migrate into the capture chamber. Evacuation of the front section of the system (barrel and sealed target section): (a) prevents the projectile velocity from being retarded by air resistance, and; (b) minimizes the radial stresses which would otherwise be imparted to the barrel during the rapid expansion of the breech gasses into its closed cylindrical section.

Two arrangements were employed to control gas release/fire the gun.

1. Initially, a bursting disc arrangement was employed (see Figure 4.4). This involved sealing a cavity between the breech and evacuated barrel with a pair of Aluminium disks calibrated to burst at a particular pressure. This cavity was then charged to half the (breech) firing pressure. To fire the gun this cavity was rapidly evacuated, allowing first the disk adjacent to the breech and then that adjacent to the barrel to burst.

2. Subsequently, a fast-acting valve system was employed (see Figure 4.5). This involved sealing the barrel from the breech gases with a nose-tapered piston (45 degree angled faces). A cavity behind the piston was filled to a pressure 10 bars greater than the peak firing value (e.g. 310 bars for a 300 bar Helium shot). This ensured that the barrel remained completely sealed from the
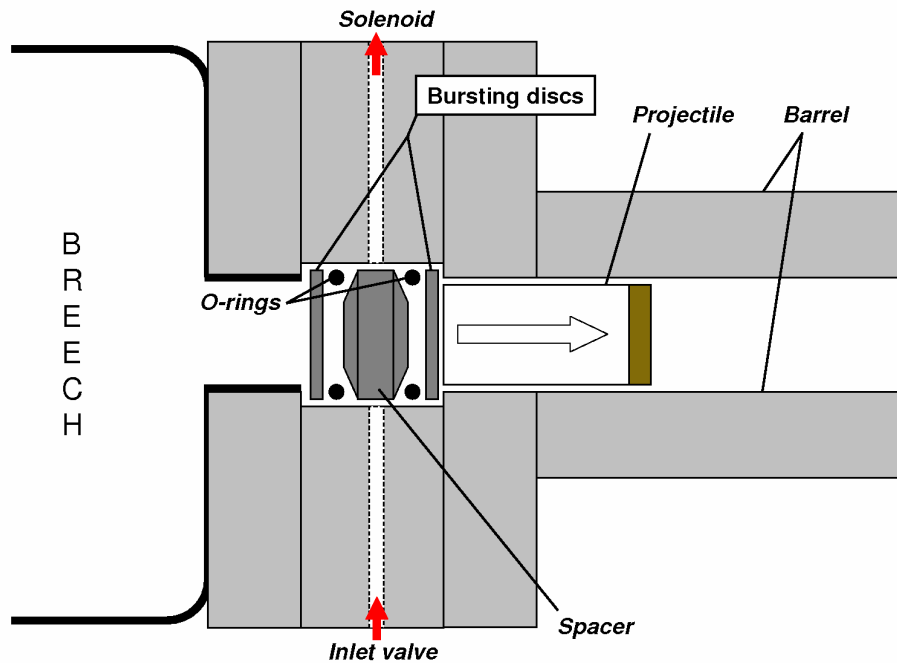
Figure 4.4: Schematic of the twin bursting-disc firing configuration

breech until the gun-system was fully pressurized and ready to be fired. To fire the gun, the cavity behind the nose-tapered piston was rapidly evacuated. No longer experiencing an opposing force, the pressure exerted upon the angled faces of the piston resulted in its rapid rearward extraction from barrel. At this point, the breech gas expanded into the barrel and imparted acceleration to the projectile.

The main reasons for implementing the fast-acting valve system within the gun were its increased ease of operation and the reduced likelihood of a misfire - seen to occur on an infrequent basis with the bursting disc approach.
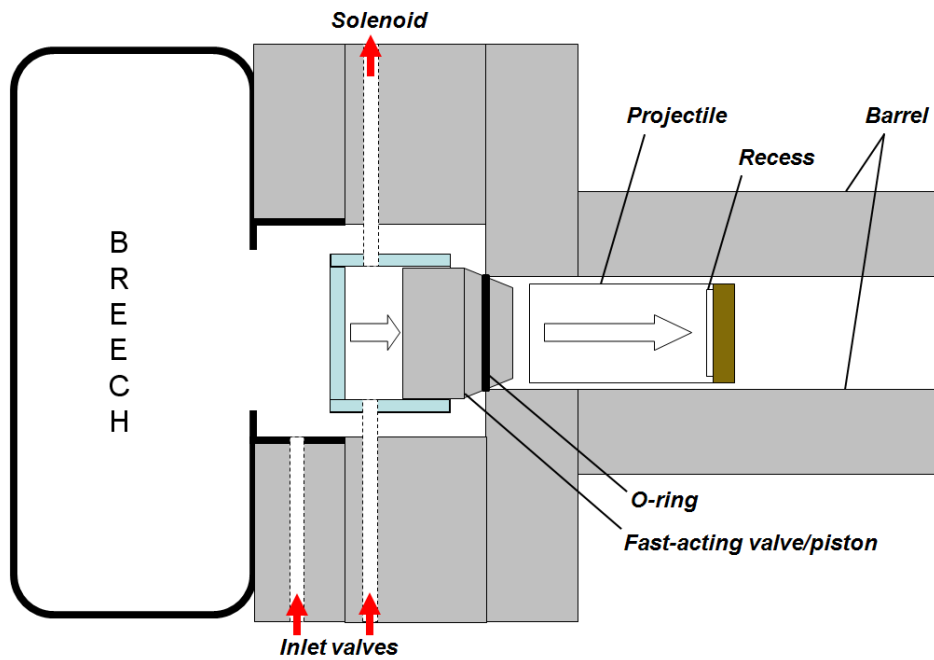
Figure 4.5: Schematic of the fast-acting valve system

## 4.2 Manganin-Foil Pressure Gauges

Manganin foil pressure gauges were employed as the primary diagnostic for investigating the interaction of shock waves with both adipose and muscular tissues in this body of work. During uniaxial shock compression, both longitudinal and lateral stress components evolve within the target material. Thus, two separate types of gauge were used to measure the respective stress components. The longitudinal component of stress was measured using type LM-SS-125CH-048 gauges, while the lateral component of stress was measured using type J2M-SS-580SF-025 gauges. Both gauge types were manufactured by Vishay Micro-Measurements[TM] & SR-4. A schematic for the construction of each gauge type is presented in Figure 4.7, highlighting clear differences between both their size and shape. In contrast with the

large grid element present within the type LM-SS-125CH-048, the type J2M-SS-580SF-025 gauge comprises a 't-type' element. In all cases, power was supplied to the gauges using a Dynasen Inc. pulse power supply (model CK2-50/0.050-300). Figure 4.6 is a circuit diagram showing: (i) connection of the Dynasen pulse power supply to a 50 ohm longitudinal gauge; (ii) the position of the trigger source in the circuit, and; (iii) the 50 ohm output, which allowed the electrical signal to reach the digital storage device (oscilloscope). The advantage of gauges is that they are "embedded" within the material flow. Essentially, this allows for accurate analysis of the stress-time response of the of the material as it undergoes compression by shock wave.

Manganin is particularly well suited for use in pressure/stress gauges due to: (a) its relative insensitivity to resistance change with temperature and; (b) its relatively high and almost constant piezoresistance, i.e. electrical resistance induced by pressure/stress [61]. The piezoresistive constants for manganin - an alloy comprising 84-86 % copper; 12 % manganese; and 2-4 % nickel - were derived by Barsis et al. [62]. Standard gauge calibration approaches, based on the compression curve determined for Manganin [62], are discussed over the next few pages. Longitudinal (type LM-SS-125CH-048) gauge calubration was detailed by Rosenberg et al [61], while that for lateral (type J2M-SS-580SF-025) gauges has evolved from studies by numerous authors [63, 64, 65].
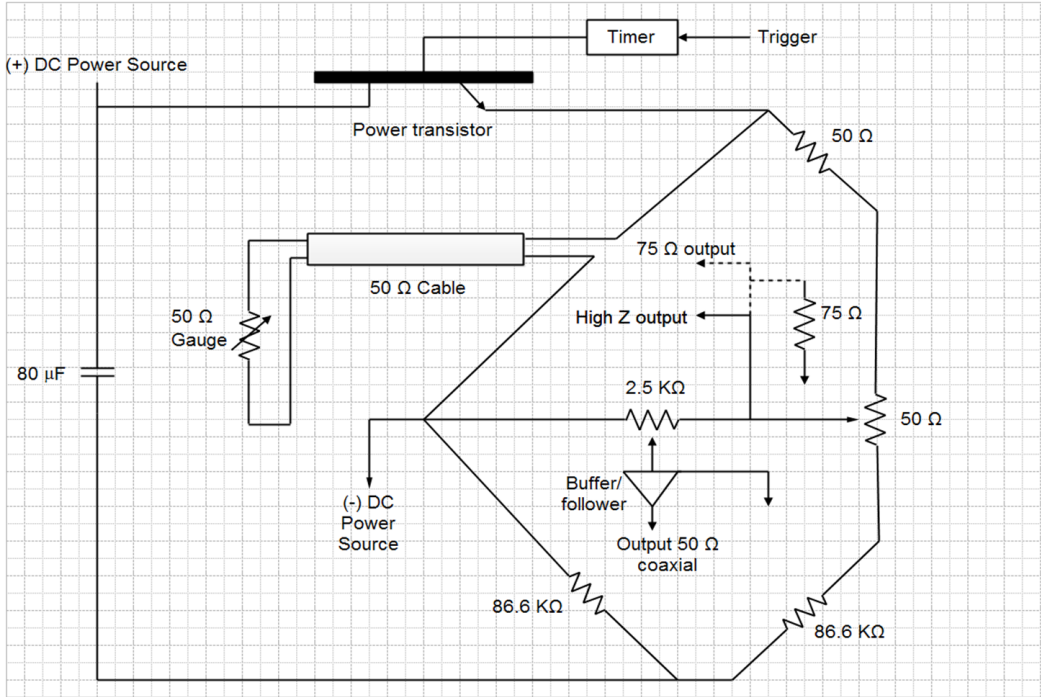
Figure 4.6: Dynasen Inc. pulse power supply and 50 ohm manganin foil pressure gauge circuit diagram

### 4.2.1 Calibration of Type LM-SS-125CH-048 Gauges

The relationship between measured voltage and the change in resistance of the gauge is determined by a quadratic fit (see Equation 4.1). Prior to an experiment, a series of seven resistors of increasing resistance are placed across the gauge and the resultant voltages recorded. This simulates the passage of a shock. A polynomial trend-line is fitted to the resulting resistance-voltage data, giving the coefficients that are required to satisfy Equation 4.1. During a plate-impact experiment the voltage-time data from the gauge is recorded on a digital storage oscilloscope. Thus, each change in voltage can be related to the change in resistance using Equation 4.1. A relative change in resistance $(dR_i)$ for each change in resistance may then be defined using

Figure 4.7: Type LM-SS-125CH-048 and J2M-SS-580SF-025 gauge construction (not to scale)

Equation 4.2.

Notably, type LM-SS-125CH-048 manganin gauges have an elastic-plastic transition, or Hugoniot Elastic Limit (HEL), at ~1.5 GPa [66]. This transition stage is incorporated into the calibration method by defining a cut-off point via Equation 4.3. For each relative change in resistance ($dR_i$), the pressure/stress must be calculated. If $dR \leq d_{crit}$ (where $d_{crit} = 1.5$ GPa), pressure/stress is calculated according to Equation 4.4. Otherwise, pressure/stress is calculated using Equation 4.5, where $m_0$ to $m_5$ are constants based upon the response of the gauge (see Table 4.1).

$$\Delta R_i = AV_i^2 + BV_i + C \tag{4.1}$$

$$dR_i = \frac{\Delta R_i}{R_0} \tag{4.2}$$

$$dR_{crit} = m_0 HEL \tag{4.3}$$

$$P_i = \frac{dR_i}{m_0} \tag{4.4}$$

91

| $m_0$ | $m_1$ | $m_2$ | $m_3$ | $m_4$ | $m_5$ |
|---|---|---|---|---|---|
| 0.0195 | 0.5720 | 25.590 | 95.200 | -312.740 | 331.770 |

Table 4.1: Type LM-SS-125CH-048 longitudinal gauge constants (constants derived by [61])

$$P_i = m_1 + m_2 dR_i + m_3 dR_i^2 + m_4 dR_i^3 + m_5 dR_i^4 \qquad (4.5)$$

### 4.2.2   Calibration of Type J2M-SS-580SF-025 Gauges

The calibration and interpretation of lateral gauges requires consideration of a number of key equations. These include equations for: (a) the yield surface of manganin ($Y_g$ in Equation 4.6), which was derived from Rosenberg and Partom [66]; (b) the hydrodynamic compression curve for manganin [62] (Equation 4.7); (c) the piezoresistive response of manganin [63] (Equation 4.8), and; (d) the relationship between hydrostatic pressure and lateral stress (Equation 4.9).

$$Y_g = (0.14995 \times P) + 6.5542 \tag{4.6}$$

$$P = 4120\epsilon_v^2 + 1160\epsilon_v \tag{4.7}$$

$$\Delta = \frac{\Delta R}{R_0} = 9.89\epsilon_v^2 + 3.45\epsilon_v + (5.17 \times 10^{-4}) \tag{4.8}$$

$$\sigma_y = P - \frac{1}{3}Y_g \tag{4.9}$$

where $Y_g$ is the yield surface of manganin; $P$ is pressure; $\epsilon_v$ is volumetric strain; $\Delta R$ is the relative change in resistance in the gauge; $R_0$ is the initial resistance of the gauge; and $\sigma_y$ is lateral stress.

By substituting Equation 4.7 into Equation 4.6 we get;

$$Y_g = 0.14995 \times (4120\epsilon_v^2 + 1160\epsilon_v) + 6.554 \qquad (4.10)$$

A key aspect of the interpretation of lateral gauges involves the elastic-plastic transition and the calculation of the relative change in resistance ($\Delta = \frac{\Delta R}{R_0}$) at which the elastic-plastic transition occurs. Equation 4.11 defines the elastic response of the gauge. Notably, in the elastic regime, gauge response depends on both the matrix properties (i.e. Poisson's ratio ($v_m$) and longitudinal modulus of the matrix material ($M_m$)) as well as the elastic properties of the gauge (longitudinal modulus ($M_g$) and shear modulus ($G_g$)).

$$\Delta_{el} = \frac{3.45}{M_g}\beta\sigma_y^m \qquad (4.11)$$

where;

$$\beta = [1 + \frac{2G_g}{M_m}(\frac{1 - v_m}{v_m})] \qquad (4.12)$$

By substituting Equation 4.9 into Equation 4.11 we get;

$$\Delta_{el} = \frac{3.45}{M_g}\beta(P - \frac{1}{3}Y_g) \qquad (4.13)$$

and by substituting for pressure and yield strength in 4.13 using Equation 4.10 we get;

$$\Delta_{el} = \frac{3.45}{M_g}\beta[(4120\epsilon_v^2 + 1160\epsilon_v) - \frac{1}{3}(0.14995 \times \ldots$$
$$(4120\epsilon_v^2 + 1160\epsilon_v) + 6.5542)] \qquad (4.14)$$

This may be re-arranged to give;

$$\Delta_{el} = \frac{3.45}{M_g}\beta[(1 - \frac{1}{3} \times 0.14995)\epsilon_v^2 + 1160(1 - \frac{1}{3} \times \ldots$$
$$0.14995)\epsilon_v - \frac{1}{3} \times 6.5542] \qquad (4.15)$$

Equating the elastic and plastic definitions of $\Delta$, i.e. making Equation 4.8 = Equation 4.15, we get;

$$(9.89\epsilon_v^2 + 3.45\epsilon_v + (5.17 \times 10^{-4}) = \frac{3.45}{M_g}\beta[4120(1 - \frac{1}{3} \times \ldots$$
$$0.14995)\epsilon_v^2 + 1160(1 - \frac{1}{3} \times 0.14995)\epsilon_v - \frac{1}{3} \times 6.5542] \quad (4.16)$$

Re-arranging and collecting like terms gives;

$$[9.89 - \frac{3.45}{M_g}\beta \times 4120(1 - \frac{1}{3} \times 0.14995)]\epsilon_v^2 \ldots$$

$$+[3.45 - \frac{3.45}{M_g}\beta \times 1160(1 - \frac{1}{3} \times 0.14995)]\epsilon_v \ldots$$

$$+[5.17 \times 10^{-4} + 3.45 - \frac{3.45}{M_g}\beta \times \frac{1}{3} \times 6.5542] = 0 \qquad (4.17)$$

This is a quadratic equation for the critical value of $\epsilon_v$, i.e. the volumetric strain at which the elastic-plastic transition of the gauge takes place. The coefficients for this equation are:

$$a = 9.89 - \frac{3.45}{M_g}\beta \times 4120(1 - \frac{1}{3} \times 0.14995) \qquad (4.18)$$

$$b = 3.45 - \frac{3.45}{M_g}\beta \times 1160(1 - \frac{1}{3} \times 0.14995)]\epsilon_v \qquad (4.19)$$

$$c = 5.17 \times 10^{-4} + 3.45 - \frac{3.45}{M_g}\beta \times \frac{1}{3} \times 6.5542 \qquad (4.20)$$

Finally, the quadratic may be substituted back into Equation 4.7 in order to calculate $\Delta_{CRITICAL}$. This gives the pressure at which the elastic-plastic transition occurs and is the locus that differentiates how the piezoresistive (i.e. pressure-dependent) response of the gauge must be interpreted. At shock states resulting in a relative change

in resistance that is less than or equal to the critical value/pressure, Equation 4.11 (elastic response) is used to solve for $\sigma_y$. Conversely, at shock states resulting in a relative change in resistance that is greater than the critical value, Equation 4.9 (plastic response) is employed. In the plastic regime, the pressure (P) in Equation 4.9 is calculated from the the quadratic constants derived above. This allows for the yield surface of the manganin to be calculated (Equation 4.6) and, ultimately, for the lateral stress component ($\sigma_y$) to be determined (Equation 4.9).

Calibration of the electrical response of the lateral gauges was determined using the same methodology as that employed for longitudinal type LM-SS-125CH-048 gauges, i.e. sequential placement of a series of seven resistors of increasing resistance across the gauge circuit. Again, this simulated the passage of the shock across the gauge. The resultant change in voltage with resistance was recorded and a polynomial fit applied to the data. This allowed accurate conversion of raw voltage data to a relative change in resistance ($\Delta R$ in Equation 4.8). The use of an 'if statement' in Microsoft Excel$^{\circledR}$ further allowed the ability to differentiate between elastic/plastic treatment of the data, with $\Delta_{CRITICAL}$ being the controlling value.

## 4.3 Ultrasonic Diagnostics

By measuring the velocities at which longitudinal and shear waves are able to propagate within a material it is possible to calculate a number of its elastic properties. These may include bulk, shear, longitudinal, and Young's moduli; Poisson's ratio; and the material's bulk sound speed. Longitudinal and shear wave speeds for the adipose and skeletal muscle tissues investigated in this work were determined ultrasonically using Panametrics quartz transducers. The typical design features of a piezoelectric transducer are shown in Figure 4.8. Notably, the active element in this class of transducer is comprised of a piezo or ferroelectric material (e.g. quartz or barium titanate). This component essentially converts (electrical) excitation energy into ultrasonic energy.

Ultrasonic transducers of relatively low frequency (0.5 - 1 MHz) were used to introduce longitudinal and shear waves into the investigated materials/tissues. This effectively maximised the wavelength of the ultrasonic disturbance ($\lambda = c/f$), allowing for maximum penetration in the highly attenuating media. Measurements were taken using a Panametrics 5077PR pulser-receiver in either the pulse-receive configuration, i.e. with one transducer both introducing and receiving the reflected wave, or in the through-transmission configuration, with one transducer placed either side of the sample material. Couplant is typically required in the examination of metals in order to allow for shear waves to be transmitted into the surface. However, an agent of this nature was not required to successfully introduce longitudinal or

shear wave disturbances in the tissues examined here. Wave interactions were measured in samples ranging from 3 to 5 mm in thickness.

A typical response signal for a shear wave disturbance within porcine skeletal muscle is presented in Figure 4.9. The waveform at the bottom of Figure 4.9 is the electrical output from a Tektronix Tek P6139A voltage probe, which measures the time period over which excitation energy (voltage) is supplied to the active element of the transducer. Thus, any measured response outside of this range must be a reflection of the introduced disturbance. Notably, the response presented in Figure 4.9 was obtained in the through-transmission mode of operation, i.e. with one transducer placed either side of the sample.

The transducer signal in Channel 1 shows two clearly resolved wave packets - one corresponding to the incident distrubance; the other to the received disturbance. By selecting corresponding/matching peaks or troughs within the respective incident and received wave packets it is possible to determine their temporal separation. As the thickness of the sample being examined is known, this allows the velocity of the propagating disturbance to be determined. Calculation of ultrasonic wave velocity was identical for both longitudinal and shear wave disturbances.
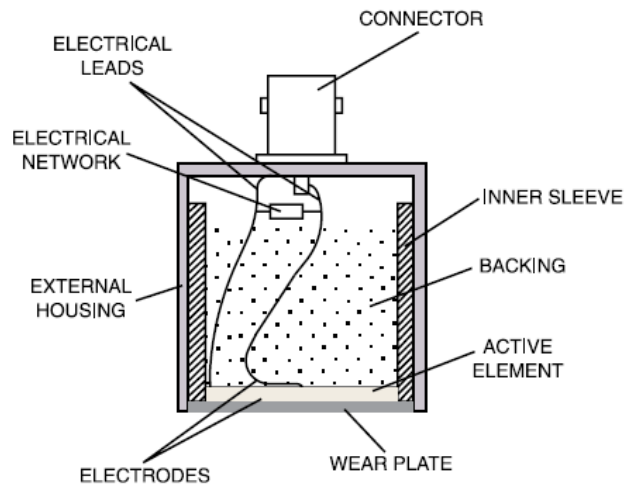
Figure 4.8: Generalised design characteristics of ultrasonic piezoelectric transducers [67]
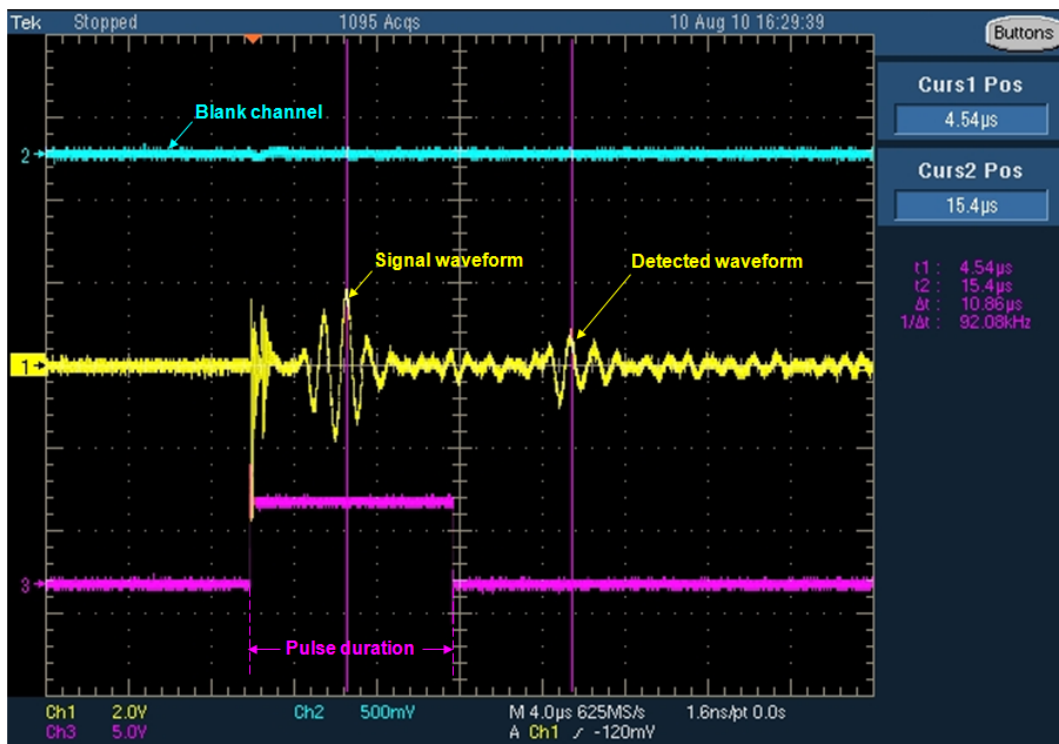


Figure 4.9: Incident and detected shear wave packets obtained from ultrasonic measurements within porcine skeletal muscle using the through transmission mode of operation

## 4.4 Transmission Electron Microscopy (TEM)

Transmission Electron Microscopy (TEM) is a technique that may be used to visualize structures that are present within biological samples. Its main advantage over optical methods is its ability to resolve images at significantly greater levels of magnification. With respect to the examination of skeletal muscle, it provides sufficient resolution to allow for detailed examination of the ultrastructure of the tissue, i.e. the sub-units comprising muscle fibres. Sewry et al. [68] presented an overview of the role of TEM in the diagnosis of muscular disorders and diseases. Specifically, TEM's ability to resolve structures/components such as intra-muscular nerves, mitochondria, the sarcoplasmic reticullum, and nuclei within the tissue was discussed by these authors. Other examples of the role of TEM in the study of muscle tissue damage/disease include the diagnosis of Marinesco-Sjögren syndrome [68] and the study of necrosis, which may be caused by toxins such as snake venoms [69, 70].

There are three main reasons why non-optical methods might be sought by the microscopist. These are: (i) to achieve higher levels of resolution than are offered by optical methods; (ii) to visualize structural components within a material that would otherwise remain opaque under optical wavelength, or; (iii) to determine the physical properties of a sample using complimentary diagnostics such as electron back-scattered diffraction (EBSD) or energy/wavelength dispersive x-ray emissions (EDX/WDX) [71]. Secondary diagnostic

techniques, however, are beyond the scope of this work.

The relatively large wavelength of light ($5 \times 10^{-5}$ m) limits its ability to resolve objects that are smaller than $\sim 1\ \mu$m . In contrast, the wave-like characteristics of electrons in a 100 kV electron microscope are approximately $3.5 \times 10^{-12}$ m in length, allowing for up to 100, 000 times magnification and objects within the order of $10^{-9}$ m in size to be resolved [72]. An acceleration of 100 kV gives each electron an energy, E = 100 keV. One electron volt (eV) is equivalent to $1.6 \times 10^{-19}$ Joules and the wavelength ($\lambda$) associated with the electrons accelerated with this voltage is given by the following De Broglie equation:

$$\lambda = \frac{h}{\sqrt{2Em_e}} \tag{4.21}$$

Where $h$ is Planck's constant and $m_e$ is the electronic mass.

A transmission electron microscope (TEM) typically comprises an electron source; condenser lenses; a sample chamber; an objective lens; an intermediate lens; and a final imaging stage, which may comprise a scintillator placed on a photomultiplier tube or a charge-coupled device (CCD), as is found in digital cameras. A scintillator is a semi-transparent material that emits a burst of light when ionizing radiation, such as an electron beam, passes through it [71]. A schematic of the basic components of an electron microscope is presented in Figure 4.10.

TEM microscopes typically operate under vacuum. This serves two
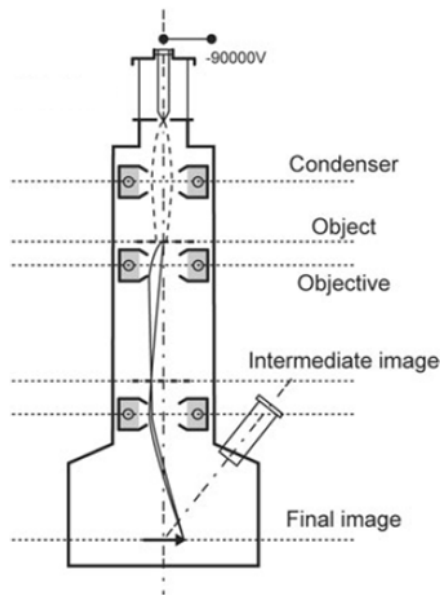
Figure 4.10: Schematic showing the general features of a transmission electron microscope (adapted from [71])

main purposes. The first is to prevent electrical arcing between the large potential difference (e.g. 100 kV) used to accelerate electrons towards the sample. The second is to increase the mean free path of the electrons. Maximizing the mean free path ensures that collisions between the electrons and gaseous atoms within the microscope column are reduced to negligible levels.

A number of key differences exist between SEM and TEM apparatus. However, the main difference is the type of electron interaction seen by the sample. In order to allow for electron transmission, i.e. the passage of electrons, samples to be used in TEM are sectioned very thin (<100 nm). Conversely, thickness is less of an issue with SEM systems. This is due to the fact that image formation by SEM systems is based upon either variations in the intensity of back-scattered elec-

trons or x-ray emission, which results from inelastic collisions between the primary beam and electrons bound in the surface of the sample [71]. Another difference between the two types of electron microscope is that samples must be conductive in conventional SEM's in order to allow electrons to be accelerated onto their surface. This is typically achieved by sputter-coating the sample with gold.

There are two main types of 'electron gun' that are used to generate electrons within an electron microscope. These are the thermionic gun and the field emission gun. The thermionic gun typically involves heating a tungsten filament to temperatures in excess of 2700 K, which produces large quantities of both light and electrons. The filament is held in a strong negative potential (cathode) with respect to the anode and the remainder of the microscope. This potential difference rapidly accelerates the electrons produced by the filament towards the anode, forming a beam as they are emitted through a circular hole at its centre. Conversely, the field emission gun works upon the principal that electrons can be extracted from the surface of a metal if a sufficiently high electrical field ($>10^9$ V/m) is passed through it. The field emitter, which is usually constructed from tungsten, however, requires a very fine point (0.1 $\mu$m) in order to allow for such a high field to be applied [73]. This means that the vacuum within the microscope must be much stronger, resulting in increased costs.

Lenses within TEM systems are typically electromagnetic (EM). If electrons enter an EM lens in such a manner that they are not aligned with the 'optical' axis, they will experience a force ($F = BeV$) that

will cause them to enter an ever-tightening helical path that converges to a point. This principle is similar to that of how light is focused by a glass lens. In the above relationship: $F$ is Force in Newtons; $B$ is flux density (strength of the magnetic field) in Teslas; $e$ is the charge of the electron $(1.6x10^{-19})$; and $V$ is the voltage.

The condenser lenses/lens sit(s) below the electron gun and control(s) the diameter of the beam as it hits the sample. This not only gives the user control of the area of the sample under influence from the beam, but also the intensity of illumination or "brightness". Below the condenser section sits the specimen. This is introduced into the column via a specimen holder and air-lock system. The specimen holder usually comprises a long rod, capable of supporting small samples or sample grids onto which smaller specimens may be attached. As the sample is inserted into the objective lens, the sample rod must be capable of both very accurate adjustment and remaining very stable once the correct position has been determined.

The objective lens forms the first image in an electron microscope, which usually has a magnification of 50-100 times [73]. This image is then further magnified by the intermediate lens/lenses and projector lens. Older TEM microscope images were captured using photographic film which was accurately exposed using a controlled shutter mechanism. Today, however, TEM images are focused onto charged couple devices (CCD's) of the type found in digital cameras. A live image feed is sent to the user to allow for the control of image position, focus, magnification, and ultimate image capture.

| Manufacturer | $Hitachi$ |
|---|---|
| Model | $H - 7650$ |
| Lens configuration | $6 - stage\ lens\ system$ |
| Focusing | $Autofocus/sigmation\ using\ CCD\ device$ |
| Operational voltage | $120\ KV$ |
| Capture device | $10\ Megapixel\ CCD\ camera\ (type\ A\ only)$ |
| Achievable resolution | $0.2\ nm\ (lattice\ image)$ |

Table 4.2: Specifications of the Hitachi H-7650 electron microscope used to visualize skeletal muscle samples in this body of work

Information about the type of electron to image samples of both virgin and shocked skeletal muscle in this work is provided in Table 4.2.

## 4.5 Computational Modelling - ANSYS® AUTODYN

ANSYS® AUTODYN has been used in this research study to aid the development of a soft-capture system allowing for the shock recovery of skeletal muscle tissue. As such, a detailed overview of the hydrocode and software package are provided in this section.

The hydrocode ANSYS® AUTODYN is a widely used numerical application allowing for the simulation of non-linear dynamic events. Examples of its use within the literature include an investigation of the penetration and perforation of reinforced concrete by a steel ogival-nosed projectile [74]; simulation of stress-wave-induced fractures within rock [75]; ballistic impact effects upon a Kevlar® helmet [76]; and a numerical approach looking at shock-induced damage beneath impact craters [77].

Within AUTODYN, direct control of model generation, pre- and post-processing, and the ability to specify output parameters are all presented to the user in a fully interactive, menu-driven environment. AUTODYN uses explicit, finite difference codes in which the conservation equations of mass, energy, and momentum are solved. These equations are listed below for the Lagrangian material description. The Lagrangian description provides a material description, i.e. a framework to which the material belongs. In contrast, the Eulerian description provides a spatial description. In this sense, material flows through a fixed framework. As the Eulerian description is better

suited to gaseous flow problems and the Lagrangian description better suited to "rigid" problems incorporating solid components, this body of work focuses purely on the Lagrangian approach to modelling. The conservation equations provided below adhere to this methodology and incorporate units of density ($\rho$), velocity ($v_i$), specific energy ($e$), the stress tensor ($\sigma_{ij}$), and external force per unit mass ($f_i$). Subscripts in the formulae represent standard tensorial notation.

$$Conservation\ of\ mass: \frac{D\rho}{Dt} + \rho\frac{\delta v_i}{\delta x_i} = 0 \qquad (4.22)$$

$$Conservation\ of\ momentum: \frac{Dv_i}{Dt} = f_i + \frac{1}{\rho}\frac{\delta\sigma_{ji}}{\delta x_j} \qquad (4.23)$$

$$Conservation\ of\ energy: \frac{De}{Dt} = f_i v_i + \frac{1}{\rho}\frac{\delta}{\delta x_j}(\sigma_{ij}v_i) \qquad (4.24)$$

In addition to the conservation equations, an equation-of-state, which relates the density (or volume) and internal energy (or temperature) of the material with pressure is required (see Equation 4.25). This accounts for both compressibility effects within the model, i.e. change in density, and irreversible thermodynamic changes (shock heating) [78]. Once initial and boundary conditions have been applied to the model, the constitutive relation (see Equation 4.26) provides a solution for the response of materials to shear [74]. This

relationship also allows stress to become a function of internal energy (E), strain ($\epsilon$), strain-rate ($\dot{\epsilon}$), and damage (K) [78]. In AUTODYN, key material properties, such as yield stress and shear modulus, are either manually entered by the user or form part of the material description that has been selected from the inbuilt materials library.

$$Equation\ of\ state: P = P(\rho, E) \qquad (4.25)$$

$$Constitutive\ model: \sigma_{ij} = f(\epsilon_{ij},\ \dot{\epsilon}_{ij},\ E,\ K) \qquad (4.26)$$

$$Courant - Friedrich - Levy\ criterion: \Delta t < \frac{\Delta x}{c} \qquad (4.27)$$

In an explicit time-integration, the finite difference time-step is controlled by the Courant-Friedrich-Levy (CFL) criterion [74]. This states that the time-step ($\Delta t$) is less than the time for a sound signal with velocity $c$ to traverse the grid spacing $\Delta x$ (see Equation 4.27). When modelling shock wave interactions, this implies that the time-step is smaller than the time taken for the shock ($c$) to traverse a single grid spacing. This ultimately dictates that the shock interaction within the model can be studied in detail.

Initially, the AUTODYN user is prompted to specify units of length, mass, and time for the model. The required type of symmetry is also

to be specified and may be either 2D axial, 2D planar, or of three-dimensional (3D) geometry. 2D axial symmetry is beneficial as it may effectively half the number of cells needed to run a complete (symmetrical) model.

Cells are formed from a lattice comprised of Lagrangian lines, which are joined at discrete points called nodes. With respect to the applied force, adjacent nodes can be either stretched apart or compressed together; thus altering the shape and size of cells. This is useful in the sense that, as mass remains constant (Equation 4.22), a decrease in the overall size of a cell relates to an increase in material density. While planar symmetry is beneficial when surface artifacts are to be studied, e.g. impact-induced crack propagation, 3D geometry is best suited to the testing of more complex components and structures (vehicle hulls, bridges, etc.). Due to the experimental setup adopted in this work and the subsequent one-dimensionality of the loading experienced by target materials (i.e. plate-impact experiment), 3D model geometry was deemed an unsuitable approach. Here, investigations have been limited to models comprising 2D axial symmetry alone.

Parts within a model are defined using a Cartesian coordinate system. This establishes initial boundary conditions and allows cell size - and thus the number of cells in a given direction - to be specified. Initial conditions, such as velocities and temperatures, may also be assigned to parts. An example of a Lagrangian grid applied to a basic model is presented in Figure 4.11. This model forms part of an attempt to quantify the stain-rate experienced at the interaction site of
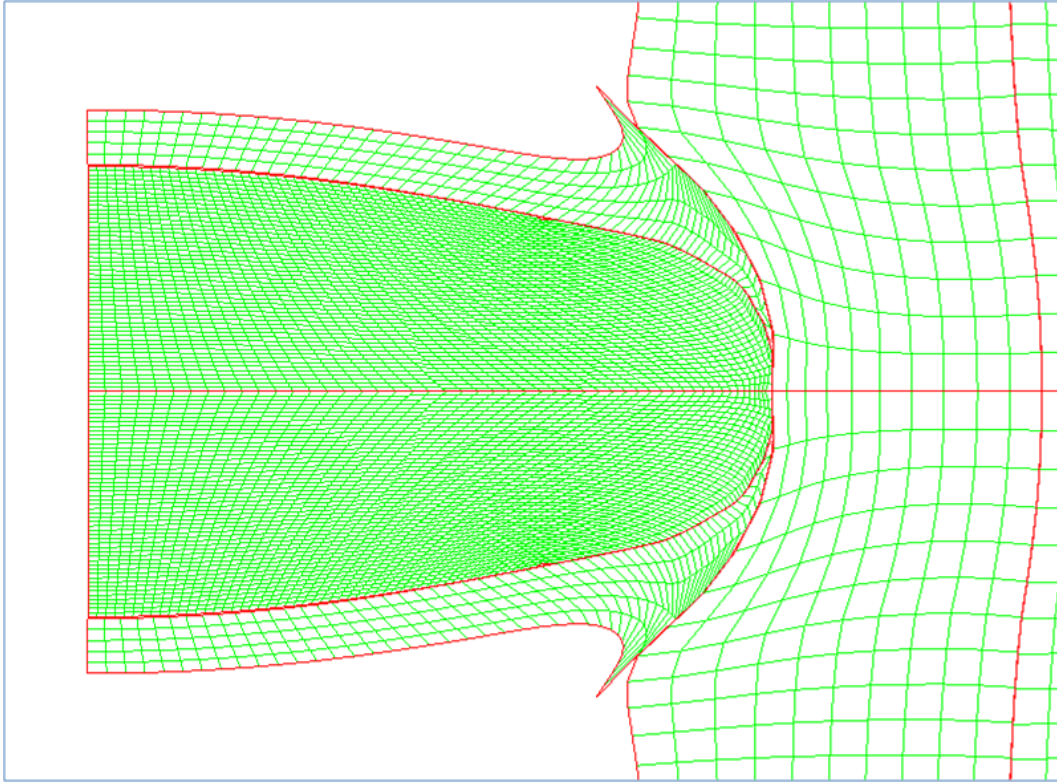
Figure 4.11: Lagrangian mesh applied to a basic model - an investigation into the typical strain-rate experienced at the interaction site of an ogival-shaped projectile impacting a steel armoured target

a lead-cored, copper-jacketed, ogival projectile when impacting a steel armoured target. Additionally, the model was constructed in order to highlight the ability to selectively control grid size - an important feature when it is necessary to optimize model run-time while retaining the quality of output data.

The Lagrangian description is not without limitations. The most significant problem associated with this type of mesh arises from large cell/grid distortions. Unfortunately, such disruptions are commonplace when modelling high-rate dynamic events such as projectile/armour and strong shock interactions. Mesh points (nodes) fol-

low particle paths within a material. Thus, when one considers the interaction between a projectile and an armour material within a Lagrangian model, it is apparent that cell distortion will be most pronounced at the projectile/target interface. In some cases, this may lead to an overlap of the nodes that distinguish one cell from another. This creates an area of negative mass within the model: an entirely undesirable property. To overcome this problem, an erosion model is typically introduced into the simulation. By pre-defining a tolerance on the geometric strain that cells are permitted to experience, the user is capable of preventing nodal overlap. However, by removing cells from a model, the mass associated each cell is also removed. The net result of such action is that neither the conservation of mass, energy, nor momentum are entirely conserved. In order to minimize the effect of cell erosion upon the integrity of the modelled result, the level of strain permitted within cells is typically quite high, e.g. 200 %. Another method allowing for the validation of Lagrangian models is to perform both simulations and experiments in parallel. Modelled results are rarely considered to be robust without the backing of experimental data.

# Chapter 5

# Research Materials

## 5.1 Skeletal Muscle Tissue

Two types of porcine skeletal muscle tissue were investigated in this body of work. These were: (a) the longissimus dorsi muscle of a middle-white swine (aged 6 months at the time of slaughter) and; (b) a commercially-available unsmoked gammon joint, marketed by Sainsbury's Supermarkets Ltd (United Kingdom) as part of their 'be good to yourself' range (<4 % fat content). These two materials were selected in an attempt to highlight any key differences that may exist between the shock data for tissue containing additives to preserve shelf-life, i.e. the commercially-available tissue, and fresh, unaltered tissue (middle-white). It seems reasonable to suggest that the commercially available tissue - comprising m.semitendinosus, m.semimembranosus, and m.biceps femoris (amongst lesser muscles) [79] - and the middle-white tissue (m.longissimus dorsi) are, to a first approximation, analogous to human skeletal muscle tissues.

The in-fibre and cross-fibre physical appearance of the commercial

muscle tissue is highlighted in Figure 5.1. While a fibrous structure may be evident from these images, it is worth noting that the average fibre diameter for porcine m.longissimus (i.e. the middle-white muscle examined in this work) is approximately 60 $\mu$m [80, 81]. Further, Ono et al. [82] present measured cross-sectional areas for the fibres of 12 different porcine muscles, measured at various stages of animal growth (20, 60, and 90 Kg body mass). The cross-sectional areas presented by Ono et al. for the m. biceps femoris (a likely component within the commercial porcine muscle tissue tested here) correspond to maximum fibre diameters of 47.5 $\mu$m at 20 kg and 80 $\mu$m at 90 kg body mass. Thus, whilst a fibrous appearance is evident within both the cross-fibre and in-fibre physical appearance of the commercially available tissue (Figure 5.1), this is not an accurate representation of fibre size. This attribute is merely due to the arrangement of fibres into bundles, i.e. perimysium-bound fascicles (see Section 1.2.1).

In addition to the two tissue types described above, the shock response of a homogenized variant of the commercially-available tissue was also investigated in this work. Homogenization of this porcine tissue involved two key steps. These were: (i) initial disruption of the tissue's fibres using a food processing unit prior to: (ii) a secondary refinement process in which the disrupted material was milled into a fine paste (i.e. ground between two hard surfaces). Following these stages, efforts were taken to remove any tendinous deposits found within the material. Whilst comprising the same biological make-up as the non-processed variant of the tissue (actin and myosin protein
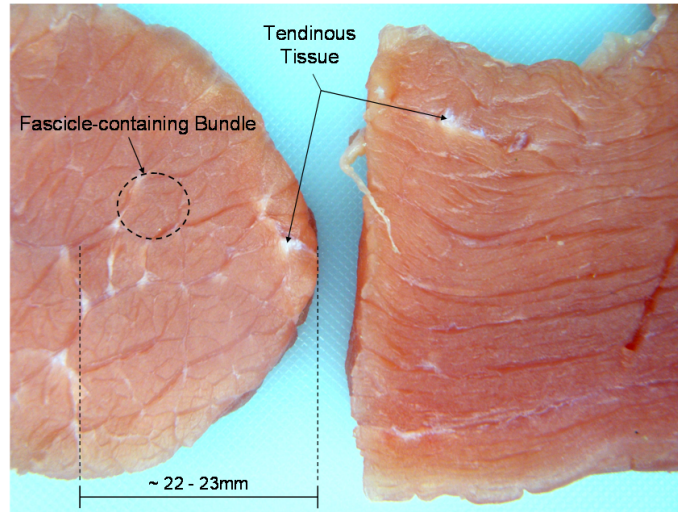
Figure 5.1: Photograph highlighting the physical appearance of both in-fibre and cross-fibre commercial tissue specimens

filaments, cellular fluid, etc.), this homogenized variant arguably possessed none of the quasi-organised structure of skeletal muscle, i.e. orientation-specific fibres bound by connective tissues. As such, it was reasoned that any difference between the response of the homogenized and virgin tissue samples to shock should only be attributable to their differing structural arrangements.

**Light Microscopy of Muscle Tissue Samples**

Basic structural analysis of thin ($\sim$1 $\mu$m) sections of the chosen research materials was performed using transmission light microscopy. This served three purposes. Firstly, the technique allowed for simplistic comparison of the two tissues which, as was discussed in section 5.1, originated from different porcine skeletal muscles. Secondly, the technique provided information regarding the spatial distribution of the fibres/fibre bundles and the typical fibre diameter present within the respective samples. Finally, the analysis was performed so that regions of interest might be highlighted for successive and more detailed structural examination using the higher resolution transmission electron microscopy (TEM) technique.

In order to view samples under either light or electron microscope, an initial fixation and embedding process was performed on each tissue sample. This process was involved fixation in 2.5 % glutaraldehyde/0.1 M phosphate buffer (pH 7.2), post-fixation in 1 % osmium tetroxide (staining agent), a rinsing/wash stage, and dehydration with a graded ethanol series (50, 70, and 90 %). Finally, the respective samples were embedded in 1:1 propylene oxide/embedding resin.

The purpose of any fixative is: (a) to 'fix' the biological specimen, i.e. to prevent it from degrading/decomposing by natural processes, and; (b) to maintain (as closely as possible) the virgin structure of the tissue for viewing purposes. An additional requirement of any fixative is to ensure that minimal artefacts are introduced to the specimen as a result of its use. Despite this, the process of fixation for microscopic

examination purposes undoubtedly causes changes to the tissue upon which it acts. Provided the effects of the adopted and standardized fixing process are known, the user can eliminate them from their interpretation of imaged results. The gluteraldehyde and phosphate buffer solution used here to fix the muscle specimens for microscopic analysis acts to bind the proteins of the tissue. Essentially, this preserves their cellular structures by preventing the proteins within them from unravelling and denaturing. The use of glutaraldehyde in a buffer solution is well documented as a suitable fixative for the visualisation of the cellular structure of skeletal muscle tissue, e.g. [83, 84].

Thin sections ($\sim$1 $\mu$m) of the tissues were made using a RMC Powertone PC (ultra-microtome apparatus) incorporating a diamond knife. These sections were then transferred to glass slides and stained using Toluene Blue, thus enhancing the contrast already provided by osmium tetroxide. When viewed under a light microscope, insufficient contrast would have been afforded without this additional staining. Haemotoxylin and/or eosin (agents commonly used to visualise cellular structures within tissues) [85, 86] were not used as they would not have been able to penetrate the resin in which the tissue was bound. The tissue specimens were sectioned in both longitudinal (LS) and transverse (TS) orientations with respect to fibre direction. Figures 5.2 and 5.3 show LS and TS light micrographs of the commercially-available muscle tissue, respectively.

The average diameter of the muscle fibres present within the commercial muscle tissue - shown in Figure 5.2 - hold good agreement with
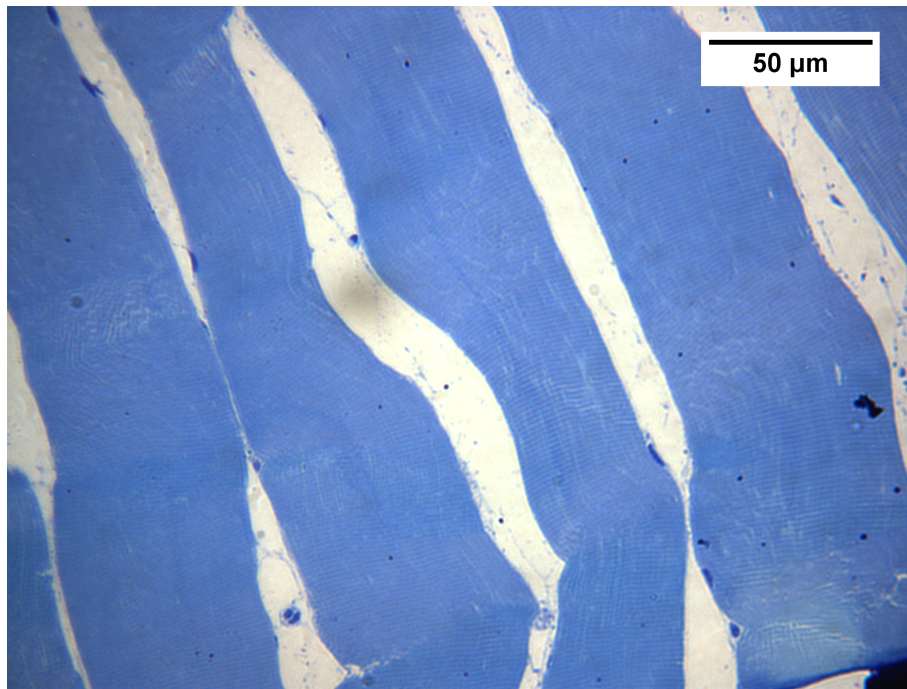
Figure 5.2: Light micrograph of a longitudinal section through the commercially-available muscle tissue
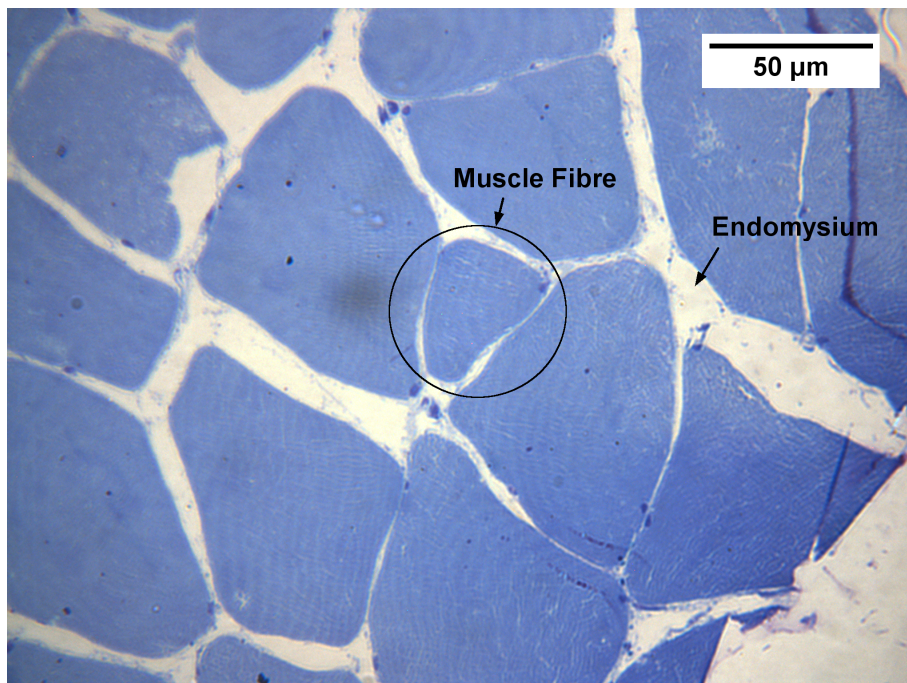


Figure 5.3: Light micrograph of a transverse section through the commercially-available muscle tissue
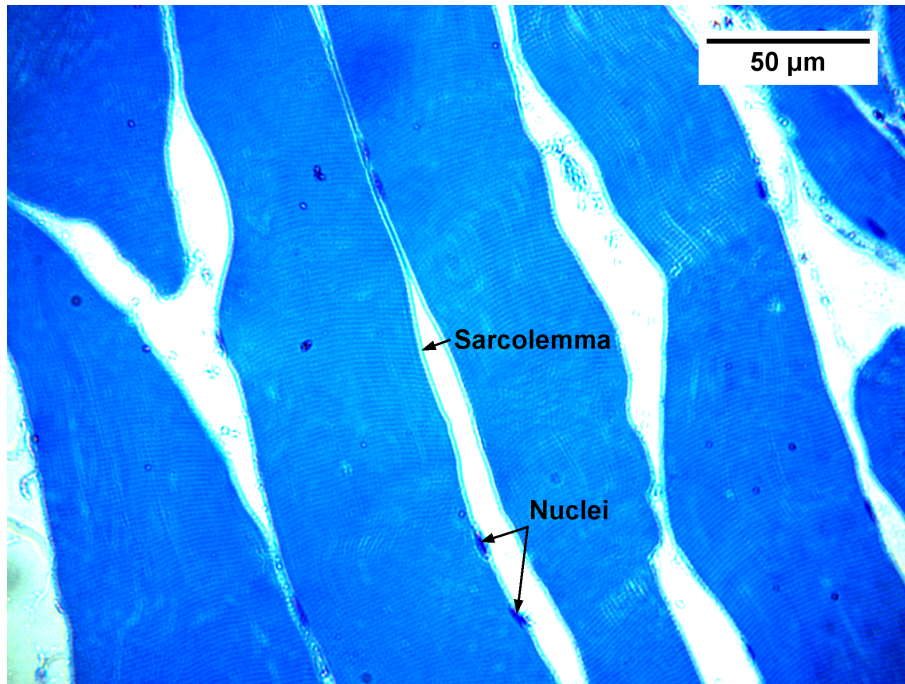
Figure 5.4: Enhanced image of a transverse section through the commercially-available muscle tissue - showing the sarcolemma and nuclei

fibre diameters found within the literature, e.g. Ono et al. [82]. The two-stage staining process (osmium tetroxide enhanced with toluene blue) has provided good resolution of the striations present within the fibres. Additionally, the staining has provided enhanced contrast to the connective tissue found between the muscle fibres, i.e. the endomysium. Figure 5.4 is an enhanced version of Figure 5.2, higlighting the connective tissue that surrounds individual muscle fibres (the sarcolemma) and nuclei of the muscle cell.

The light micrographs presented in Figures 5.2 to 5.6 indicate that both the commercially-available and middle-white tissues possessed good levels of structural integrity. However, the spatial separation between the muscle fibres of the two materials is dissimilar, i.e. much
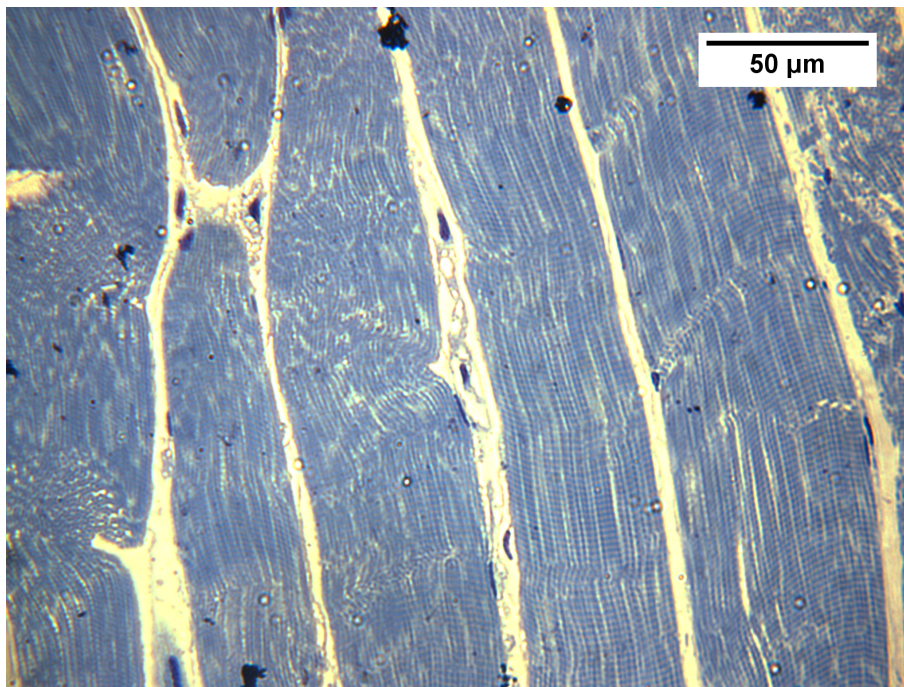
Figure 5.5: Light micrograph of a longitudinal section through the middle-white muscle tissue
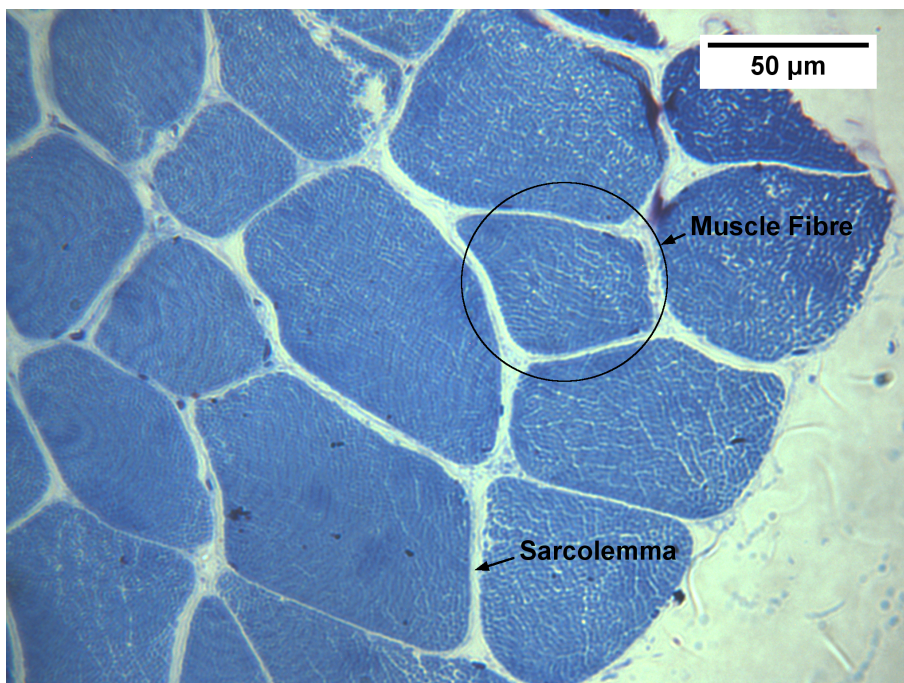


Figure 5.6: Light micrograph of a transverse section through the middle-white muscle tissue

larger spacing is apparent within the commercially-available tissue than the middle-white tissue. This difference may relate to the treatment of the two materials prior to chemical fixation. Specifically, the commercially-available tissue was subjected to a period of freezing, prior to being thawed to allow for chemical fixation, while the middle-white tissue was stored at 4°C prior to the treatment. Ayala et al. [87] found that formation of ice crystals in the inter-fibrillar spacings of skeletal muscle led to similar expansion as that shown in the light micrographs of the commercially-available tissue. Such expansion effects have also been shown to relate to the post-mortem time interval [88]. Despite altering the spatial separation of the fibres within skeletal muscle, freezing has been shown to have no discernible effect upon the ultrastructure of the tissue [89], suggesting that the protein-based filaments comprising its structure remain unaffected by the effects of freezing. Following analysis of the structures of the two tissue types, each was frozen. The shock data presented later in this work for skeletal muscle reflects such treatment.

**Transmission Electron Microscopy of Muscle Tissue Samples**

The initial preparation of both shocked and non-shocked tissues for examination by either TEM or optical methods in this work was identical (see Section 5.1). One key difference between the two preparatory methods (TEM versus light microscopy) was that sections to be examined by the electron microscope did not require the additional staining afforded by the toluene blue reagent, i.e. suffiecient contrast was attainable from the osmium tetroxide staining alone. An additional difference between the sections examined by the two microscopic methods was their thickness. Tissue sections viewed using TEM were much thinner (nominally 80 nm) than those examined using the light microscope ($\sim 1$ $\mu$m). In all cases, however, sample material was sectioned using a RMC Powertone PC (ultra-microtome apparatus). The transmission electron miscroscope used in the anylysis of tissue samples in this work was a Hitachi H7650. Samples were imaged using an operating voltage of 120 KV.

A micrograph showing a longitudinal section through a muscle fibre from the commercially-available tissue is presented in Figure 5.7. This figure highlights the inherent anisotropy of the materials structure, i.e. myofibres (a sub-unit of the muscle fibre) are visible in both longitudinal and transverse orientations. Fibre orientation within specific muscles, e.g. *m.triceps brachii* in the human arm, may also exhibit a variable degree of anisotropy. A longitudinal section of the tissues ultrastructure is presented in greater detail in Figure 5.8. The sarcomeres of the tissue, i.e. the repeat units within the myofibre that are
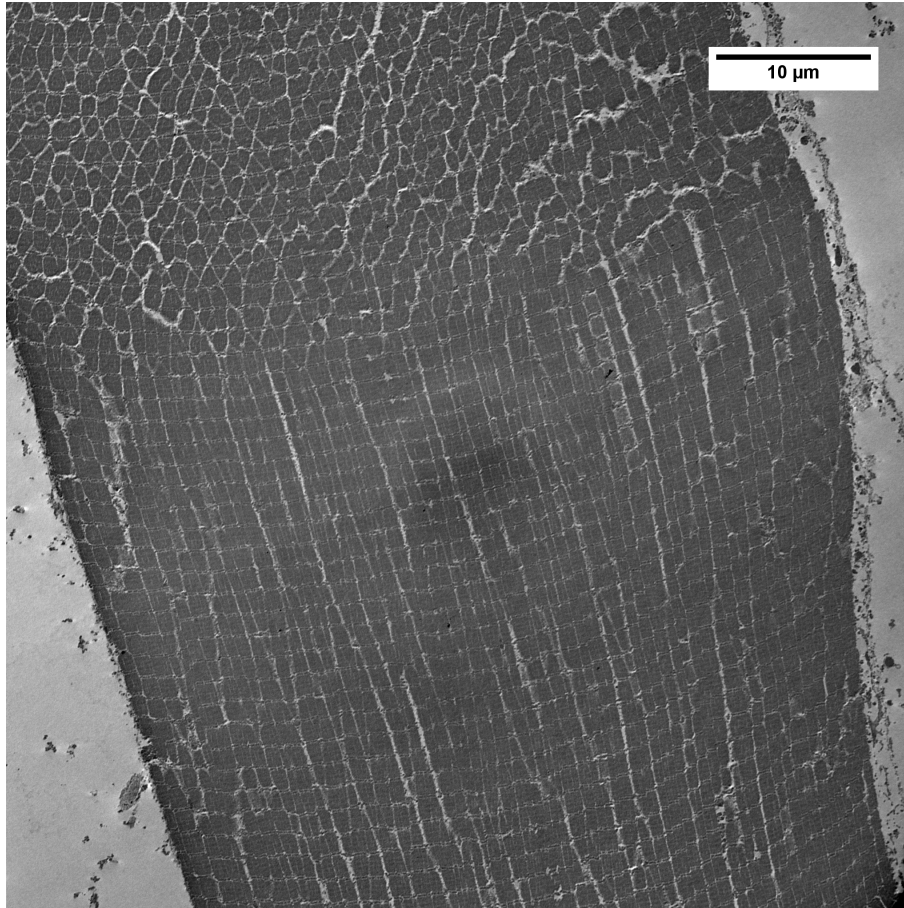
Figure 5.7: Transmission electron micrograph of a typical muscle fibre from the commercially-available porcine tissue (longitudinal section)

responsible for muscle contraction, are largely contiguous. Specifically, key features such as Z-disks (Z), I-bands (I), A-bands (A), and the M-line (M), are all intact. However, some evidence of inter-myofibrillar splitting may be observed (*).

The commercially-available tissue exhibits a more cohesive and consistent structure than the middle-white tissue - as evidenced in Figures 5.9 and 5.7, respectively. Specifically, Figure 5.9 shows existence of the widespread splitting of myofibres throughout the tissue sample. This feature was not apparent in the commercial tissue
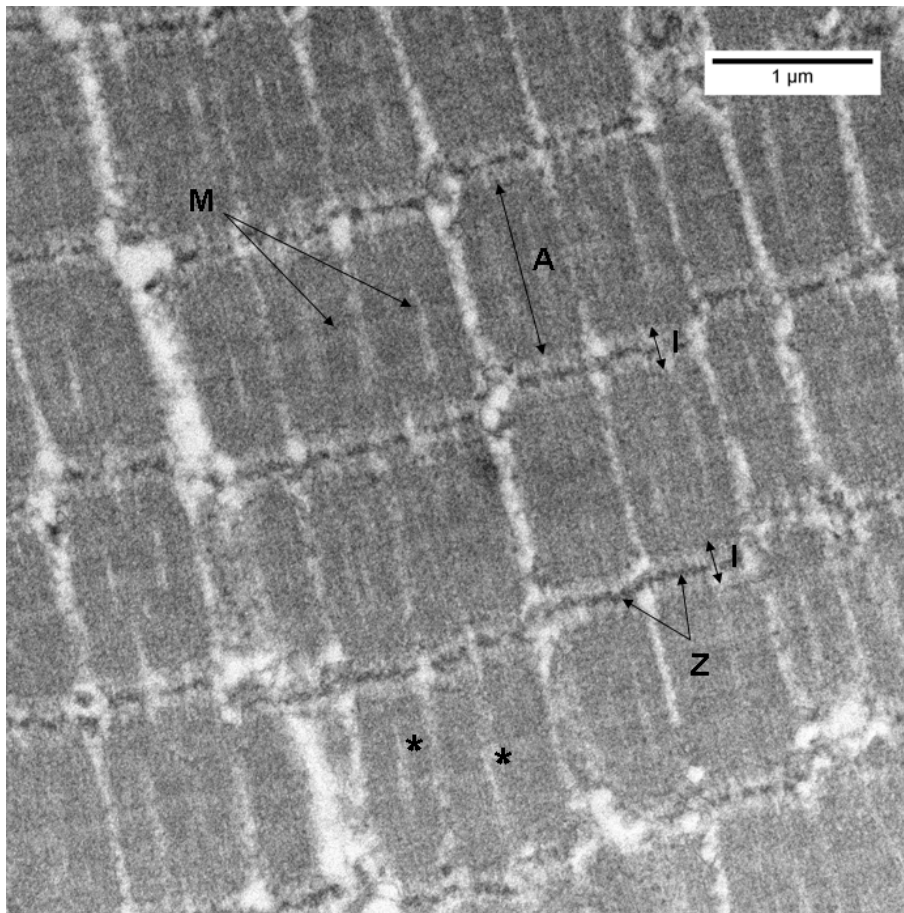
Figure 5.8: A detailed TEM micrograph of a longitudinal section through a muscle fibre (commercially-available tissue) where:

M = M-line; A = A-band; I = I-band

Z = Z-disk, and; * = inter-myofibrillar splitting
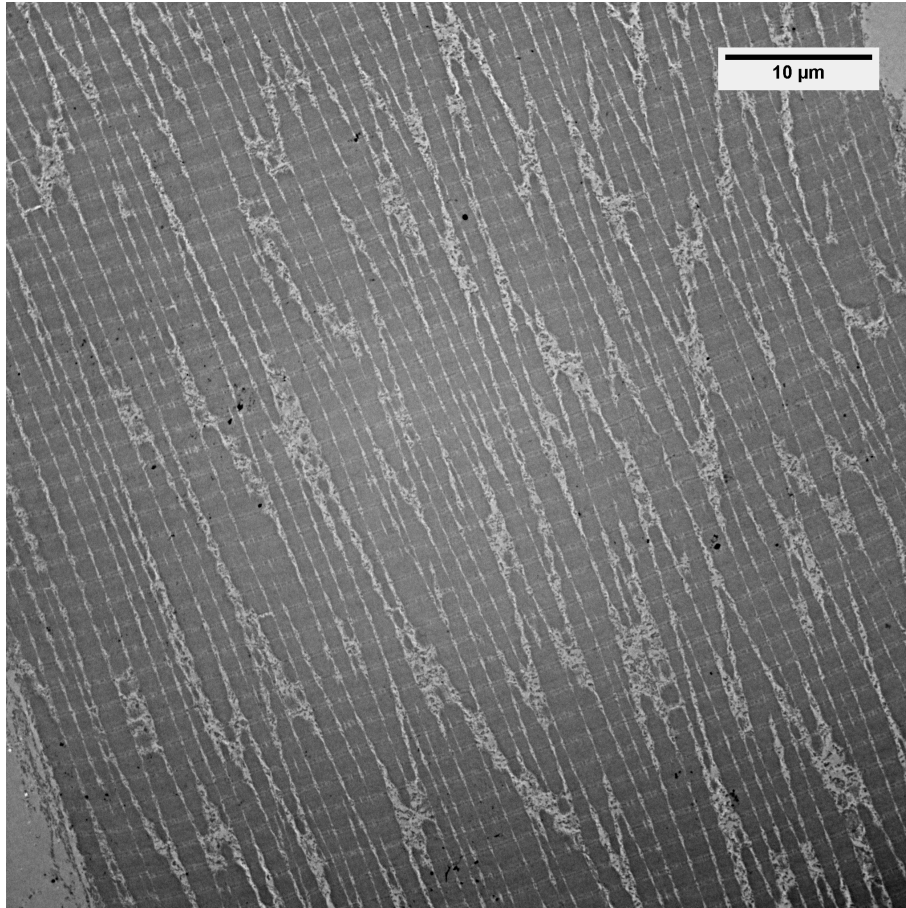
Figure 5.9: Transmission electron micrograph displaying a longitudinal section through a typical longissimus dorsi muscle fibre (middle-white tissue)
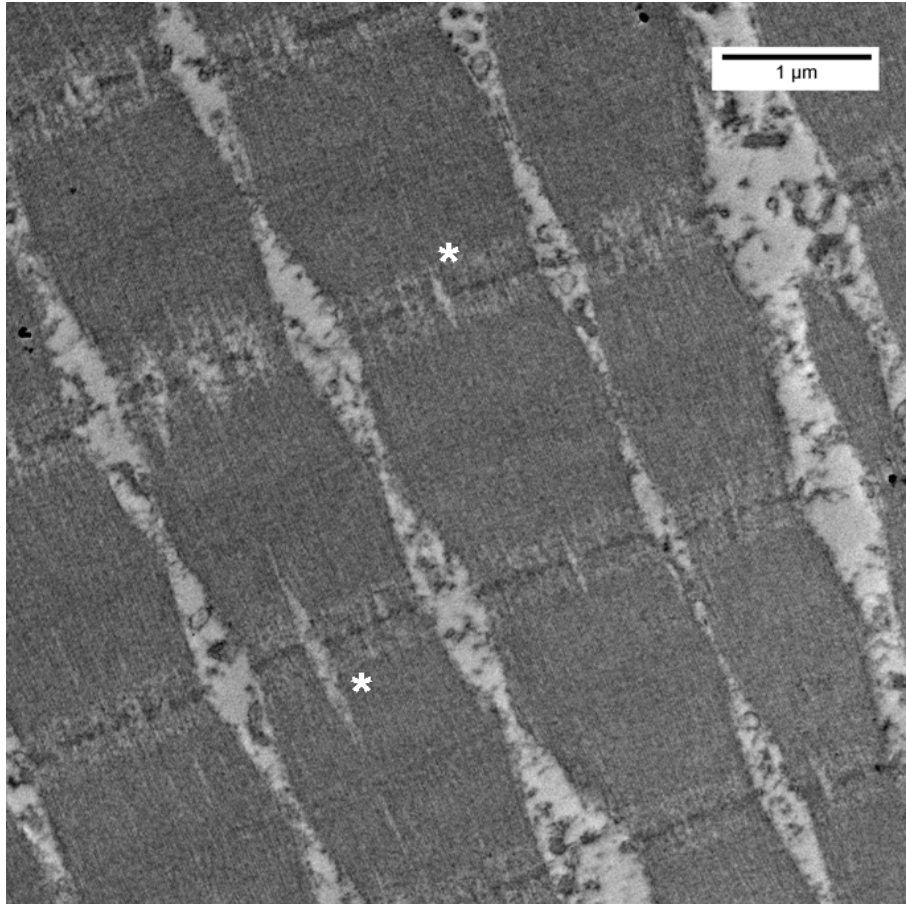
Figure 5.10: A detailed TEM micrograph of a longitudinal section through a muscle fibre (middle-white tissue) - * inter-myofibrillar splitting

sample. Absence of such features within the commercially-available product may possibly be attibuted to the preservatives added to the product. However, the exact cause of the damage is unknown and simply remains a feature of the middle-white sample material. Aside from this defect, key features within the ultrastructure of the middle-white tissue (Z-disks, I-bands, etc.) are clearly resolved and are suitably intact. In likeness with the commercially-available tissue, however, inter-myofibrillar (*) splitting is also shown to exist within the middle-white tissue's ultrastructure.

### 5.1.1 Muscle Tissue Density and Water Content Analysis

The initial density of a material is a key parameter used in the determination of many Hugoniot relationships. As such, the density of the two tissue types adopted in this work was measured using a Micromeritics AccuPyc 1330 Gas Pycnometer. This apparatus determines the density of a sample by measuring the pressure change of helium between a calibrated volume and the measured cell chamber volume when the sample is present. Hence, a vital step in the analysis is to measure the mass of the sample. This is then programmed into the pycnometer prior to anaylsis and used to calculate sample density. The precision of the result from the apparatus is maximised by taking data across five consecutive runs. The tolerance, i.e. permitted spread, of data during the cycles is specified by the user. Due to the sensitivity of the apparatus to environmental temperature, daily calibration of this apparatus must be performed. The calibration process itself involves measuring the density of a ball bearing of known mass and volume with the calibration being achieved when the density is accurately recorded to a standard deviation of <0.0010 $g/cm^3$ over five cycles. A schematic of the AccuPyc 1330 Gas Pycnometer is presented in Figure 5.11.

The measured densities for the commercially-available and middle-white tissues are presented in Table 5.1. These values hold good agreement with the density value that is typically accepted for mammalian skeletal muscle within the literature (1.0597 $g/cm^3$) [90], [91].

Cellular fluid/water is a major constituent of both in vivo and ex
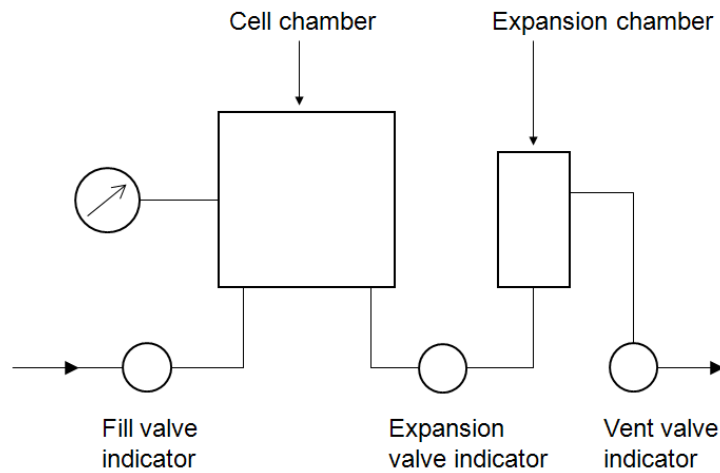
Figure 5.11: A schematic of the AccuPyc 1330 Gas Pycnometer

vivo muscle tissue (i.e. both within and outside of the body). As such, efforts were made to quantify the water content of the tissues under examination in this work. Samples ranging from 0.57 to 1.15 g were taken from the respective tissue types and dehydrated by one of two processes: (i) heating at $40 \pm 0.25$ °C for 24 hrs in a GENLAB General Purpose Incubator, or; (ii) dessication for 24 hrs in bright, open conditions. Three samples from each tissue type were exposed to each dehydration process. While no clear correlation was observed between percentage mass loss from the two tissue types, values ranging from 62.6 - 68.4 % were recorded, giving a clear indication that more than half of the composition of the tested samples (by mass) was fluid. A discernable difference between the achieved percentage water losses using the two dehydration processes was not detected.

Density was measured for both hydrated and dehydrated variants of the two tissue types. These values are presented in Table 5.1, highlighting that the natural, hydrated density of skeletal muscle is

an approximate match to that of water. Significantly, the densities recorded for the dehydrated tissues were greater than those of the hydrated samples. This suggests that - when in its natural state, i.e. as living tissue - the density of skeletal muscle is largely dominated by its relatively high water content. Essentially, the tissue exists as a swollen, fibre-based matrix. The errors associated with the density measurements presented in Table 5.1 reflect the range of densities measured by the gas pycnometer over five consecutive cycles.

| Tissue | Density $(g/cm^3)$ |
|---|---|
| Commercially-available | $1.0958 \pm 0.0003$ |
| Middle-white | $1.0892 \pm 0.0002$ |
| Commercially-available (dehydrated) | $1.2838 \pm 0.0011$ |
| Middle-white (dehydrated) | $1.2378 \pm 0.0006$ |

Table 5.1: Tissue density and water content

### 5.1.2  Determination of Elastic Constants

Longitudinal and shear wave velocities ($c_L$ and $c_S$, respectively) were determined for both the commercially-available and middle-white tissues. The wave velocity measurements were taken using two 1.0 MHz Panametrics quartz transducers in the through-transmission configuration, i.e. with a transducer placed either side of the sample material. Determination of these individual wave speeds has allowed successive calculation of bulk sound speed values ($c_0$) for the tissues (see Equation 2.27). Essentially, these values define the minimum velocity at which shock waves may propagate within the respective media ($u_p = 0$). Errors for $c_0$ were calculated from the range of measured longitudinal and shear wave velocities. Key elastic properties for the two muscle tissues are presented in Table 5.2.

The bulk sound speed values calculated for the two tissue types in this work hold good correlation with ultrasonic wave velocities determined for skeletal muscle tissue elsewhere, e.g. [92], [93]. However, somewhat lower longitudinal, shear, and bulk sound wave speeds are noticeable for the middle-white tissue than the commercial tissue. This reflects lower material stiffness, which may potentially be attributed to the relative 'freshness' of the sample or the lack of additives (anti-oxidants, salt, etc.) present within the tissue. Alternatively, this discrepancy in wave velocities may reflect the individual muscles from which the tissues were sourced.

Bulk moduli (K) were calculated for the respective tissue types (where $K = \rho_0 c_0^2$). These are also to be found in Table 5.2 and hold

good agreement with those reported in the ultrasound and acoustic microscopy literature [94].

| | Commercially-available | Middle-White |
|---|---|---|
| $c_L$ | 2.050 ($\pm 0.100$) | 1.930 ($+0.021$; $-0.025$) |
| $c_S$ | 0.985 ($\pm 0.035$) | 0.894 ($+0.072$; $-0.097$) |
| $c_0$ | 1.700 ($\pm 0.15$) | 1.631 ($+0.141$; $-0.087$) |
| $K$ | 3.188 | 2.897 |

Table 5.2: Key elastic constants for the selected muscle tissues

## 5.2  Adipose Tissue

The adipose material adopted in this work was a commercially-available lard manufactured in the UK by Matthews Foods PLC and retailed by the Co-operative Food Group under the product name Fresh Fields Lard. The material was chosen as an approximation of human fat tissues and adipose layers, due to its high fat content (c.99.8 %), and the requirement that such materials/simulants comply with ethical regulations for the testing of animal and human tissues. The adipose material was stored at 4 °C up until the point of target prepatation.

As with the skeletal muscle tissue, the density of the adipose material was determined using the Micromeritics AccuPyc 1330 Gas Pycnometer. A density value of $0.9451 \pm 0.006$ g/cm$^3$ was determined for the material at room temperature. As such, the densities of both the adipose material and the skeletal muscle tissues examined in this work sit either side of the standard density of water.

The longitudinal sound speed ($c_L$) of the adipose material was measured ultrasonically at room temperature using a Panametrics pulser-receiver in the pulse-receive configuration and a 1.0 MHz Panametrics quartz transducer. This relatively low frequency was adopted to ensure maximum penetration of the ultrasonic waves in the highly attenuating adipose material. A value of $c_L = 1.51 \pm 0.10$ mm/$\mu$s was determined. This is in good agreement with longitudinal wave speeds obtained elsewhere for gelatin [95] and water [96] ($1.48 \pm 0.06$ mm/$\mu$s and 1.49 mm/$\mu$s, respectively). A shear wave speed for the

material was not discernible, most likely due to the materials low stiff-ness. An overview of ultrasonic diagnostics and the equipment used to determine wave speeds within materials is provided in Section 4.3.

# Chapter 6

# Development of a soft-capture system for the shock-recovery of porcine skeletal muscle tissue

A number of different types of soft-capture systems that have been used within the literature to recover materials following shock compression were discussed in Section 3.3. These techniques have most notably allowed for the soft-capture of metals, polymers, and (biological) cell suspensions. Upon reviewing the literature, it seems reasonable to suggest that the type of soft-capture systems used in conjunction with the plate-impact technique typically fall into one of two categories: (a) those in which the shocked material is ejected and recovered separately from the soft-capture vessel (e.g. [57]), or; (b) vessels that remain intact post-impact, but that do not deliver a simple square-topped pulse prior to release [60] (a requirement of the capsule developed in this work). As such, the development of a system that was capable of remaining both intact following plate-impact and delivering a simple

square-topped pulse to the sample prior to release was sought here.

The development of a soft-capture system allowing for the shock-recovery of porcine skeletal muscle in this body of work was facilitated by the non-linear explicit hydrocode: ANSYS® AUTODYN. Notably, a detailed overview of the ANSYS® AUTODYN package is provided in Section 4.5. A Lagrangian mesh size of 0.04 mm$^2$ (200 $\mu$m x 200 $\mu$m) was employed in all stages of the capsule development. This approach allowed a high degree of confidence in the output data to be established. In addition, this mesh size was deemed to provide balance between a high degree of accuracy in the numerical simulations and computational time, which increases with mesh density. This mesh size also provided close agreement with the typical combined thickness of a manganin foil pressure gauge and encapsulating layer (c.200 $\mu$m). Thus, it seems reasonable to suggest that the resolution of any experimentally measured shock interactions involving a particular variant of the soft-capture system should match with that of the model, e.g. simulated and experimental rise-times should be of the same order of magnitude.

In all stages of the development of a suitable capsule, the tissue sample was modelled using the shock EoS data established for skeletal muscle in this research study (i.e. $U_s = 1.72 + 1.88u_p$) - see Section 8. Further, a geometric strain erosion model set at 200 % was applied to all parts within the numerical simulations presented in this study. The loss of both mass and energy associated with this erosion model is one of the main limitations of simulations applying a Lagrangian mesh

to modelled parts. However, as is discussed in a detailed overview of the ANSYS® AUTODYN package provided in Section 4.5, the introduction of an erosion model is necessary to allow explicit simulations based upon a Lagrangian frame to run to completion.

Initially, the wave profile imparted to a sample when confined within an all-steel capsule was investigated. This design was based upon the the soft-capture system employed by Hazell et al. [60], which was used to investigate the effects of shock compression on bacteria. However, an additional PMMA/plexiglas ring, which encompassed/surrounded the tissue sample, was included in the design here. Being of closer acoustic impedance to the skeletal muscle than the surrounding steel vessel, the purpose of such an insert was to grade the change in impedance between the sample and the confining arrangement and thus minimize any radial release effects/loss of 1D conditions during shock loading. A schematic of the initial (all-steel) model is presented in Figure 6.1.

The steel material model in the numerical simulation of a 500 m/s copper flyer impacting the (all-steel) soft-capture vessel (see Figure 6.1) was of type AISI 304L (low carbon) and incorporated a Johnson-Cook strength model. Notably, this approach toward simulation was identical to that adopted by Hazell et al. [60] and was of the form:

$$\sigma = (A + B\epsilon_p^n)(1 + Cln\,\dot{\epsilon}_p)(1 - T_H^m) \qquad (6.1)$$

where $A$ is the yield strength at zero plastic strain, $B$ is the strain hardening constant, $n$ is the strain hardening exponent, $C$ is a strain-

|  | Notation | Steel (type AISI304L) | Copper |
|---|---|---|---|
| Yield strength (MPa) | $A$ | 90 | 110 |
| Work hardening constant (MPa) | $B$ | 292 | 1500 |
| Work hardening exponent | $n$ | 0.05 | 0.36 |
| Strain rate hardening coefficient | $C$ | 0.005 | 0.014 |
| Melting temperature ($^\circ K$) | $T_m$ | 1356 | 1696 |
| Reference temperature($^\circ K$) | $T_{room}$ | 300 | 300 |
| Thermal softening coefficient | $m$ | 1.09 | 1.0 |

Table 6.1: Johnson-Cook material strength data (adapted from [60] and incorporating data from [97] for the steel and [98] for the copper)

rate constant, $T_H$ is the homologous temperature $((T\text{-}T_{room})/(T_m\text{-}T_{room}))$, $m$ is the thermal softening exponent, and $T$ and $T_m$ are the temperature and melting temperature of the material, respectively. Finally, $\epsilon_p$ is the equivalent plastic strain and $\dot{\epsilon}_p$ is the dimensionless plastic strain-rate.

Both the copper and plexiglas (PMMA) models were selected from the AUTODYN® materials library. In likeness with the AISI 304L model, all copper components within the simulations presented in this work also incorporated a Johnson-Cook strength model. The Johnson-Cook strength data for both the copper and AISI 304L material models may be found in Table 6.1. In addition, hydrodynamic data for all other materials used in the numerical simulations presented in this section is provided in Table 6.2. The plexiglas (PMMA) was assigned hydrodynamic/strengthless properties.

In order to assess the nature of the loading profile experienced by
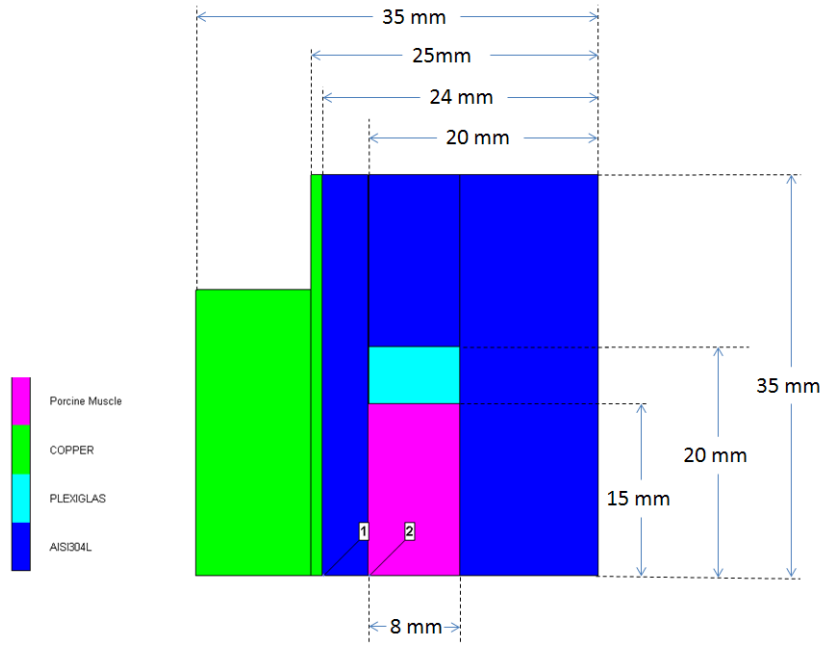
Figure 6.1: Initial capsule design - all steel construction

|  | Copper | Steel (304L) | Plexiglas (PMMA) | Muscle | Gelatin (20 wt.%) | Aluminium (Al − 6061) |
|---|---|---|---|---|---|---|
| Initial density (g/cm³) | 8.900 | 7.903 | 1.186 | 1.096 | 1.060 | 2.710 |
| Bulk sound speed (m/s) | 3958 | 4570 | 2598 | 1720 | 1570 | 5380 |
| Slope in $U_s - u_p$ Hugoniot | 1.50 | 1.49 | 1.52 | 1.88 | 1.77 | 1.34 |
| Gruneisen coefficient | 2.00 | 1.93 | 0.97 | − | − | 2.1 |

Table 6.2: Hydrodynamic EoS model data for the copper, stainless steel, skeletal muscle, 20 wt.% gelatin, and aluminium. (Data for the copper, stainless steel, and aluminium was taken from the AUTODYN® material library and data for the gelatin was taken from [99]. The data for the muscle was established in this study (see Section 8))

the sample in the all-steel capsule, modelled gauges (nodal monitoring positions) were inserted into the simulation at two separate locations. The first gauge was positioned at the front surface of the capsule lid, while a second was placed at the front surface of the tissue sample.

The stress-time history resulting from a simulated 500 m/s copper impact upon the all steel capsule design is presented in Figure 6.2. There are a number of points to note from the simulated results. Firstly, a significantly larger stress is observed in the steel capsule lid than the tissue sample. This is due to the dissimilar shock impedances of the two materials, i.e. their initial densities, and their shock equations of state ($P = \rho_0 U_s u_p$). The impact event is shown to induce a constant Hugoniot stress of c.1.3 GPa within the tissue sample. Further, this steady shocked state is seen to last for approximately 4.5 $\mu$s. Upon reaching the rear surface of the sample and a material of higher impedance than skeletal muscle, i.e. the steel backing of the capture vessel, reflection of the shock has occurred. This is evident from the reflected signal detected by the gauge located at the front surface of the sample. Is seems likely that this reflected pulse, which is detected at t = $\sim$ 5.7 $\mu$s and shown to result in a pressure-stress state in excess of 20 GPa, would have have had a significantly greater effect upon the tissue sample than the initial shock pulse of c.1.3 GPa. However, subsequent analysis of any structural alteration imparted to the tissue from an impact of this nature would have reflected the combined effects of both portions of the loading history. A shock reflection of the magnitude displayed in Figure 6.2 is entirely unacceptable in a capture
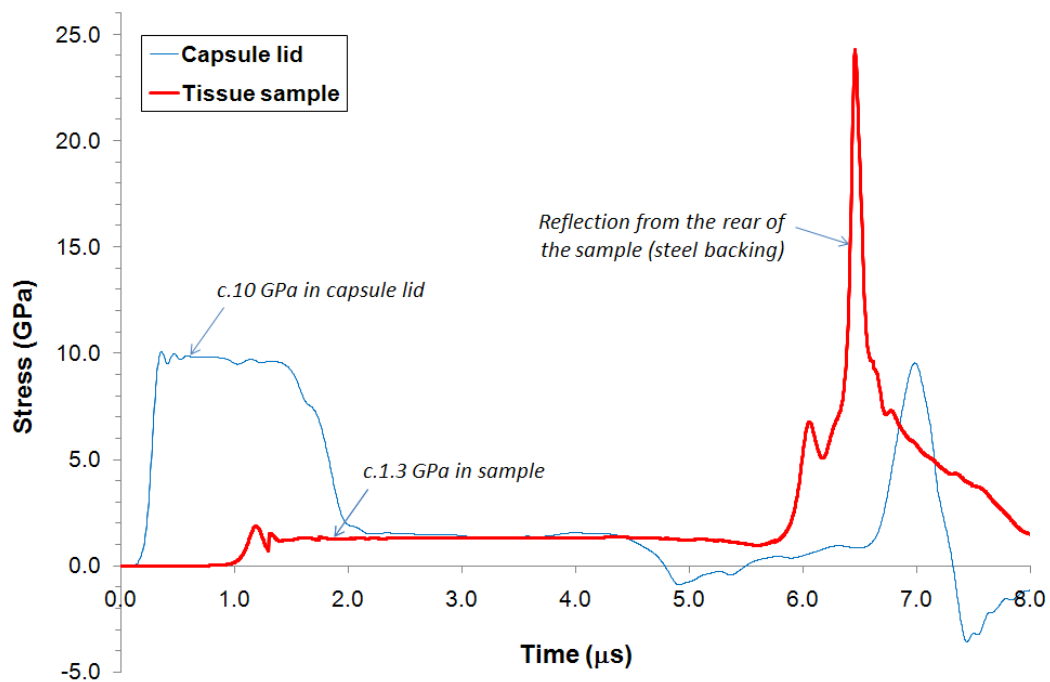
Figure 6.2: Initial capsule design - all steel construction. (Simulation of a 500 m/s copper flyer impact)

system aimed at imparting a simple square-topped pule to the sample prior to release. Consequently, the development of an improved design was sought.

The next logical step in either preventing or minimizing any shock reflection within the capsule appeared to involve backing the sample tissue with a material of lower impedance than steel, or similar shock impedance to the skeletal muscle. As such, it was decided that a 5 mm thick plexiglas (PMMA) disk should be inserted behind the sample in the next iteration of the design. In terms of capsule manufacture, this step would have involved the removal of material (steel) from the capsule void (see Figure 6.3). The void present in the initial (all-steel) design simply lacked the ability to accommodate the additional
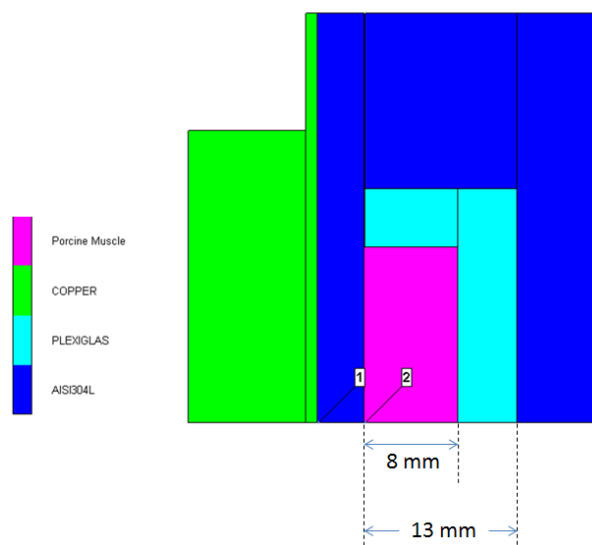
Figure 6.3: Soft-capture capsule with PMMA insert

PMMA disk. As per the initial design, simulation of a 500 m/s copper flyer impact upon the capture system was performed. The results from this simulation are presented in Figure 6.4 and show a clear reduction of the reflected signal. However, a peak reflected pressure in excess of 5 GPa was still detected at the front surface gauge (nodal monitoring position). Notably, a signal corresponding to the generation of a reflected wave at the tissue-plexiglas (PMMA) boundary was not detected by the simulation. As such, the reflected signal presented in Figure 6.4 is the sole product of the shock reflection originating from the PMMA-steel boundary, i.e. the rear surface of the capsule void.

In order to achieve the desired loading profile of a simple square-topped pulse prior to release within the sample, it was decided that two specific design features needed to be incorporated into the design of the soft-capture system. Firstly, and in light of the improved re-
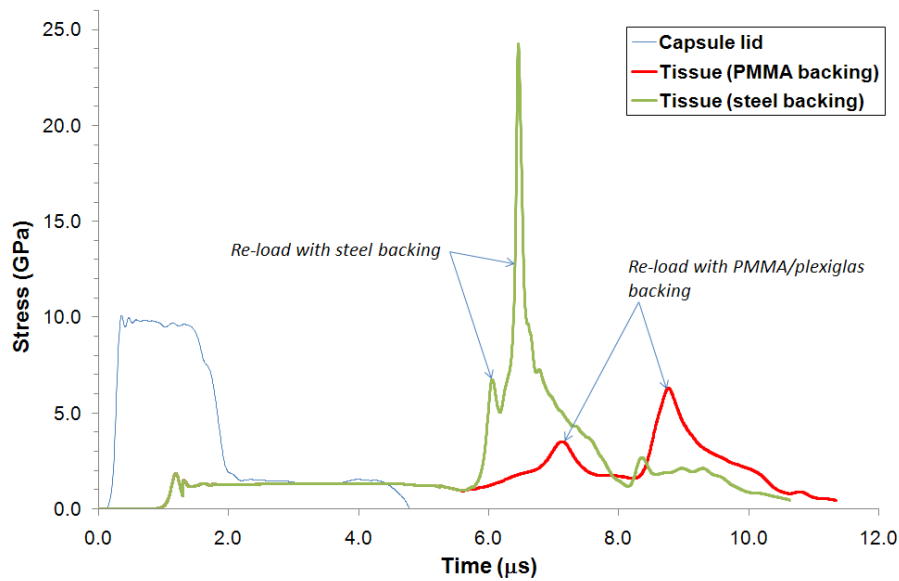
Figure 6.4: Simulation of a 500 m/s copper flyer impact upon the soft-capture capsule with PMMA insert

sult observed in Figure 6.4, it was reasoned that a backing material of equal or lower acoustic impedance to muscle tissue was required. Secondly, in order to trap the momentum of the shock, it appeared that the overall thickness of the backing material would have to be significantly increased. Propagation of shock waves requires a medium. Consequently, in a given medium (e.g. air/water), the greater the displacement of the shock from its point of origin, the lesser the energy associated with the propagating wave front. This energy loss may be attributed to the work done on the medium by the shock (e.g. the resultant change in pressure and temperature). As such, it seemed logical that by extending the thickness of the backing material towards infinity, the greater the overall reduction of energy associated with the incident shock that would result. It also seemed logical that

the adoption of a backing material of equal or lower shock impedance than the sample material would dictate that the component of the shock reflected at the sample-backing interface would either be not generated (equal impedance), or minimal (lower impedance). Hence, the majority of the stress imparted to the sample by the incident shock would be transferred into the backing material and the reflected component of the shock would likely result in a less significant change in stress within the sample than when a backing material of slightly higher impedance (i.e. plexiglas/PMMA) was adopted.

In plate-impact experiments, the thickness of the flyer may be used to control the duration of the shock pulse, i.e. a thicker flyer will provide a longer duration shock pulse than a thinner flyer. Such behaviour is due to the fact that it takes longer for a shock generated upon impact in a thick flyer to: (a) reach the rear of the flyer and then become tensile on relection from its rear (free) surface, and; (b) for this tensile release wave to ultimately catch up to the incident shock within a sample. The opposite is true for a thinner flyer during identical impact conditions. Thus, by: (i) extending the thickness of the backing material towards infinity, and; (ii) selecting a flyer of appropriate thickness to the impact velocity, it seemed reasonable that it might be possible to specify the point of release for the transferred component of the incident shock to occur within the (lower impedance) backing material. As such, no reflected pulse would be generated from the rear of the capsule. During typical plate-impact experiments, it is common to select a flyer of appropriate thickness to the impact velocity. This ensures

one-dimensional release of the sample before peripheral release waves may have an effect upon the planarity of the shock. When seeking to achieve one-dimensional release of the sample, the maximum thickness of the flyer is dictated by: (i) the equation-of-state of both the flyer/cover and the sample materials; (ii) the impact (and thus shock and release) velocity, and; (iii) the diameter of the flyer and sample. Thus, if a flyer of 'excessive' thickness is adopted, radial release waves will begin to have an effect on the sample. Again, it should be noted that this conflicts with the intention of any plate-impact experiment. While seeking to achieve a shock pulse of a relatively long duration in the soft-capture experiments performed in this work, the uniform release of tissue sample was also desired.

The final design specification of the soft-capture system, which allowed for the successful shock-recovery and post-shock analysis of skeletal muscle tissue, is presented in Figure 6.5. In addition, a schematic of the system, in which overall dimensions are given, is presented in Figure 6.6. Unlike the previous capsule designs covered in this section, the final capsule design was not constructed out of type AISI 304L steel, but Al-6061 (aluminium). This choice of material helped to reduce the overall mass of the system and, for a given impact velocity, reduce the level of stress that would otherwise have been imparted to the sample by a system incorporating a steel lid (i.e. due to its lower acoustic impedance). A linear equation-of-state (EoS) model employing a von-Mises strength criterion was selected from the AUTODYN material library for the aluminium components within

the simulation (i.e. the capsule lid and walls). In addition, plastic strain failure was set to occur at 30 % for the alloy. Values of 26.9 and 29.0 GPa were adopted for the shear modulus and yield stress for the aluminium, respectively. In addition, 20 wt.% ballistic gelatin was adopted as both a backing material and as a surrounding 'jacket' (see Figure 6.5), thus replacing the plexiglas (PMMA) inserts used in the previous configuration. This material afforded a significantly improved match in impedance between the tissue sample and the backing section of the capsule design. Again, the extension of the backing section allowed for suitable release of the shock following complete migration through the tissue sample. Notably, the 5 mm lid of the soft-capture system was machined to a 'press-fit' tolerance with respect to the vessel's main body and was further secured using three countersunk screws. Numerical simulation of the soft-capture experiments conducted in this work is discussed later in detail (see Section 8.3).
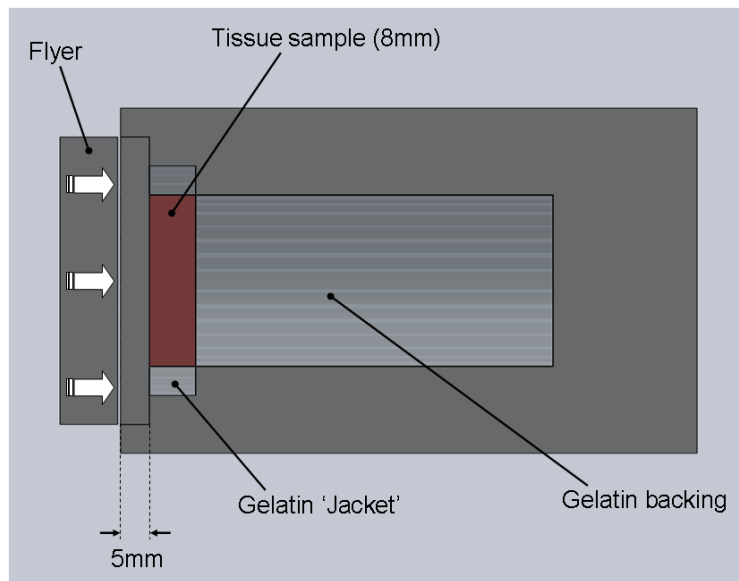
Figure 6.5: Soft-capture vessel
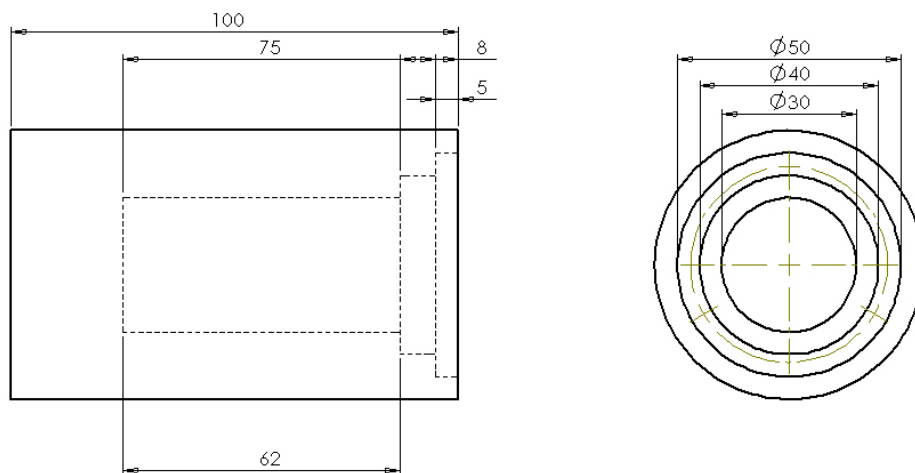


Figure 6.6: Capture vessel design specifications (dimensions are in millimeters)

# Chapter 7

# Experimental Setup

## 7.1  Plate-Impact Setup

The setup adopted for plate-impact experiments is shown in Figure 7.1. The velocity of the flyer was determined by the sequential shorting of an array of graphite pins, each of which were held in pairs in a velocity pin block (see Figure 7.1). Knowledge of the spatial separation of the graphite pins (12 mm) allowed calculation of the velocity of the flyer, i.e. *speed = distance/time*. In addition, a further set of conductive pins was also employed to trigger a second oscilloscope, to which the embedded manganin foil pressure gauges were connected (see trigger pins in Figure 7.1).

Components forming an important part of plate-impact setup but which are not shown in Figure 7.1 include the barrel extension, the barrel containment vessel, and the momentum capture arrangement. The function of the barrel extension in an experiment was to: (a) act as a support for the velocity pin block; (b) act as a guide for the sabot once it had left the barrel; (c) provide a stable platform upon
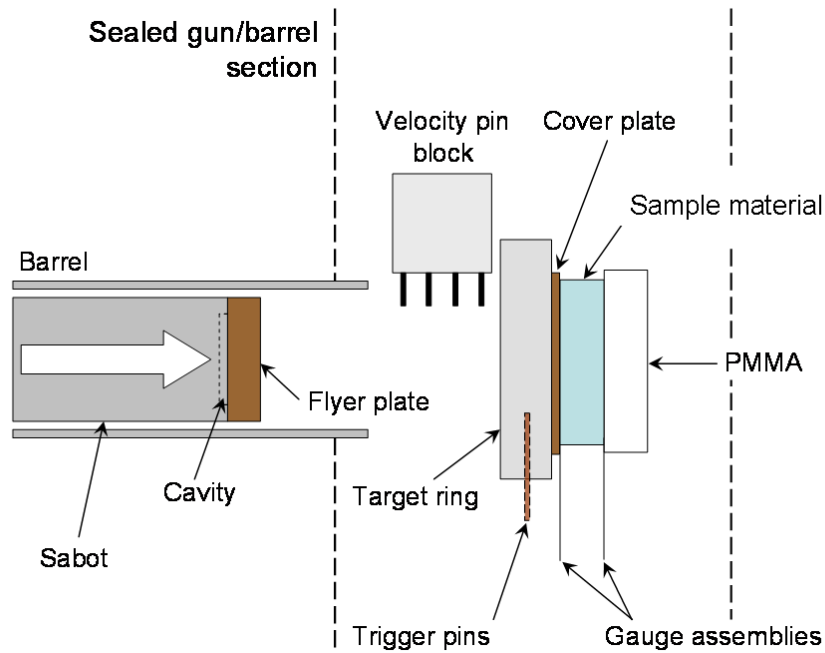
Figure 7.1: Experimental setup/target arrangement

which the target ring and sample could be mounted, and; (d) act as a sacrificial extension of the barrel in case of damage caused by the impacted target. The barrel containment vessel, which was constructed from large polymeric tubing and an aluminium end-plate, was used to seal the front section of the gun, i.e. the barrel section. Such action allowed for a much stronger vacuum to be created than within the rearward expansion chamber and capture tank, which occupied a much larger volume. This essentially acted to reduce gas presence ahead of the projectile and minimize both retardation of the projectile and the chances of pre-impact disturbance on the target. Finally, a perspex window was machined into the aluminium end-plate to allow the flyer/sabot to exit the containment vessel and continue along its trajectory into the capture tank and momentum capture section.

149

## 7.2 Dual Type LM-SS-125CH-048 (Longitudinal) Gauge Experiments

Use of two type LM-SS-125CH-048 longitudinal manganin stress gauges in a single shock experiment, i.e. one located at each of the front and rear surfaces of the sample, respectively, yields a significant amount of data. Firstly, provided that the overall thickness of the sample is accurately known, temporal knowledge of shock arrival at each gauge allows for simple but accurate calculation of shock velocity (via $speed = distance/time$). This approach differs from free-surface techniques such as VISAR and heterodyne velocimetry which allow for only the free-surface/particle velocity at the rear surface of the sample to be measured, i.e. they do not directly measure the velocity of the shock. Particle velocity is derived using the impedance matching technique (see Section 3.2) in dual gauge experiments. Thus, each experiment yields a shock velocity-particle velocity ($U_s$-u$_p$) datapoint on the principal Hugoniot. The additional benefit of using manganin foil gauges is that they allow for direct measurement of the levels of uniaxial stress imparted to the sample by the shock. This ultimately allows for comparison between the predicted hydrodynamic behaviour of a material ($P = \rho_0 U_s u_p$) and its measured response in both the pressure-particle velocity ($P$-u$_p$) and pressure-volume ($P$-V) Hugoniots.

The components comprising a longitudinal shock response target were: (i) a cover-plate of identical material (and therefore acoustic impedance) as the flyer; (ii) the front surface gauge package; (iii) the

sample material; (iv) a rear surface gauge package, and finally; (v) a backing plate (typically manufactured out of polymethyl-methacrylate (PMMA), due to its well-defined Hugoniot [16], [100] and known response to one-dimensional shock [101]).

Gauge packages each encompassed a piezoresistive manganin foil pressure gauge, two brass shim legs (one attached to each of the two solder tabs on the gauge), two sheets of equally thick (25 $\mu$m) Mylar® insulation placed either side of the gauge, and an epoxy layer, which bound the components together. An example of a gauge package employing two sheets of 50 $\mu$m Mylar® insulation is shown in Figure 7.2. The purpose of the brass shim legs was to allow for the change in applied voltage and current to be monitored during shock loading via connection to a display/storage device, e.g. an oscilloscope. Gauge legs were attached using a small amount of indium solder, whose low melting temperature (180 °C for type 1E, 52IN/48SN solder [102]) prevented damage to the gauge's backing material or the gauge wire itself. Insulation of gauges is not required when the they are embedded within polymeric targets, due to their non-conductive nature. In this work, however, all experimental gauges were insulated due to the dielectric properties of many biological materials [103], [104], [105] and the overriding desire to prevent any effect that this may otherwise have had on gauge response.

In order to ensure one-dimensional loading, the mount faces of all target components were machined flat and parallel to within a tolerance of 10 $\mu$m. When combined with the design specifications of the 50
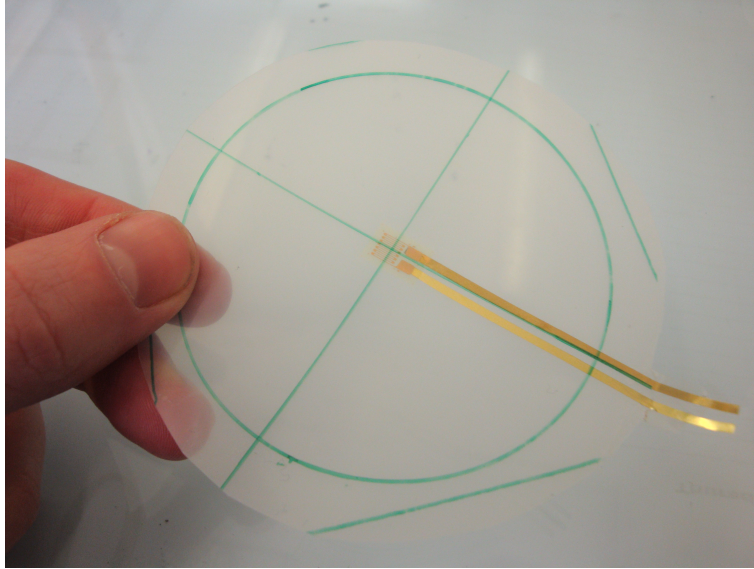
Figure 7.2: Type LM-SS-125CH-048 (longitudinal) gauge package

mm single-stage gas gun employed during plate-impact experiments, this ensured that all strain acted along the impact axis. Aluminium rings of 60 mm internal diameter were used to confine target materials in a controlled manner. A schematic of the aluminium sample rings used in experiments is shown in Figure 7.3. Recesses were machined into the flat faces of the rings to prevent the legs of the managanin gauges from interfering with either the flatness or parallelism of the targets. Major components of the target assembly (e.g. the cover-plate, sample ring, and PMMA backing block) were bonded together in a purpose-built jig using LOCTITE® fast-acting epoxy resin. Gauge packages, however, were constructed using slower curing epoxy resins - either Pacer Technology's Z-Poxy® or LOCTITE® 0151® Hysol® two-part epoxy resin depending on availability at the time of target manufacture. The combination of a slower curing epoxy resin and float glass, which was used in the purpose-built jig during gauge pack-
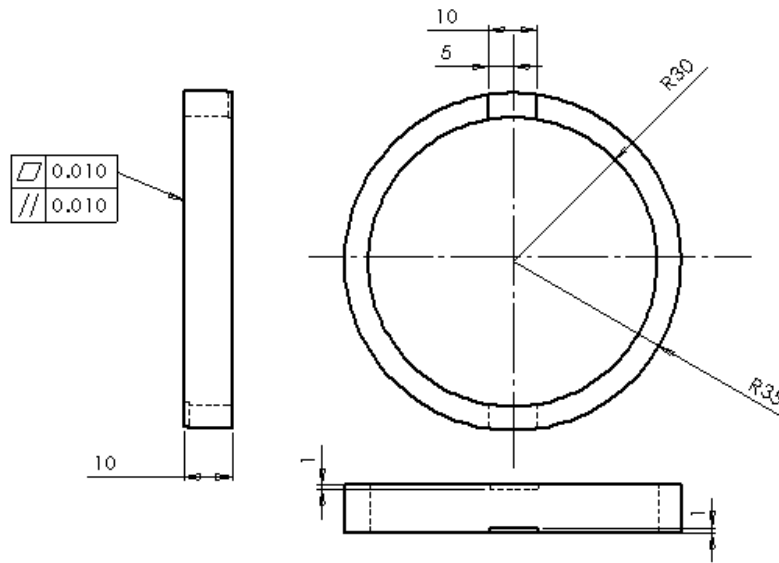
Figure 7.3: Aluminium sample ring. (Note: (a) dimensions are in mm; (b) general tolerance of 0.25 mm applies; (c) overall thickness (10 mm) may vary)

age manufacture, allowed for maximum migration of excess adhesive from the glue layer. Consequently, a suitably thin encapsulating layer ($\leq 200$ $\mu$m) was achievable. A thinner glue layer was experimentally beneficial as it minimized gauge rise-time, hence increasing accuracy during the determination of shock velocity between the two gauge loci.

### 7.2.1   Porcine Adipose Material

Target manufacture for the investigation of shock wave propagation within the adipose tissue involved three main stages. These were: (i) construction of a hollow target assembly; (ii) slowly heating the material to a temperature at which it was completely liquid (50-60 °C), and; (iii) syringing the resultant liquid material into the hollow target assembly via a 7 mm hole machined into the side wall of the sample ring.

Figures 7.4 and 7.5 show a pre-cast/hollow and a fully-cast target assembly, respectively. The figures also highlight the use of an additional, larger ring that the target assemblies were bonded to using Plastic Padding® 'chemical metal'. This particular bonding agent comprised both a styrene monomer filler and benzoyl peroxide hardener.

The larger (target) rings shown in the Figures 7.4 and 7.5 form part of the overall setup for a plate-impact experiment, which is discussed in greater detail in Section 7.1. By casting liquid lard into hollow target arrangements, an intimate contact layer between both the material and the front and rear gauge surfaces was ensured. While the temperatures employed in this preparatory process were above the typical fat-to-lipid (solid/liquid) transition point (35-40 °C), they remained significantly below those used in commercial rendering processes (> 100 °C in steam processing for 1-5 hours). Being a rendered product, it seems reasonable to suggest that the casting methods used in this work will have caused minimal to no
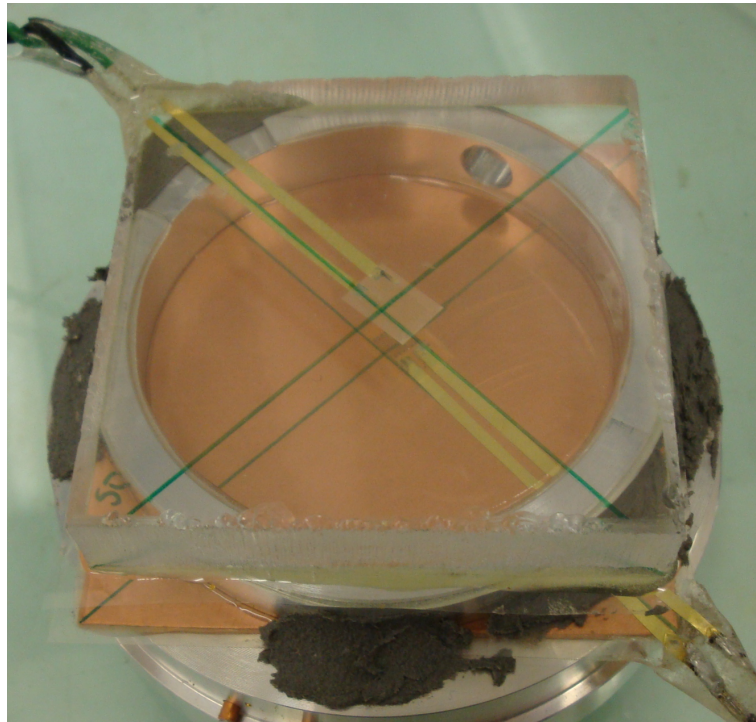
Figure 7.4: Pre-cast/hollow adipose target assembly
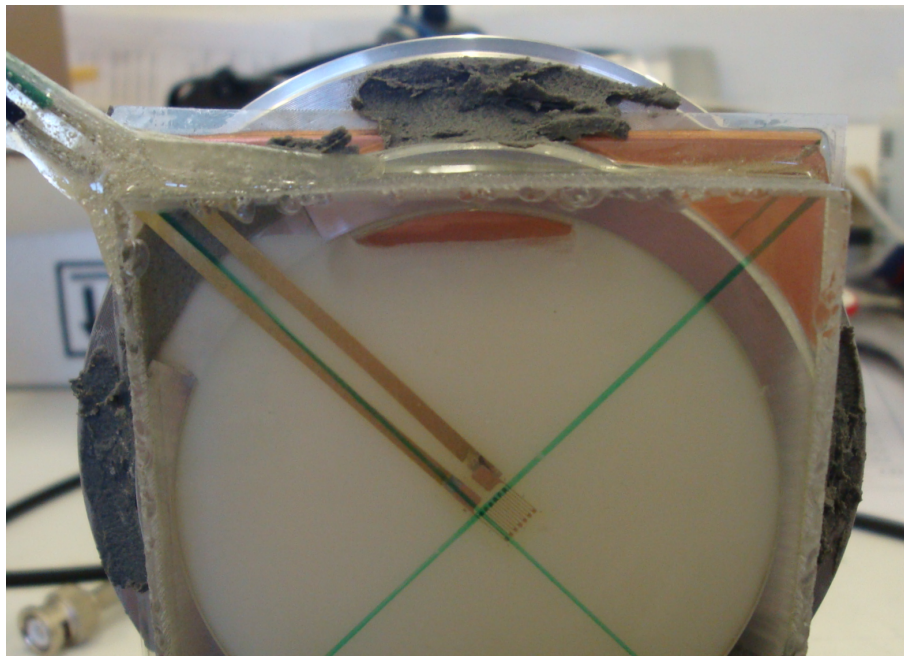


Figure 7.5: Fully-cast adipose target assembly

significant alteration to the microstructure of the adipose material. In all experiments the target rings employed were 10 mm ($\pm$ 20 $\mu$m) thick and the Mylar® sheet insulation was 25 $\mu$m thick.

### 7.2.2   Porcine Skeletal Muscle Tissue

Sheets of tissue were initially cut from the bulk muscles using an Ital Stresa 250S meat slicer. Following this, sample discs were excised from the sheets using sharp trephine blades. These samples were then confined within one of two assemblies: aluminium target rings of 60 mm internal diameter or PMMA sample holders of 40 mm internal diameter. Further, a range of thicknesses (6, 10, or 12 mm $\pm$ 0.25 mm) were used in the plate-impact experiments involving muscle tissues. In all cases, the tissue samples were then further confined between a 1 mm copper cover plate and a PMMA backing block. As with the adipose target components, the mount-faces of these confining assemblies were machined flat and parallel to a tolerance of 10 $\mu$m.

Despite yielding differing shock speeds for a given impact velocity, the type of material used to confine samples in this work had no effect upon the measured response. The reasoning behind this is twofold. Firstly, a large sample diameter dictated that all gauges were physically removed from the radial extremities of the target arrangement where peripheral release waves are naturally generated. Secondly, by varying both the type (e.g. copper, aluminium) and thickness of the flyer (5-10 mm), the shock pulse duration in each experiment was

controlled. Thus, following the initial stage of shock compression, a uniform release wave would propagate through the sample long before any effects of radial release/loss of one dimensionality were permitted.

Tissue samples were sectioned both 10 mm less than the internal diameter and 3 mm greater than the overall thickness of the assembly in which they were to be confined, i.e. 6, 10, or 12 mm aluminium or PMMA sample holders. Such action mean that, upon placement between the copper cover plate and the PMMA backing block, the tissue expanded to fill the void of the confining assembly. This resulted in intimate contact between the tissue and the gauge-mounted surfaces - a requirement for the stable transmission of the shock through the sample. The overall volumes into which the tissue samples were confined were consistently (slightly) larger than that of the unconfined tissue sample. As such, it was reasoned that 'confinement' of samples by the described methodology should not have stressed the material in any significant manner. While it may still be argued that the shock response of this work reflects that of the tested tissues in a pre-stressed state (i.e. due to confinement), the magnitudes of stress imparted to the samples by the shock wave determines that any pre-compressive effects are likely negligible in the corresponding shock data.

**Homogenized Tissue Variant**

For the manufacture of the homogenized variant targets, two target halves were initially constructed: one comprising both a PMMA backing block and rear gauge package; the other comprising a cover-plate, front surface gauge package, and either an aluminium target ring or PMMA sample holder. As with all other target preparation techniques, major parts of the assembly were bonded together using LOCTITE® fast-acting epoxy resin while gauge packages were assembled using either Pacer Technology's Z-Poxy® or LOCTITE® 0151® Hysol® two-part epoxy resin. Sample material was tightly packed into the hollow target half, i.e. the half comprising either the aluminium sample ring or PMMA sample holder. By closely packing the material (essentially a paste), the possibility for the formation of air gaps within the bulk of the sample mass was minimized. Finally, the two target halves were assembled and bonded together using LOCTITE® fast-acting epoxy resin.
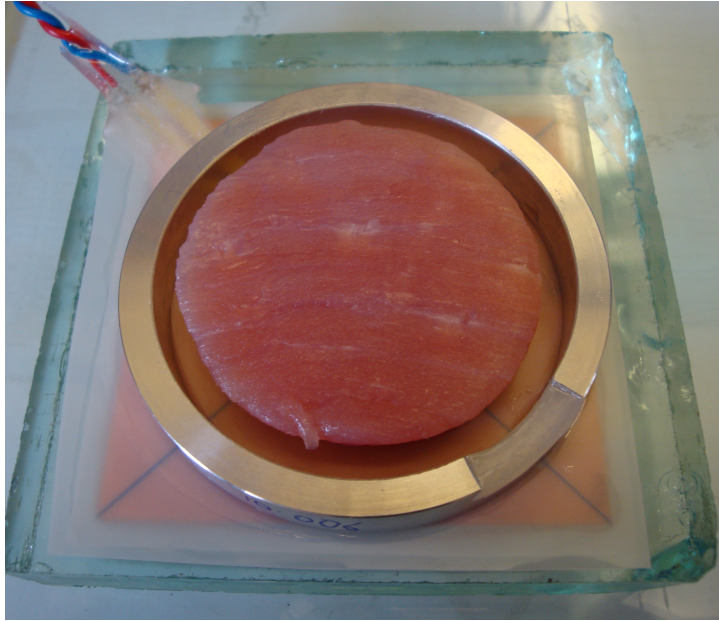
Figure 7.6: 'Non-confined' skeletal muscle tissue target
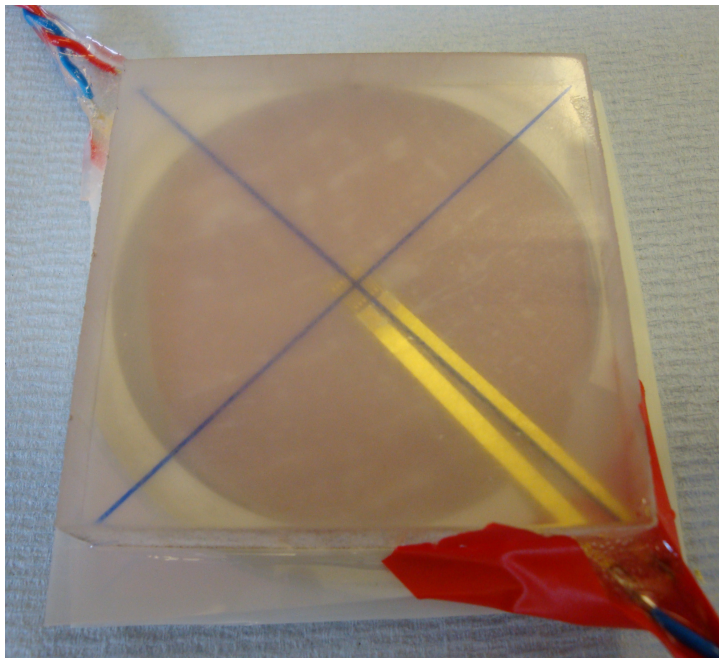


Figure 7.7: 'Confined' skeletal muscle tissue target

## 7.3 Type J2M-SS-580SF-025 (Lateral) Gauge Targets - Adipose Material Testing

The techniques employed to measure lateral stress in plate-impact experiments are widely covered in the literature [106, 107, 108, 109]. However, the types of materials that are typically investigated by such methods are metals and polymers, whose machinability allows for the placement of lateral stress gauges directly between prepared target-material halves. Aluminium rings of 60 mm internal diameter, of either 6 or 10 mm $\pm$ 20 $\mu$m thickness, and with opposing faces machined flat and parallel to a tolerance of 10 $\mu$m, were employed for target-material confinement in this study. Adhered to the front of the sample ring was a 1 mm thick copper cover-plate, whilst the rear of the target ring allowed for the insertion of the gauge-support assembly (see Figure 7.8). The lateral response targets were initially assembled into a hollow-casing form prior to being filled with liquid adipose material through one of two 4 mm holes machined into the side-wall of the target-rings; the second allowing for the release of air from the target void. The lateral gauges employed were of type J2M-SS-580SF-025 Vishay Micro-Measurements® & SR-4® Manganin Pressure Sensors, calibrated according to the methodology adopted by Millett et al. [110] (a technique based upon the previous work of Rosenberg and Partom [63], Rosenburg and Brar [64], and Millett et al. [65]). Additional information regarding the calibration of type J2M-SS-580SF-025 lateral stress gauges can be found in Section 4.2.2.

Lateral gauges were initially encapsulated between two 50 $\mu$m Mylar® sheets prior to secondary confinement between two PMMA halves with flat mount faces. As shown in Figures 7.8 and 7.9, this arrangement was then employed as the rear-surface of the hollow casing assembly, with the encased gauge protruding into the target cavity. Mylar® encapsulation enhanced the stiffness of the gauge package. This allowed for accurate alignment of the gauge element in relation to the impact axis at distances of 4 and 6 mm from the copper/adipose material impact boundary. In addition to experiments in which a Mylar® encapsulating layer was used to surround the gauge element, experiments were also conducted in which the gauge element protruded further ahead of any encapsulation. In such configurations, only as-cast lard surrounded the gauge element. Distances of 4 and 6 mm of the gauge element from the front edge of the target material were, however, maintained. These two distinct types of lateral gauge experiments were undertaken in order to ascertain any effect of localized encapsulation on gauge response. All target components were bonded together with Pacer Technology Z-Poxy®, a two-part epoxy resin comprising an epoxy resin and mercaptan hardener.
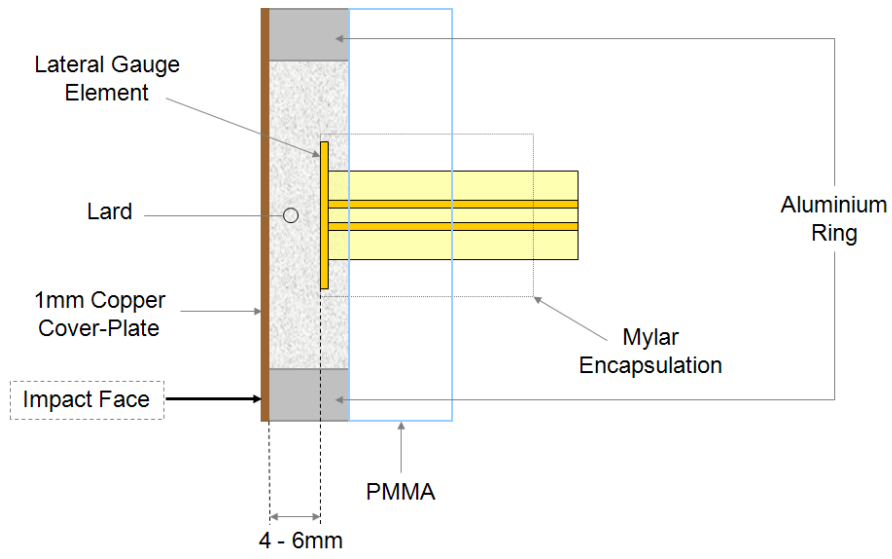
Figure 7.8: Side view of lateral gauge target assembly
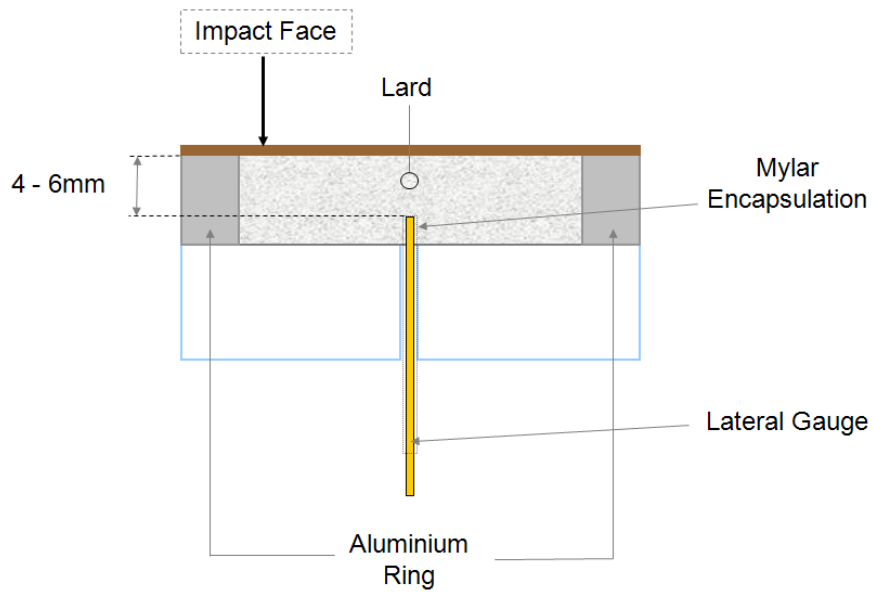


Figure 7.9: Alternate side view of lateral gauge target assembly

# Chapter 8

# Results and Discussion

## 8.1 Adipose Material

A total of ten plate-impact experiments were conducted during investigation of the longitudinal shock response of the adipose material. The shock response data from these experiments, which corresponds to an impact velocity range of 39-882 m/s, is shown in Table 8.1.

A typical longitudinal stress-time history resulting from a twin-gauge adipose target is presented in Figure 8.1. These traces exhibit a number of key features. Firstly, a small undershoot at shock arrival (a) is observed at the front surface gauge. Such undershoots have been seen elsewhere [111] and have been attributed to a capacitance effect as the conducting cover plate moves towards the insulated gauge. Both gauge traces within Figure 8.1 exhibit: (a) rapid rise times of 100-123 ns (indicative of good target alignment), and; (b) a constant (Hugoniot) stress behind the shock. It is also worth noting that there is a clear temporal separation of shock arrival times ($\Delta t$). This temporal resolution, when combined with knowledge of sample thickness,

| Experiment | Flyer thickness (mm) | Impact velocity (m/s) | $u_p$ (mm/µs) | $U_s$ (mm/µs) | $\sigma_x$ (GPa) |
|:---:|:---:|:---:|:---:|:---:|:---:|
| 1 | 10 | 39 | 0.04 | 1.44 | ... |
| 2 | 5 | 76 | 0.007 | 1.75 | 0.09 |
| 3 | 5 | 79 | 0.08 | 1.82 | 0.12 |
| 4 | 10 | 183 | 0.17 | 2.06 | 0.31 |
| 5 | 10 | 310 | 0.29 | 2.29 | 0.67 |
| 6 | 10 | 411 | 0.39 | 2.39 | 0.95 |
| 7 | 5 | 489 | 0.46 | 2.77 | 1.26 |
| 8 | 10 | 596 | 0.55 | 2.87 | 1.79 |
| 9 | 10 | 758 | 0.70 | 3.26 | 2.63 |
| 10 | 5 | 882 | 0.80 | 3.67 | 3.08 |

Table 8.1: Longitudinal shock data - adipose material

allowed calculation of the shock velocity for a given experiment.

In Figure 8.1, the front gauge trace indicates the stress-time behaviour of the adipose material whilst the rear gauge response shows the stress observed in the PMMA backing. Given knowledge of the density and measured shock velocity in the target, it is possible to convert the rear gauge response to that in the target material using Equation 8.1, where; $Z_{Adipose}$ is the shock impedance of the adipose material, $Z_{PMMA}$ is the shock impedance of the PMMA, and in general, $Z = \rho_0 U_s$.

$$\sigma_{Adipose} = \frac{1}{2} \frac{(Z_{Adipose} + Z_{PMMA})}{Z_{PMMA}} \sigma_{PMMA} \qquad (8.1)$$
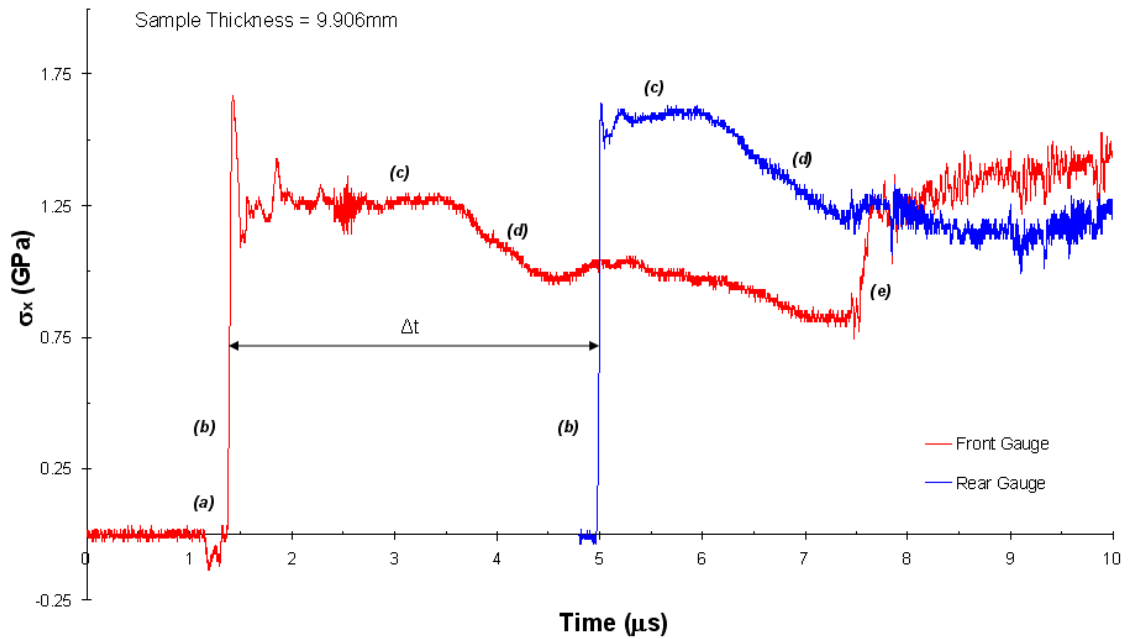
Figure 8.1: Typical longitudinal stress-time history for the adipose material (example corresponds to a 5 mm Cu flyer impacting an adipose target at 489 m/s)

Notably, the rear gauge response in Figure 8.1 has a higher Hugoniot stress than the front gauge trace. From Equation 8.1, this implies that the adipose material has a lower shock impedance than the PMMA. Another key feature of the traces presented in Figure 8.1 is the initially elastic release behaviour (d). This is the result of release waves from the rear of the flyer catching up with the shock in the material. Finally, reloading of the adipose material occurs at (e).

In Figure 8.2 the $U_s$-$u_p$ Hugoniot for the adipose sample material, which is constructed from the information presented in Table 8.1, is compared with the Hugoniot of 20 wt.% ballistic gelatin [95] and water [112]. Shock velocity errors included on the Hugoniot were cal-

culated from the possible range of shock arrival times ($\Delta t$ in Figure 8.1) and are expressed as maximum and minimum values from the median shock arrival time. As discussed in Section 3.2, particle velocity was solved using a quadratic fit (see Equation 3.5). Notably, two of the coefficients required to solve this quadratic are dependent upon the value for shock velocity, which was determined experimentally. In order to calculate both the maximum and minimum particle velocities possible in a given experiment, two new sets of coefficients were calculated for the sample material: one taking account of the maximum possible shock velocity and the other the minimum possible shock velocity. Consequently, and in likeness with the shock velocity errors presented in the dataset, the particle velocity errors were expressed as maximum and minimum values from the median particle velocity value. However, particle velocity errors calculated by this method were both negligible and did not extend beyond the limits of any of the datapoints presented on the $U_s$-$u_p$ Hugoniot for the adipose material.

The measured longitudinal sound speed of the adipose material ($c_L$ = 1.51 $\pm$ 0.10 mm/$\mu$s) holds good agreement with the corresponding values of $c_L$ and Hugoniot intercept for ballistic gelatin (1.48 $\pm$ 0.06 mm/$\mu$s and 1.57 mm/$\mu$s, respectively [95]). The Hugoniot relationships for water and ballistic gelatin (both established elsewhere [95], [112]) hold close agreement with one another in the $U_s$-$u_p$ plane at particle velocities less than 1 mm/$\mu$s (see Figure 8.2). Conversely, the Hugoniot established for the rendered porcine fat does not possess such close agreement over the range of measured impact conditions.
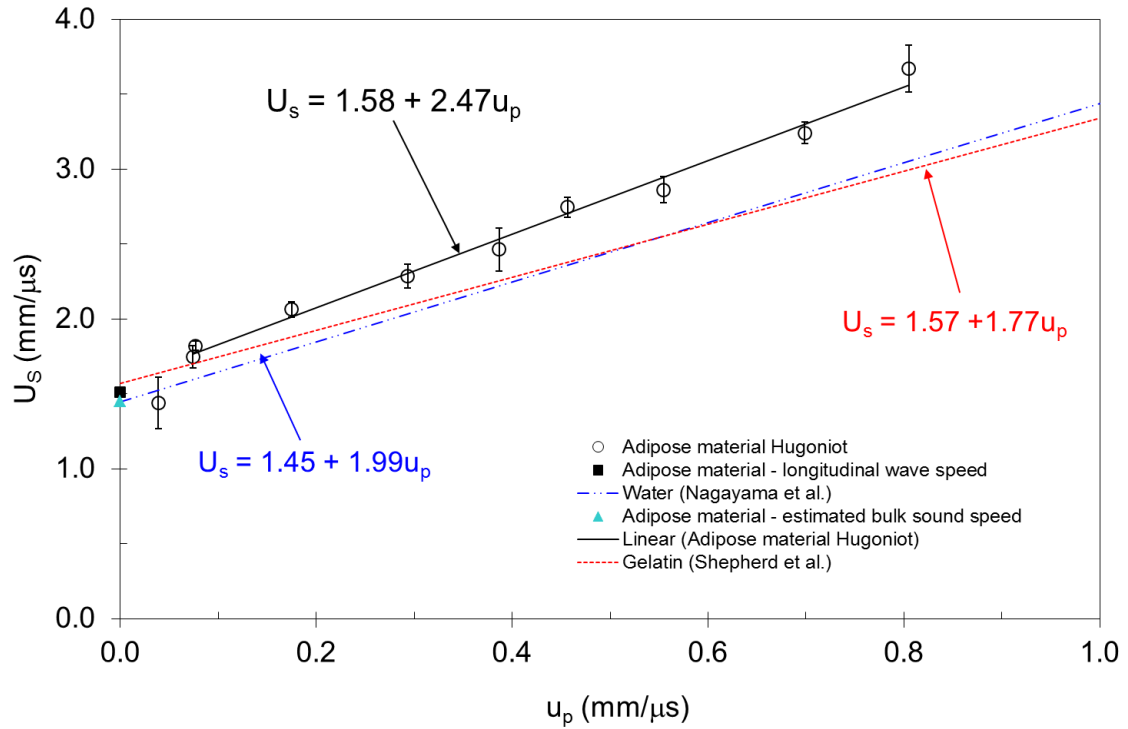
Figure 8.2: Principal ($U_s$-$u_p$) Hugoniot of the adipose material

While the material is seen to occupy similar $U_s$-$u_p$ space at lower particle velocities, its response differs significantly at particle velocities $\geq$ 0.5 mm/$\mu$s.

Information within the literature suggests that the value of Poissons ratio for fatty/adipose materials is approximately 0.5. Notably, materials posessing a Poisson's ration of 0.5 are incompressible. Delalleau et al. [113] determined the value of Poissons ratio for subcutaneous fat as 0.48 from indentation studies, whilst a value of 0.49 was adopted during research into deep tissue injury [114]. Further, a review presented by Palomar et al. [115] highlighted the wider acceptance that a value for Poissons ratio for fatty tissues is close to 0.5. Assumption of a value of 0.47 for the adipose material investigated in this work suggests a shear wave velocity of 0.35 mm/$\mu$s (see Equations 8.2 and

167

8.3). This would equate to a bulk sound speed for the material of 1.45 mm/$\mu$s, which is in good agreement with values of 1.42 and 1.44 mm/$\mu$s established ultrasonically elsewhere [116], [117]. Increasing the value of Poissons ratio for the adipose material to 0.49 (a value used elsewhere [114]) resulted in a calculated value of $\sim 1.49$ mm/$\mu$s for $C_0$. This value is significantly higher than the expected bulk sound speed for fat/fatty tissues taken from the literature (1.42 mm/$\mu$s [116] and 1.44 mm/$\mu$s [117]). Consequently, a value of $v = 0.49$ was considered less suitable than the chosen value of 0.47.

$$\alpha = \frac{C_s^2}{C_L^2} \tag{8.2}$$

$$\nu = \frac{2\alpha - 1}{2\alpha - 2} \tag{8.3}$$

A value of $C_0 = \sim 1.45$ mm/$\mu$s for fat (obtained when $v = 0.47$) suggests that slight curvature of the otherwise linear Hugoniot relationship for the adipose material exists at low particle velocities. Given the nature of the adipose material and the limited suitability of manganin pressure gauges in measuring shock at such low stress levels, detailed interrogation of the suggested curvature at lower particle velocities was not further practicable. Nevertheless, curvature at low particle velocity for otherwise linear Hugoniots has been witnessed elsewhere for polymers [16], [31], which possess similar structure to that of triaglyceride/triglycerol fats.

The linear relationships established for Polyethylene, Polypropylene, and Polystyrene provide linear Hugoniot intercept values which are significantly greater than their measured bulk sound speeds ($C_0$) [15]. Combination of (a) the (adipose) experimental results; (b) the trend for polymers to exhibit lower sounds speeds than the values provided by the linear-fit incercept in the $U_s$-$u_p$ Hugoniot, and; (c) a calculated value of $C_0 = \sim 1.45$ mm/$\mu$s for fat (assuming $v = 0.47$) suggests that the bulk sound speed of the rendered porcine fat should be lower than the linear-fit value of 1.58 mm/$\mu$s.

The main mechanism proposed to explain curvature of the $U_s$-$u_p$ Hugoniot at lower particle velocities involves two stages: (1) initial reduction of the spaces between the polymeric chains, due to the existence of weak van der Waals forces, before; (2) secondary compression of the backbone carbon chain. Although this mechanism is arguably applicable to polymers in general, Carter et al. [16] discussed the existence of phase changes within certain polymeric materials at low pressures and how these could also account for such observations. Other theories describing this behaviour in polymers also exist, including the elastic-plastic flow model [118], which predicts extreme curvature of the Hugoniot at low particle velocities. Consequently, inclusion of the data-point corresponding to an impact velocity of 39 m/s, suggesting slight-curvature in the Hugoniot of the adipose material at low particle velocities (see Figure 8.2), supports evidence that the material possesses structural similarity to simple polymers.

In terms of basic repeat structure, the polymer chain of polyethy-

lene, which does not possess side group attachments, is somewhat similar to triglycerides (i.e. the adipose material examined in this body of work). Excluding the presence of glycerol within the triglyceride molecule, which is both a key structural component of fat and a functional group that will have significant effect on the response of the material to shock compression, the two materials both possess a long carbon chain without attachment - essentially a $CH_2$ repeat. The adipose material tested in this work exists as a semi-solid at room temperature due to the largely saturated nature of the fatty acid chains contained within it. Saturation of fatty materials may vary, however, and, as was previously discussed [13], variance in percentage saturation is known to have an effect on material firmness.

Notably, the frequency of the disturbance adopted during ultrasonic measurement in polymeric materials is known to have an effect upon their calculated sound speeds. For example, Mc Hugh [119] found a difference of $\sim 100$ m/s between sound speeds measured within a fully-cured epoxy when using ultrasonic transducers of 3 and 5 MHz. Over a temperature range of approximately 20-200 °C, Mc Hugh also found that a consistently lower sound speed was measured within the epoxy by the 3 MHz disturbance. As was discussed in Section 5.2, a frequency of 1.0 MHz was adopted during ultrasonic measurement of the adipose material investigated in this work in order to minimize attenuation of the signal. In addition, the sound speed for the adipose tissue was calculated using a value of 0.47 for Poisson's, which was chosen due to its close agreement with values measured elsewhere for sub-

cutaneous fat. As was previously mentioned, this approach resulted in a shear wave velocity of 0.35 mm/$\mu$s for the adipose material. It seems reasonable to suggest that, had access to ultrasonic transducers of lower ($< 1.0$ MHz) frequency been possible, the longitudinal wave speed that was detected within the material may have differed from the measured value. While still intrinsically difficult to achieve, the detection of a shear wave disturbance may also have been possible by adopting lower frequency transducers. Due to (a) the position of the datapoint corresponding to the lowest impact velocity and; (b) the overall tendency for polymeric materials to exhibit curvature a lower particle velocities, it seems reasonable to suggest that the true shear wave speed of the adipose material, and thus its bulk sound speed ($C_0$), may be significantly lower than the value estimated from information within the literature (i.e. 1.45 mm/$\mu$s). Again, the possibility of detecting a lower longitudinal sound speed in the material than the recorded value may also contribute to the existence of a somewhat reduced bulk sound speed (see Equation 2.27). It is possible that the rendering processes undergone by the adipose material may have acted to reduce its stiffness and thus reduce the maximum velocity at which shear disturbances may propagate within it. Of particular interest, and a possible area of future study regarding the shock response of adipose materials, is that of the behaviour of non-rendered fats, e.g. subcutaneous fat and/or calcaneal (heel) fat. Such investigation may help to clarify or provide answer to some of the issues raised by this work.

Millett and Bourne [15] studied the shock loading of polyethylene (no side group), polypropylene (methyl side group), and polystyrene (benzene side group). It was found that as the complexity, or size, of the side chain addition to the repeat unit increased, there was an increase in the shear strength of the material (i.e. its ability to resist compression under shock loading). Essentially, greater resistance to the compression that accompanies increases in stress was encountered with more complex polymer chain side groups. It is worth noting that glycerol, which is a major component present within the structure of triglycerides/triaglycerols (i.e, the adipose material) comprises three carbon atoms, three oxygen atoms, and five hydrogen atoms once chemically bonded to three fatty acid chains. In addition, a double covelant bond exists between the first carbon atom of each fatty acid chain and an oxygen atom. Given such complexity, it seems reasonable to suggest that a significant resistance to compression is anticipated within the measured shock response of the material.

It has been postulated that there is a direct link between both the key parameters of $C_0$ and S (i.e. the shock velocity at $u_p = 0$ and the slope of the equation-of-state in the $U_s$-$u_p$ plane, respectively) and physical material properties during shock loading. Specifically, values of S are known to depend upon the first pressure derivative of bulk modulus (K) [120]. As such, higher values of $C_0$ have been linked to a greater resistance to compression [32], while lower values of S have been linked to both increased resistance to compression and enhanced material stiffness [121].

As shown in Figure 8.2, the value of S is significantly lower for gelatin than the adipose material (1.77 and 2.47 respectively). This suggests one of two things: that 20 wt.% gelatin is a material of greater stiffness than the adipose material, and/or that it will exhibit greater resistance to compression than it. As mentioned, the adipose material comprises a structure that is closely similar to that found within polymeric materials and includes: (a) large sub-unit attachments, i.e. glycerol molecules, and (b) carbon-oxygen double-covelant bonds where fatty acid molecules bound to glycerol molecules. At first glance, the suggestion that a material with limited structural complexity, i.e. ballistic gelatin, should exhibit greater resistance to compression than the adipose material is somewhat surprising. However, it is worth noting that gelatin comprises 80% water; hence it will have a high degree of inherent incompressibility, as opposed to the hydrophobic adipose tissue.

Unlike 20 wt.% ballistic gelatin, which exhibited hydrodynamic behaviour during shock compression (i.e. it exhibited no significant shear strength) [95], the adipose adipose material tested here appears to strengthen under dynamic loading. This behaviour is reflected in an increase in the gradient of the experimental adipose material data above the hydrodynamic line with increased impact stress. This can be see in both the P-$u_p$ and P-V Hugoniot relationships, which are presented in Figures 8.3 and 8.4, respectively. The measured response curve for 20 wt.% gelatin, which was found to be equivalent to the predicted hydrodynamic response curve, is also included in Figure 8.3

in order to highlight the difference in behaviour between the adipose and simulant material during equivalent loading. Notably, pressure errors in the figures 8.3 and 8.4 were calculated from the maximum and minimum deviation in response from the Hugoniot stress (seen at point (c) in Figure 8.1). Volume errors were calculated using equation 8.8 (see Section 8.2) and both maximum and minimum shock and particle velocity values for a given experiment.

Hydrodynamic curves are calculated using Equation 8.4. From Figure 8.3 it is apparent that at $u_p = \sim 0.7$ mm/$\mu$s a difference in pressure of roughly 0.5 GPa would result between 20 wt.% ballistic gelatin and the rendered fat. This suggests that there is a significant difference in the response of the two materials at elevated particle velocities. At very high shock pressures (beyond the scope of the experiments presented here) one of two types of behaviour may be expected: (a) a significant and increased separation may develop between the measured response and that predicted by the hydrodynamic curve, or; (b) the data recorded for the adipose material may collapse back on to the predicted curve, signifying that hydrodynamic conditions have been reached. Notably, all materials typically fall back on to the hydrodynamic curve - the level of stress required to reach hydrodynamic behaviour simply differs from one material to another due to differences in physical structure.

$$P = \rho_0 U_s u_p \qquad (8.4)$$
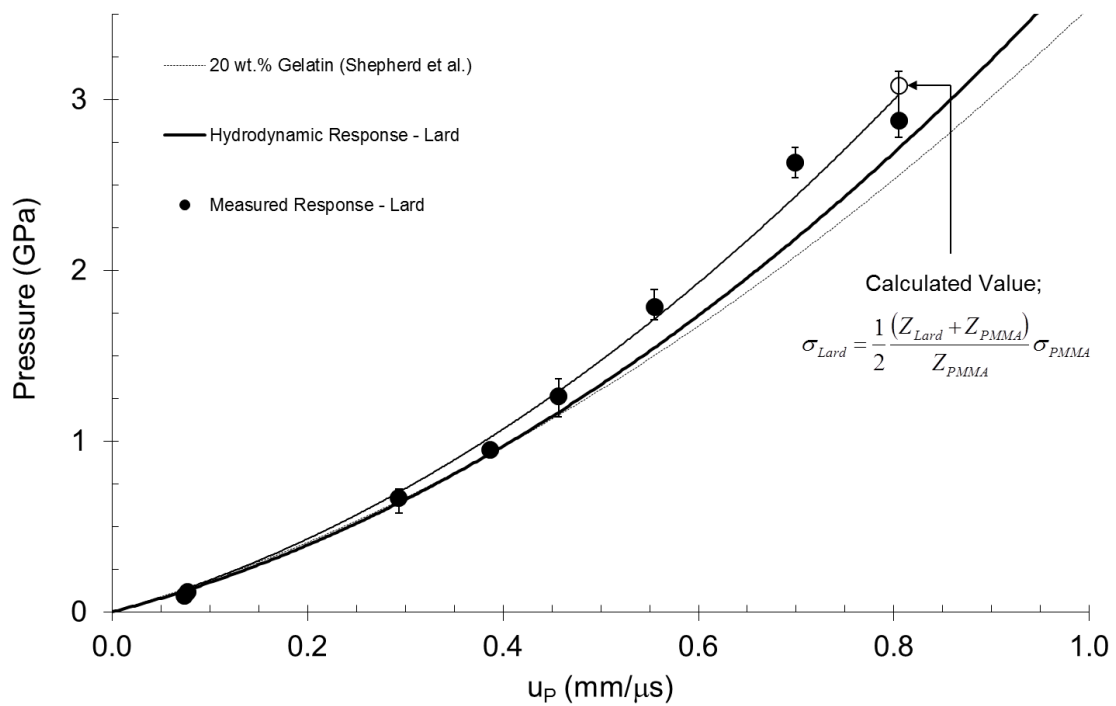
Figure 8.3: P-$u_p$ Hugoniot of the adipose material and 20 wt% ballistic gelatin
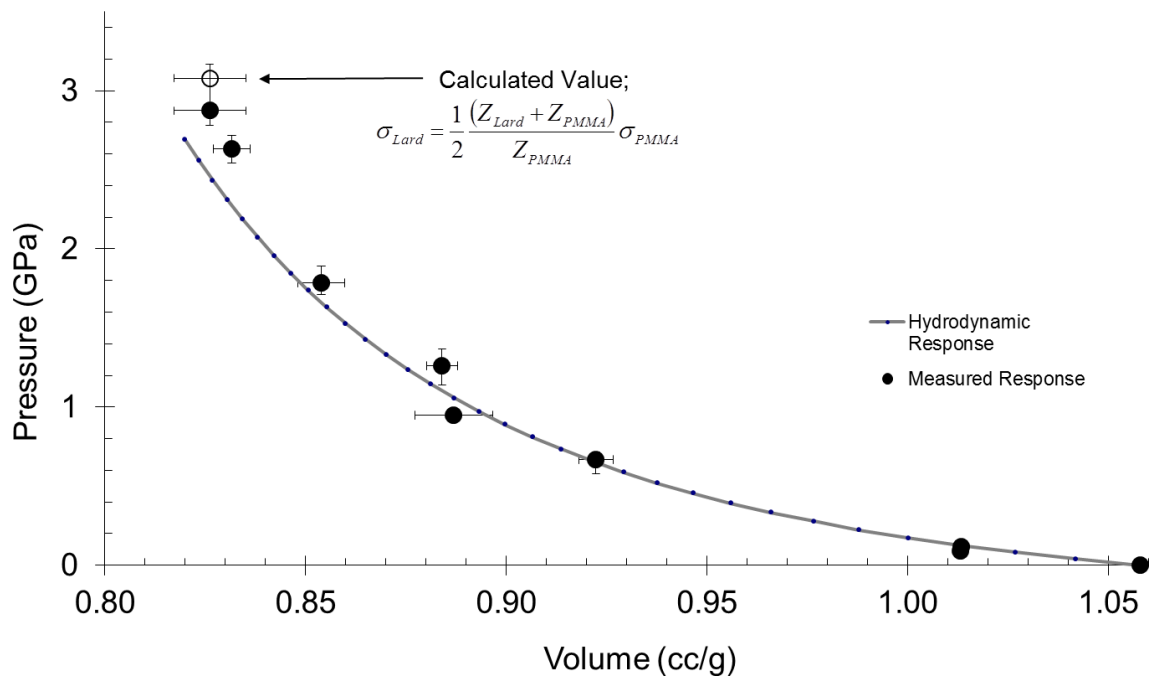


Figure 8.4: P-V Hugoniot of the adipose material

The pressure value for the datapoint corresponding to the largest longitudinal stress and particle velocity (882 m/s) in the P-u$_p$ and P-V Hugoniots (Figures 8.3 and 8.4, respectively) was calculated from the rear-surface trace using Equation 8.1. As is shown in both Hugoniot planes, there is some discrepancy between the front and (adjusted) rear-surface values for this datapoint. Despite this discrepancy, in both cases a measurable deviation from the hydrostatic response is seen to occur. This is indicative of strengthening. Adoption of the rear-surface value for $\sigma_x$ (longitudinal stress) in determining the experimental best-fit was felt to be justified here for two reasons: (i) due to good agreement with the deviation from the hydrostat apparent for the 758 m/s datapoint from (see Table 8.1 and Figures 8.3 and 8.4), and; (ii) due to anomalous features on the recorded front-gauge trace which made determination of a Hugoniot stress problematic. To reiterate, the long-chain structure of fat (i.e. the adipose material) and the observed strengthening in the P-$u_p$ and P-V planes under shock loading appears to be broadly similar to that of simple polymers over the range of investigated shock pressures (e.g. [122], [16] and [123]).

As has been discussed, the design specifications of the 50 mm single-stage gas gun used in this work ensured that all strain within the target material was accommodated along the impact axis. Upon impact, however, both longitudinal and lateral stress components are generated within sample materials. This is reliant upon the fact that during conditions of one-dimensional shock compression (1D strain) the stress state is three dimensional, due to inertial confine-

ment. Thus, $\sigma_x \neq \sigma_y = \sigma_z \neq 0$. Notably, the lateral stress components generated within materials under a state of one-dimensional shock have been measured extensively using manganin foil gauges, e.g. [124, 63, 110, 108]. Unlike the grid-type gauges employed during measurement of the longitudinal stresses imparted to sample materials, lateral stress measurement involves use of a T-type gauge element (see Section 4.2.2), which is embedded within the material flow during shock compression.

As discussed, both the longitudinal ($\sigma_x$) and lateral ($\sigma_y$) stress components within a one-dimensionally shocked material are often deviatoric in nature, i.e. of differing magnitude. When both the lateral and longitudinal response of a material to shock are well characterized, an indication of the change in shear strength within the material may be calculated (see Equation 8.6). It is generally accepted that the shear strength ($2\tau$) of a material governs its response under shock loading. The relationship between shear strength; the pressure (P), which is an average of the three components of stress ($\sigma_x, \sigma_y, and \ \sigma_z$); and the longitudinal stress ($\sigma_x$) is given by Equation 8.5.

$$\sigma_x = P + \frac{4}{3}\tau_{max} \tag{8.5}$$

$$2\tau = \sigma_x - \sigma_y \tag{8.6}$$

### 8.1.1   Lateral Response - Adipose Material

Plate-impact experiments were conducted using type J2M-SS-580SF-025 as a means to investigate the lateral stresses generated within the adipose material when subjected to a one-dimensional state of strain. In addition, and due to some debate within the literature regarding the use of lateral stress gauges in plate-impact experiments, comparison has been made between the effects of the presence, or lack there-of, of an encapsulating Mylar$^{®}$ layer around the gauge element (but not ahead of the gauge) upon its response to the shock. The four impact experiments conducted here correspond to impact velocities ranging from 346-804 m/s and a measured lateral stress range of approximately 0.5-2.0 GPa within the material. Initially, two experiments were conducted in which the gauge element and gauge package were encapsulated between two 50 $\mu$m Mylar$^{®}$ sheets. As was discussed in Section 7.3, lateral targets were initially assembled into a hollow, pre-cast construct prior to being filled with liquid adipose material. The two impact experiments in which an encapsulating layer was present around the gauge were subjected to impact by a 10 mm copper flyer at velocities of 405 and 682 m/s. Complimentary to these shots, another set of experiments, in which no encapsulating Mylar$^{®}$ layer was present, were conducted at impact velocities of 346 and 804 m/s. Again, a 10 mm copper flyer was used.

The types of materials in which lateral stress gauges are often used to measure the evolution of lateral stress during shock compression are typically rigid in nature, e.g. metals and polymers [110], [125], [126].

Notably, the adipose material adopted in thie work exists as a semi-solid at room temperature. Despite this, the techniques that have been adopted in this work have successfully allowed for the measurement of the behind-shock lateral stress component generated within the material by flyer-plate impact. By adopting a value of $c_0 = 1.45$ mm/$\mu$s ([116], [117]) and taking Poissons ratio to be 0.47, lateral response data for the adipose material has been presented in this work as calibrated stress-time plots (see Figure 8.5). Information regarding the calibration and interpretation of the data obtained from type J2M-SS-580SF-025 lateral stress gauges in plate-impact experiments is presented in Section 4.2.2. The stress values presented in Figure 8.5 are later used during calculation of the change in shear strength ($2\tau$) of the material as a result of shock compression.

At impact velocities of 804 m/s and 346 m/s gauge elements were positioned 4 mm from the impact face of the target, whilst a distance of 6 mm was used during the 682 m/s and 405 m/s experiments. Such placement corresponds to distances of 6 and 4 mm respectively from the rear of the 10 mm target ring in all but the 346 m/s shot. In the case of the 346 m/s impact, a smaller target ring thickness of 6 mm meant that the gauge element sat only 2 mm from the rear of the target when placed at a distance of 4 mm from the impact face. This arrangement produced unfavourable noise within the 346 m/s trace from t = 1.5 $\mu$s onwards, most likely due to re-loading upon reflection of the shock from the rear of the target. As a result, the 346 m/s data for t >1.56 $\mu$s after impact has been omitted from the lateral gauge
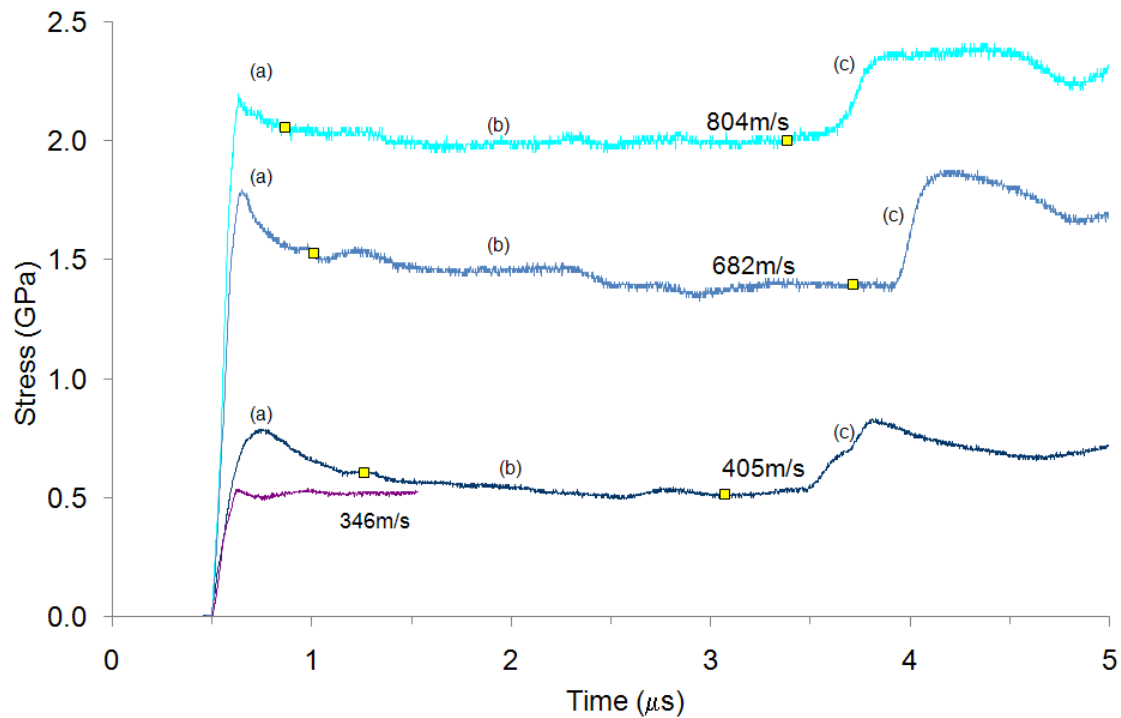
Figure 8.5: Lateral shock response of the adipose material

traces in Figure 8.5.

In Figure 8.5, square markers have been included to highlight the range over which gradients behind the shock were established. These gradients can be found in Table 8.2. In addition, these markers also correspond to the lateral stress values used in subsequent calculation of the initial and final shear strength states within the material (see Figure 8.6 and Table 8.3 in later discussion). Square markers, have not been included on the 346 m/s trace due to the aforementioned loss of signal after t >1.56 $\mu$s. Consequently, this trace is also not used in calculation of either a behind-shock gradient or a change in shear strength.

There are a number of points to note from the lateral response data

for the adipose material (see Figure 8.5). Firstly, as impact velocity increases, so do both the initial gradient (rise-time) and amplitude of the gauge response corresponding to shock arrival. Such behaviour is indicative of (i) an increase in shock velocity, and, (ii) the subsequent increase in pressure generated within the target material as a result of greater shock velocity. It should be noted that this type of response is expected from the relative change in impact conditions.

An initial overshoot (a) can be seen to occur upon shock arrival at impact velocities of 405, 682, and 804 m/s in Figure 8.5. However, this artefact appears to be significantly enhanced in targets where an encapsulating layer was present i.e. at impact velocities of 405 and 682 m/s. Notably, an overshoot is not clearly discernible at 346 m/s, which lacked a Mylar$^{®}$ encapsulating layer. Similar overshoots to those seen in the lateral response of the adipose material have been observed in longitudinal gauge traces (Figure 8.1). This behaviour in longitudinal gauges, however, has been attributed to an electrical capacitance effect between the gauge and the surface of the target material [111].

One explanation proposed in the literature for such overshoots in lateral gauge response is based on the concept of differing shock velocities in the target/matrix (generally metals and polymers) and the encapsulation layer, leading to the formation of a Mach-stem. Hydrocode simulations undertaken by Winter and Harris [127] indicated that if the shock in the matrix runs ahead of the shock in the encapsulation, the pressure, and hence the determinant stress, will be initially characterized by an overshoot with a subsequent decay in

181

magnitude behind. Conversely, a continuous rise in pressure/stress with time would be apparent when the shock in the matrix lags the shock in the encapsulation. It is worth noting that slight negative gradients are apparent behind the shock in the adipose material (see (b) in Figure 8.5). The calculated magnitudes of the gradients - taken between the two square markers on the gauge traces  are presented in Table 8.2. At first glance, the experimental results seem to suggest that the overshoot witnessed upon shock arrival is, as proposed by Winter and Harris [127], an artefact caused by Mach-stem formation between the matrix and the encapsulating Mylar$^{®}$ layer/gauge packaging. However, the combination of; (i) rapid rise times witnessed for longitudinal gauges (<125 ns), suggesting a close match in impedance between the gauge packaging and the epoxy resin used in target construction, and; (ii) the form of the Hugoniot relationships of epoxy resin and PMMA within the literature ($U_s = 2.65 + 1.55u_p$ [44] and $U_s = 2.59 + 1.52u_p$ [16] respectively) suggests that the velocity of the shock in the gauge encapsulation, modelled as either PMMA or epoxy resin, will be greater than the velocity of the shock in the matrix (adipose material) at particle velocities <1.16 mm/$\mu$s. Lateral experiments conducted here correspond to particle velocities of less than 1 mm/$\mu$s. Consequently, the overshoots witnessed in stress upon shock arrival are unlikely to be the result of a Mach-stem between the matrix and the gauge package in this case. Evidence of a slight overshoot at the higher impact velocity of 804 m/s, despite exclusion of an encapsulating Mylar$^{®}$ layer, suggests that the overshoot is part of

| Impact velocity (m/s) | 405 | 682 | 804 |
|:---|:---:|:---:|:---:|
| Gradient behind the shock (GPa/μs) | −0.049 | −0.048 | −0.021 |

Table 8.2: Lateral gauge gradients established behind the shock

an inherent response of lateral gauges to the onset of shock. However, it is reasonable to suggest that this artefact may only be observed at significant levels at higher impact velocities e.g. 804 m/s. At point (c) in Figure 8.5, reloading occurs, most likely as the result of a reflection of the shock from the PMMA backing material, due to its higher density and shock impedance.

For a given material, if longitudinal stress remains constant whilst lateral stress decreases, Equation 8.6 dictates that the shear strength will increase. The adipose material has been observed to exhibit both constant longitudinal stress (see point (c) in Figure 8.1) and negative gradients behind the shock in lateral investigations. This therefore suggests the possibility of an increase in shear strength within the material under shock loading conditions. This result correlates well with lateral response data for polymers elsewhere [123], [107].

The change in shear strength with longitudinal stress for the adipose material, 20 wt.% ballistic gelatin, and ballistic soap is presented in Figure 8.6. Data corresponding to the impact conditions experienced by each material is further highlighted in Table 8.3. While the change in lateral stress behind the shock was measured experimentally, the longitudinal stress data presented within Table 8.3 was calculated by applying a polynomial fit to the pressure-particle velocity Hugo-

niot for each material (where particle velocity was derived from both the impact conditions and the appropriate Hugoniot relationships, i.e. using the impedance matching technique). Shear strength $(2\tau)$ was calculated using Equation 8.6. Notably, data for 20 wt.% ballistic gelatin and ballistic soap was both taken from the literature [128, 129] and sourced from previous work undertaken at Cranfield university.

From Figure 8.6 it can be seen that, as longitudinal stress increases, so too does the shear strength of both the adipose material and ballistic soap. Further, it would appear that there is an increased separation of the initial and final shear strength states within the materials as impact stress rises from 0 to c.2.2 GPa. At impact stresses higher than c.2.2 GPa, the degree of separation between the initial and final shear strength states for each material appears somewhat reduced. However, overall shear strength itself continues to increase with impact stress. This reduction may reflect a structural change within the material; however, in the absence of a more definitive dataset (i.e. an extensive dataset comprising a greater number of datapoints and an increased range of impact stresses), it is not possible to provide further comment on this apparent change.

Notably, a clear difference between the initial and final shear strength states within the adipose material and ballistic soap becomes apparent as impact stress increases from 1 to 2 GPa (see Figure 8.6). At impact stresses lower than 1 GPa, however, little difference is observed between the initial and final shear strength states in either material. Both the overall trend showing an increase in shear strength
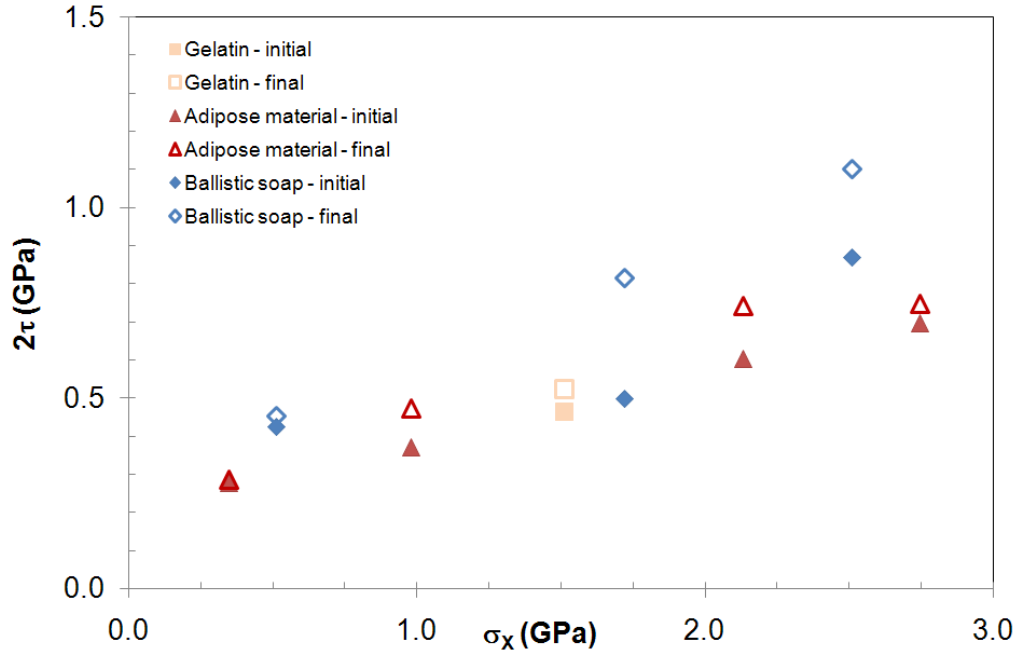
Figure 8.6: Change in shear strength with longitudinal impact stress for the adipose material, ballistic soap, and ballistic gelatin

with impact stress and the relative increase in shear strength for a given impact stress in both the adipose material and ballistic soap is indicative of material strengthening. As was previously shown in the P-u$_p$ plane (see Figure 8.3), the measured response for the adipose material rises-above the predicted hydrodynamic curve at impact stresses in excess of 1 GPa. This seems to both reinforce and be in agreement with the suggestion of strengthening within the adipose material over this range of investigated shock conditions. The most likely mechanism behind such behaviour is that of steric hindrance, i.e following initial reduction of van-der Waals spacings, the long chain molecules comprising the structure of the adipose material begin to compress to a greater extent as impact stress increases. Notably, this behaviour

has been noted elsewhere in materials of a polymeric nature, including Sylgard [126], ballistic soap [128], and polystyrene [15]. Of further interest is that the measured responses of both Sylgard and ballistic soap within the P-u$_p$ Hugoniot have both been seen to rise above the hydrodynamic response curve at c.1.2 GPa. Again, both of these materials possess polymeric structures and exhibit behaviour that is highly comparable to the measured response of the adipose material tested here. While no conclusive study into whether or not this type of behaviour is applicable to polymeric materials in general, the change in response at c.1.2 GPa may indicate a clear threshold at which compression of the hydrocarbon backbone becomes a component of observed shock response. Also unknown is at what point the onset of failure, i.e. collapse to a hydrodynamic response as a result of increased impact stress, occurs within either the adipose material or ballistic soap.

|  | Adipose material | Ballistic soap | 20wt.%gelatin |
|---|---|---|---|
| $\sigma_x$ (GPa) | 0.35 (194 m/s) | 0.51 (191 m/s) | 1.51 (600 m/s) |
|  | 0.98 (405 m/s) | 1.72 (526 m/s) | – |
|  | 2.13 (682 m/s) | 2.51 (652 m/s) | – |
|  | 2.75 (800 m/s) | – | – |
| Initial $\sigma_y$ (GPa) | 0.07 (194 m/s) | 0.09 (191 m/s) | 1.05 (600 m/s) |
|  | 0.61 (405 m/s) | 1.22 (526 m/s) | – |
|  | 1.53 (682 m/s) | 1.64 (652 m/s) | – |
|  | 2.05 (800 m/s) | – | – |
| Final $\sigma_y$ (GPa) | 0.06 (194 m/s) | 0.06 (191 m/s) | 0.99 (600 m/s) |
|  | 0.51 (405 m/s) | 0.90 (526 m/s) | – |
|  | 1.39 (682 m/s) | 1.41 (652 m/s) | – |
|  | 2.00 (800 m/s) | – | – |
| Initial $2\tau$ (GPa) | 0.28 (194 m/s) | 0.42 (191 m/s) | 0.46 (600 m/s) |
|  | 0.38 (405 m/s) | 0.50 (526 m/s) | – |
|  | 0.60 (682 m/s) | 0.87 (652 m/s) | – |
|  | 0.70 (800 m/s) | – | – |
| Final $2\tau$ (GPa) | 0.29 (194 m/s) | 0.45 (191 m/s) | 0.52 (600 m/s) |
|  | 0.47 (405 m/s) | 0.82 (526 m/s) | – |
|  | 0.74 (682 m/s) | 1.10 (652 m/s) | – |
|  | 0.75 (800 m/s) | – | – |

Table 8.3: Lateral stress and shear strength data for the adipose material, ballistic soap, and 20 wt.% ballistic gelatin (see also Figure 8.6)

## 8.2 Porcine Skeletal Muscle

A total of 20 plate-impact experiments were conducted during investigation of the bulk shock response of porcine skeletal muscle tissue. Of these, fifteen involved the commercially-available tissue and five involved the middle-white tissue. However, due to gauge failure, not all provided useful Hugoniot stresses (i.e. in some cases, only shock and particle velocities were obtained). Three plate-impact experiments involving the homogenized tissue variant were also conducted. The plate-impact experiments involving muscle tissue correspond to an impact velocity range of 190 - 1000 m/s and a particle velocity range of $\sim$ 0.18 - 0.91 mm/$\mu$s. Further, the range of investigated impact velocities correspond to a measured (Hugoniot) stress range of 0.73 - 3.69 GPa within the commercially-available tissue and a stress range of 0.62 - 2.70 GPa within the middle-white tissue. As was discussed in section 4.2, longitudinal shock response was measured using Vishay$^{\circledR}$ Micro-Measurements$^{\circledR}$ & SR-4$^{\circledR}$ Type LM-SS-125CH-048 manganin foil pressure gauges.

A typical example of the stress-time history for the commercially-available tissue is presented in Figure 8.7. This trace is also typical of those obtained for the middle-white tissue. There are a number of points to note with respect to (Figure 8.7). As with the longitudinal shock traces for the adipose material, the front surface gauge highlights the stress generated within the porcine muscle tissue, while the rear surface gauge shows the stress measured within the PMMA backing material. A higher stress is observed within the PMMA backing ma-

| Experiment number | Tissue type | Impact velocity $(m/s)$ | $U_s$ $(mm/\mu s)$ | $u_p$ $(mm/\mu s)$ | $\sigma_x$ $(GPa)$ |
|---|---|---|---|---|---|
| 1 | Commercial | 190 | 2.05 | 0.18 | ... |
| 2 | Commercial | 220 | 2.08 | 0.21 | ... |
| 3 | Commercial | 270 | 2.22 | 0.25 | 0.73 |
| 4 | Commercial | 310 | 2.19 | 0.29 | 1.02 |
| 5 | Commercial | 357 | 2.42 | 0.33 | 1.07 |
| 6 | Commercial | 403 | 2.49 | 0.38 | ... |
| 7 | Commercial | 407 | 2.38 | 0.38 | 1.29 |
| 8 | Commercial | 409 | 2.51 | 0.38 | 1.37 |
| 9 | Commercial | 484 | 2.56 | 0.45 | ... |
| 10 | Commercial | 497 | 2.59 | 0.46 | 1.70 |
| 11 | Commercial | 600 | 2.72 | 0.55 | 1.95 |
| 12 | Commercial | 776 | 3.03 | 0.71 | ... |
| 13 | Commercial | 804 | 3.07 | 0.74 | 2.85 |
| 14 | Commercial | 874 | 3.18 | 0.80 | ... |
| 15 | Commercial | 1000 | 3.48 | 0.91 | 3.69 |
| 16 | Middle-White | 325 | 1.91 | 0.21 | 0.62 |
| 17 | Middle-White | 342 | 2.08 | 0.21 | ... |
| 18 | Middle-White | 521 | 2.76 | 0.48 | 1.70 |
| 19 | Middle-White | 817 | 2.99 | 0.75 | 2.70 |
| 20 | Middle-White | 833 | 3.07 | 0.76 | ... |
| 21 | Homogenized | 356 | 2.21 | 0.33 | 0.98 |
| 22 | Homogenized | 449 | 2.42 | 0.42 | 1.27 |
| 23 | Homogenized | 677 | 2.90 | 0.61 | 1.96 |

Table 8.4: Experimental and equation-of-state data for the investigated porcine muscle tissues

terial than within the porcine muscle tissue due to the higher density of the PMMA and its greater shock impedence (Z), where $Z = \rho_0 U_s$. Both gauges show rapid rise-times (c.62 ns) at point (a), despite the adoption of 195 $\mu$m Mylar® insulation in the given example. This is indicative of good target alignment and implies that the measured response is representative of true one-dimensional shock loading within the sample material. The use of increased levels of Mylar® protection in plate-impact experiments involving skeletal muscle was sought in an attempt to minimize noise, which was initially seen to occur in gauge traces provided with lesser insulation/protection. After the arrival of the shock, ringing (point (b)) is observed within the front surface gauge. Thus, although the adoption of increased Mylar® protection in experiments was successful in reducing the levels of noise originally witnessed within lesser-protected gauge traces, this reduction was not always complete. A near constant Hugoniot stress can be seen at point (c). This Hugoniot stress - seen to vary with impact pressure - is later used in the construction of the stress-volume Hugoniot for the porcine muscle tissue. A release wave from the rear of the copper flyer eventually catches up with the incident shock at point (d), due to its higher velocity of propagation. Finally, a loss of 1D conditions within the sample occurs at point (e).

The $U_s$-$u_p$ (shock velocity-particle velocity) Hugoniot for the commercially-available tissue is presented in Figure 8.8. Notably, the tissue possesses a comparable linear relationship ($U_s = 1.72 + 1.88u_p$) to the adipose material investigated in this work ($U_s = 1.58 + 2.47u_p$)
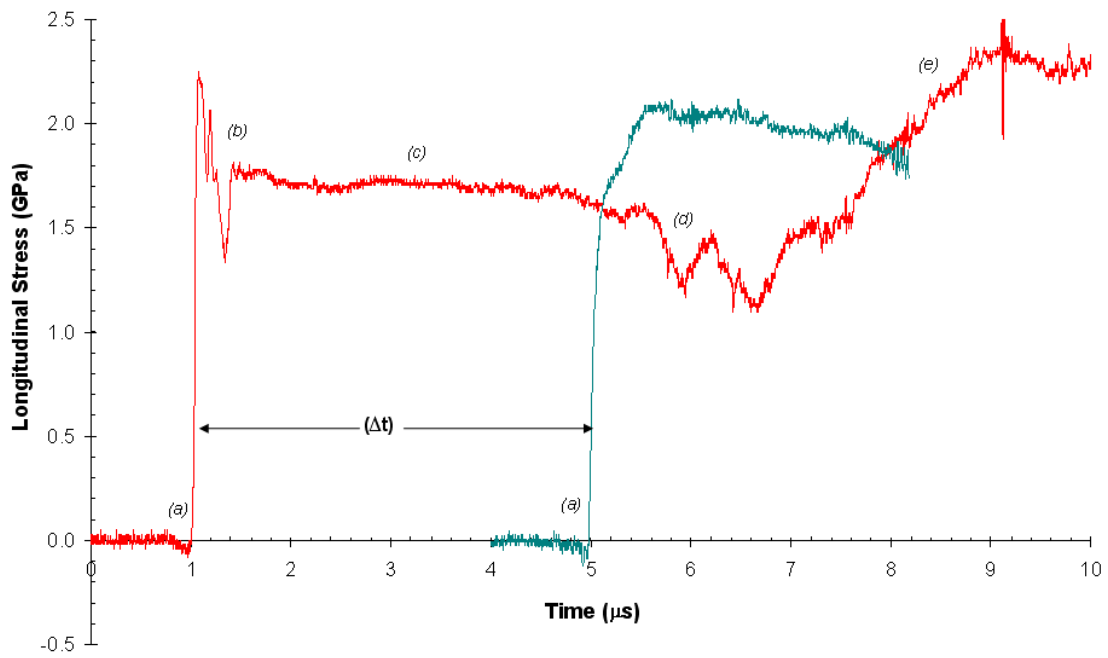
Figure 8.7: Stress-time history corresponding to a 10 mm Cu flyer impacting a 10.012 mm thick sample of the commercially-available tissue at 497 m/s
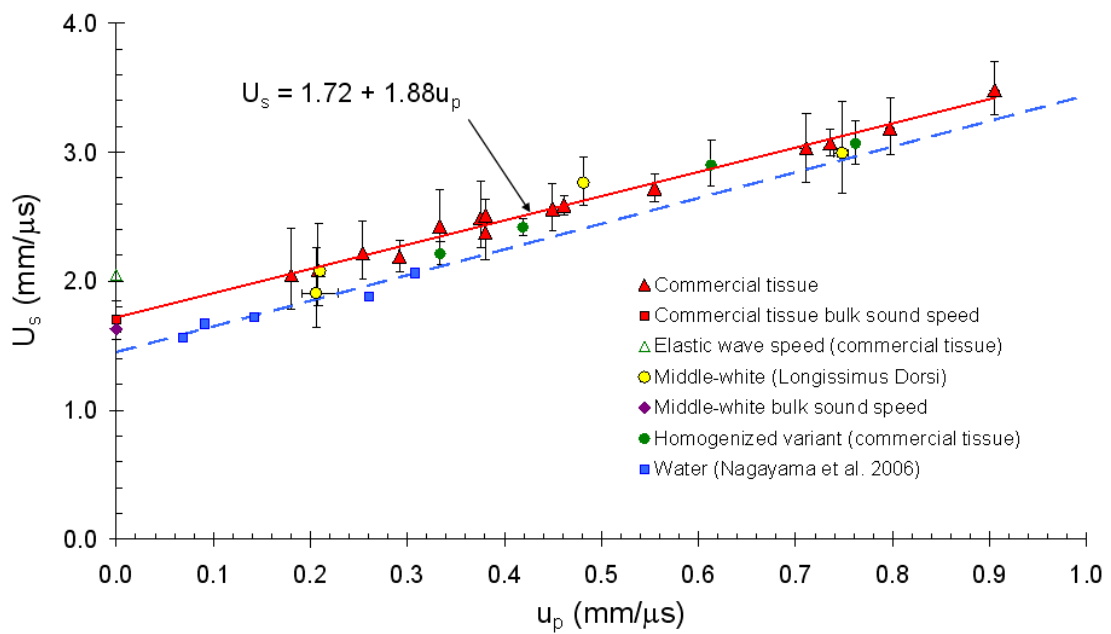


Figure 8.8: $U_s$-$u_p$ Hugoniot for porcine skeletal muscle tissue (comparison made with water [112])

191

and to that of water, which was established elsewhere [112] ($U_s = 1.45 + 1.99u_p$). The data corresponding to the middle-white tissue lies closely on this Hugoniot, suggesting no significant difference between the responses of the two materials, despite possible differences in their treatment (inclusion of additives, ageing, etc.) and the muscles from which they were removed. For comparative purposes, the linear EoS for water [112] is also included in Figure 8.8.

As was discussed in the results section for the adipose material (see Section 8.1), the slope of the prinicpal Hugoniot in the $U_s$-$u_p$ plane (S) is dependent upon first pressure derivative of bulk modulus. Moreover, it was also discussed that the slope of the Hugoniot is known to bear influence on the relative compressibility of the material. While a greater shock velocity would result within porcine muscle tissue than water at given particle velocity, the overall slope of the Hugoniot for each material is roughly equivalent. While not yet giving consideration to measured longitudinal or shear stresses within the material, this suggests that (in the $U_s$-$u_p$ Hugoniot) it is the high water content of the material that may bear the greatest influence upon its relative compressibility during shock compression. Due to the limited dataset provided for water by Nagayama et al. [112], it is not possible to confidently apply any suggestion or discussion regarding the behaviour or or interaction of the two materials in this section to particle velocities above c.0.32 mm/$\mu$s.

Despite its relatively high water content ($\sim 65\%$), the shift in position of the muscle Hugoniot above that established for water in the

U$_s$-u$_p$ plane yields indication that the fibrous element of the tissue may be providing an avenue for an increased velocity of shock propagation. Arguably, it is this velocity that is detected by the manganin foil gauges, which provide an averaging output over their occupied area. It seems reasonable to suggest that regions of the shock within the fluid layer may lag behind those in the (protein-based) fibrous elements of the tissue, i.e. the difference in shock velocity seen between the Hugoniots for water and skeletal muscle tissue (8.8). It seems most likely that due to: (a) a lack of discrimination regarding fibre alignment within the tissue samples (i.e. the bulk response measured in this work); (b) the averaging nature of the wire element gauges, and; (c) the resolution of the gauges, that a two-stage shock arrival was not discernible within the experimental results. By using a diagnostic capable of providing spatial resolution of the relative shock velocities in an inhomogeneous sample such as muscle tissue (i.e. line VISAR [130, 131, 132]), the detection of a two-stage shock arrival may be possible in a 1D plate-impact experiment. However, such detection would most likely only be possible in samples exhibiting a degree of structural conformity, i.e. muscle fibres aligned predominately with, or orthogonal to the impact axis.

The linear intercept for the commercially-available muscle tissue (an average value of 1.72 mm/$\mu$s) holds good agreement with the bulk sound speeds that were determined for the two tissue types via ultrasonic methods here (1.70 $\pm$ 0.15 mm/$\mu$s and 1.63: +0.14; -0.09 mm/$\mu$s, respectively). The intercept also holds good agreement with

sound speed values that are typically accepted within the literature for skeletal muscle (c.1.63 mm/$\mu$s) [92], [117]. This shows that, unlike polymers, which possess similar acoustic impedance to the porcine tissues tested here, there is no curvature of the Hugoniot at low particle velocities, e.g. [44], [31].

Figure 8.9 shows the pressure-volume (P-V) Hugoniot for all of the tested tissues and includes the hydrodynamic response curves for both muscle tissue and water for comparative purposes. The hydrodynamic response of each material is calculated using Equations 8.7 and 8.8. For muscle, this was performed using the linear EoS values obtained for the commercial tissue ($U_s = 1.72 + 1.88u_p$). Both the measured response of the adipose material [133] and an exponential trend-line, which has been plotted through the measured data points for the commercial muscle tissue alone, are also included in the Hugoniot. The response of the muscle tissues is clearly dissimilar to that of the rendered porcine fat investigated in this study. This is mainly due to the differing densities of the two materials, although the uniqueness of the equations-of-state formed for each material will also have influence upon both their hydrodynamic (i.e. $P = \rho_0 U_s u_p$) and measured responses. Pressure errors in Figure 8.9 are presented in terms of a maximum and minimum deviation in response from the Hugoniot stress (determined at point (c) in Figure 8.7). Volume errors were calculated using the maximum and minimum shock and particle velocities for an individual experiment (see Equation 8.8). Particle velocities for use in error calculation were derived using of a set of quadratic coefficients

based upon the maximum and minimum (measured) shock velocities in an experiment, i.e. adoption of the impedance matching technique (see Section 3.2). Shock velocity, and thus shock velocity errors, were measured experimentally.

$$P = \rho_0 U_s u_p \qquad (8.7)$$

$$V = V_0 \left( \frac{U_s - u_p}{U_s} \right) \qquad (8.8)$$

During this study the adipose material has been shown to strengthen under shock conditions in a manner not dissimilar to that occurring within polymeric materials. This was indicated by levels of measured stress lying above those predicted by the hydrodynamic response curve in the P-V Hugoniot (see Figure 8.4). There are indications that the shock responses of the porcine tissues examined here are also non-hydrodynamic, although the mechanism behind any material strength is suggestively dissimilar to that of the fatty material. For the adipose material, the hydrodynamic and measured response curves were shown to be divergent in nature, i.e. a greater difference in measured stress compared to hydrodynamic stress was observed as impact velocity increased. No such clear distinction is apparent for the collective muscle tissue data. Instead, the experimental data largely sat very close to the hydrodynamic curve. When taken in its entirety, however, the overall trend of the data appears to suggest a
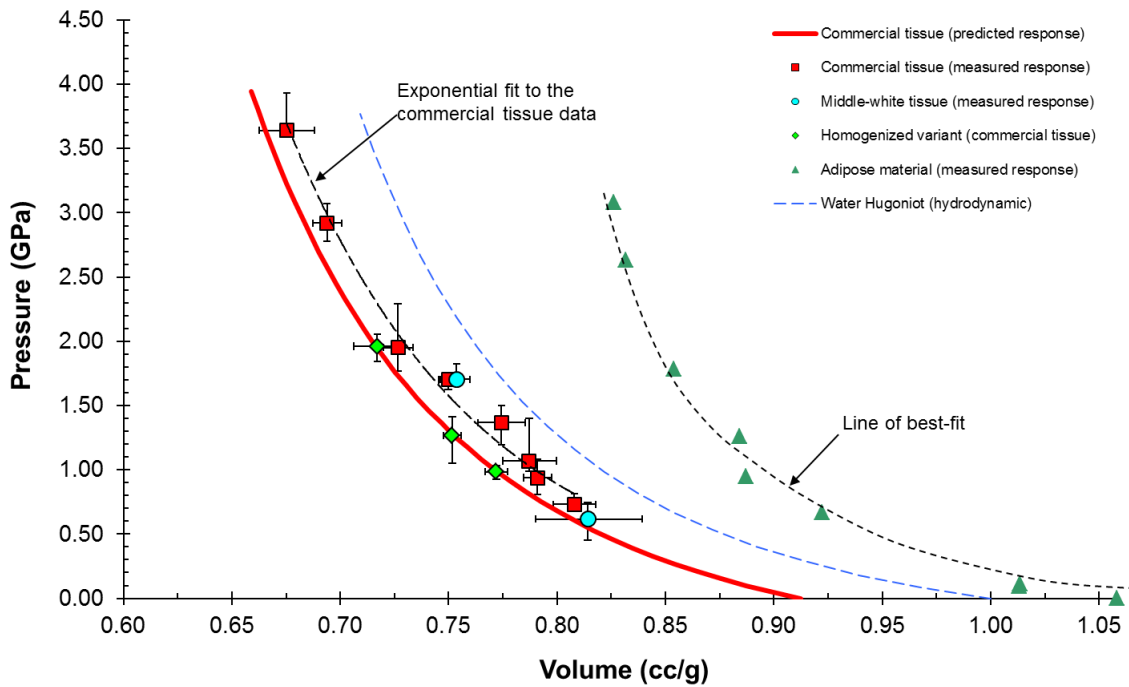
Figure 8.9: Pressure-Volume Hugoniot for the examined muscle tissues

consistently (slightly) higher stress than the predicted hydrodynamic response at all impact velocities. Thus, in contrast with both material flow strength which decreases with pressure (softening) and material flow strength which increases with pressure (hardening), the porcine muscle tissues appear to exhibit a near constant flow strength which is independent of pressure. It must be stressed that this apparent flow strength is only observed for impact stresses up to c.3.6 GPa, has only a very small magnitude, and sits, in many cases, within the calculated experimental errors. These findings suggest that both 20wt. % ballistic gelatin and water, which have both been shown to behave entirely hydrodynamically under shock loading conditions, may not accurately reflect the behaviour of skeletal muscle tissue under equivalent rates of strain.

The datapoints for the homogenized variant of the commercially-available tissue lie on the hydrodynamic response predicted for skeletal muscle. As mentioned previously, despite relatively large experimental errors (arising from the inherent inhomogeneity of the tissue), when considered as a collective data set, the response of the virgin tissue is dissimilar to the homogenized variant, i.e. the stress-volume data appears to lie slightly above the predicted hydrodynamic response (see Figure 8.9). Given that the overall components within the virgin and homogenized materials were identical; this difference in behaviour is most likely the result of their structural dissimilarity, i.e. the quasi-organized structure of skeletal muscle versus its disrupted counterpart. The observed difference in response suggests that the strength or resistive mechanism displayed for the unaltered muscle tissues is due to the dynamic response of the fibrous, structured components found within their makeup - none of which are present within the homogenized sample material. The integrity of the connective tissues within the unaltered tissues, e.g. the endomysium, which separates individual muscle fibres from one another, may also bear influence on the difference in observed behaviours. It must be emphasized that the previously outlined and large experimental errors associated with the presented dataset for the investigated materials promote the requirement for further study before it would be possible to begin to quantify resistive/strain-hardening effects during shock loading.

## 8.3 Shock-Recovery of Porcine Skeletal Muscle Tissue

By adopting the finalized experimental approach detailed in Section 6, two successful shock-recovery experiments were performed during this research project. Specifically, one experiment was conducted upon the commercially-available tissue and another upon tissue from the middle-white. In both experiments fibre alignment of the samples was predominately parallel to the impact axis, i.e. such that the shock would migrate along, rather than across the fibres. The commercially-available and middle-white soft-capture vessels were impacted at 216 and 223 m/s, respecitvely, and each with a 10 mm thick aluminium flyer. Prior to experiment, control tissue was excised from each of the un-shocked samples and prepared for analysis by Transmission Electron Microscope (TEM). Following recovery, tissue was removed from the shocked sample and subject to identical treatment. The treatment process, i.e. fixation and other the preparatory stages required for TEM analysis, is outlined in Section 5.1. From each of the control and shocked variants of the two tissue types both longitudinal (LS) and transverse (TS) sections were taken for microscopic analysis.

Given the highly similar behaviour of the two tissue types under shock loading (shown previously in Hugoniot data) and the similar impact conditions of the two shock-recovery experiments (216 and 223 m/s), numerical simulation of only the 216 m/s experiment involving the commercially-available tissue is presented here. Further

information about the models used in the numerical simulation of the soft-capture experiments can be found in Section 6. As was discussed in Chapter 6, two major design features were incorporated into the finalized design of the soft-capture system. Firstly, a backing material of lower acoustic impedance than skeletal muscle (i.e. gelatin) was adopted. This has ensured that the majority of the incident shock has been transmitted into the backing material and that any reflection/reloading from the rear of the sample has been minimal. Secondly, the capsule backing section was extended towards infinity. This reasoning behind this design feature was discussed in Chapter 6 (capsule development) and is expanded upon later in this section.

A number of schematics/illustrations are provided in this section in an attempt to deconvolute the information held within the simulated results. These include: (i) a schematic of the modelled components within the soft capture system (Figure 8.10); (ii) a detailed illustration of the modelled event at t = 1 $\mu$s (Figure 8.11); (iii) an overview of the progression of shock interaction within the soft-capture system (Figure 8.12), and; (iv) the modelled stress-time history experienced by the tissue sample (Figure 8.13). In the model figures, red indicates regions of higher pressure/stress while green and then blue indicate regions of lower pressure/stress. In addition, both the fixed (for all simulations) pressure scale-bar in Figure 8.11 and the modelled stress-time history in Figure 8.13 provide a more detailed overview of the evolution of shock pressure/stress within the capsule during impact.

At t = 1 $\mu$s after impact (see Figure 8.11) it can be seen that
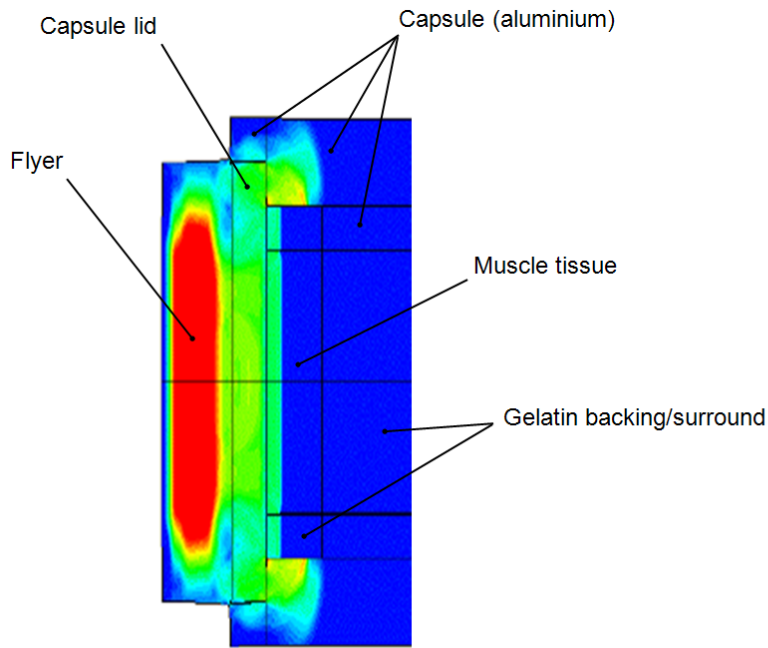
Figure 8.10: Schematic of model constituents
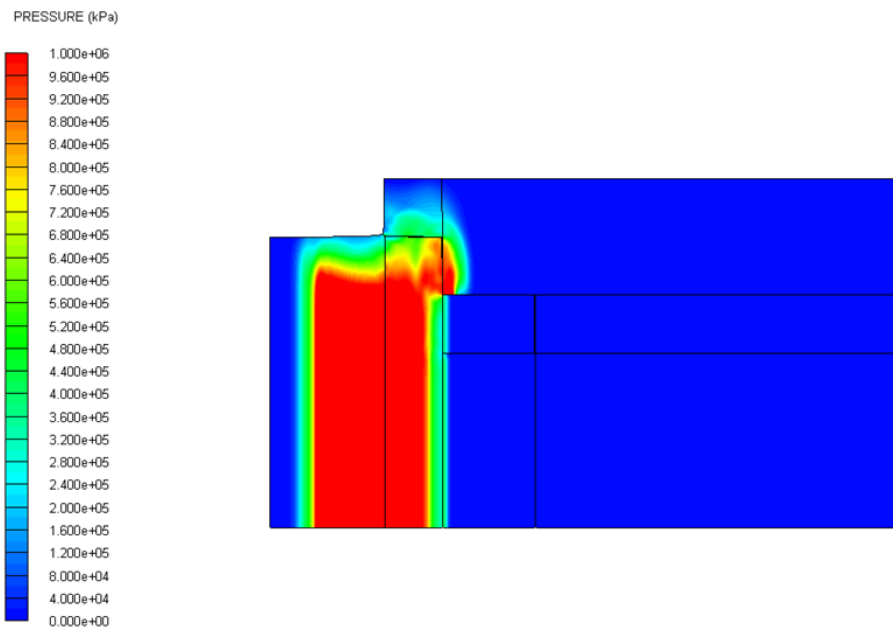


Figure 8.11: Model of a 216 m/s Aluminium flyer impacting the soft-capture system at t = 1 $\mu$s (note: the fixed pressure scale-bar presented in this figure corresponds to the pressure colour-scale in all simulations presented in Section 8.3)

the shock has migrated from the point of impact both towards the muscle tissue sample and back towards the rear of the flyer. Notably, the shock propagating within the walls of the capture vessel has migrated the same distance forward as the shock migrating back towards the rear of the flyer. This is a result of the flyer and the vessel being of equal impedance/material composition. Dissimilarly, the part of the shock that has entered into both the tissue sample and gelatin surround is seen to lag behind that propagating within the vessel walls. This behaviour, along with the reduced pressure/stress observed within two components (tissue and gelatin surround), is due to their lower shock impedance compared to that of the surrounding aluminium. Upon reaching a material of lower impedance, i.e. the muscle tissue sample, a reflected component of the incident shock has caused a reduction in shock pressure within the capsule lid (see Figure 8.11). Finally, release waves are seen to enter from the peripheral free surface regions of the flyer and flyer-vessel interface at t = 1 $\mu$s.

The information presented within Figure 8.12 is best described per independent time division, i.e. at 2, 3, 6, and 10 $\mu$s respectively. At t = 2 $\mu$s, the shock running within the walls of the capture vessel has far exceeded that within the tissue sample. While the shock within the vessel walls has been influenced by the peripheral geometry of the system, the shock within the tissue sample remains largely one-dimensional at this point in time. The reflected shock at t = 2 $\mu$s has almost reached the rear surface of the flyer. In addition, release waves from the periphery of the flyer and flyer-vessel interface (also
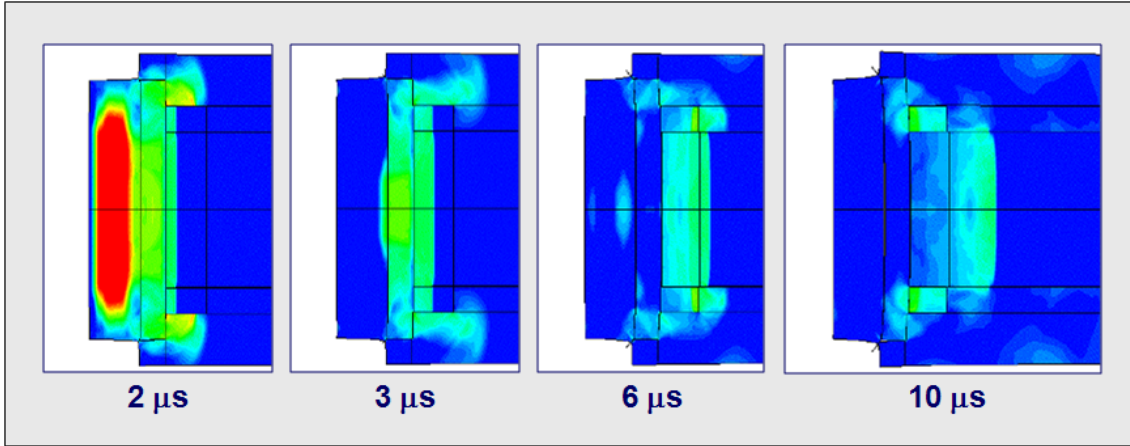
Figure 8.12: Numerical simulation of 216 m/s shock-recovery experiment

seen at t = 1 $\mu$s) continue to migrate inwards. At t = 3 $\mu$s, however, these regions of interference are overtaken by a tensile release wave propagating at a higher velocity from the rear of the flyer. Here, the shock within the tissue has migrated through approximately half of the sample thickness ($\sim$ 4 mm) and, despite curvature of the disturbance at the outer edges, appears to remain largely planar. At t = 6 $\mu$s the compressive shock has completely passed the tissue sample and has entered into the gelatin backing. In addition, the release from the rear of the flyer appears to have entered the front of the tissue sample, although its exact position is somewhat difficult to identify.

Finally, at t = 10 $\mu$s, the shock has dispersed into two elements. The first continues to propagate through the gelatin backing. However, the release wave from the rear of the flyer is fast approaching this compressive front. The second element of the shock continues to ring

(i.e. reflect back-and-forth) between the capsule lid and the two aluminium shoulders located behind the gelatin surround. At this stage in the simulation this secondary element may arguable no longer be a shock wave but a high amplitude pressure wave. At times exceeding t = 10 $\mu$s, the tensile wave from the rear of the aluminium flyer will continue to approach the incident shock, which has passed far beyond the tissue sample and continues to propagate within the backing material. Eventually, and long prior to reaching the rear surface of the gelatin backing, i.e. the gelatin-aluminium interface, the tensile wave catches the incident shock causing release within the capture system. At this point, a shock is no longer present within the capture system. However, residual stress waves may continue to reverberate within elements of the capsule.

Three gauge elements (nodal monitoring positions) were positioned within the model to measure shock pressure/stress: one at the front surface of the 5 mm aluminium cover (G1); and one at each of the front and rear tissue surfaces, respectively (G2 and G3). For comparative purposes a Vishay Micro-Measurements® & SR-4® type LM-SS-125-CH-048 manganin foil pressure gauge was used to measure the longitudinal pressure/stress at position G1 experimentally. Close agreement was apparent between both the experimental and simulated shock profiles in the aluminium cover (see Figure 8.13). Also, the rise times, Hugoniot stresses, and times of release for both the simulated and experimental results are all comparable. Both the front (G2) and rear (G3) gauge elements indicate a Hugoniot stress of ∼ 0.4 GPa in the
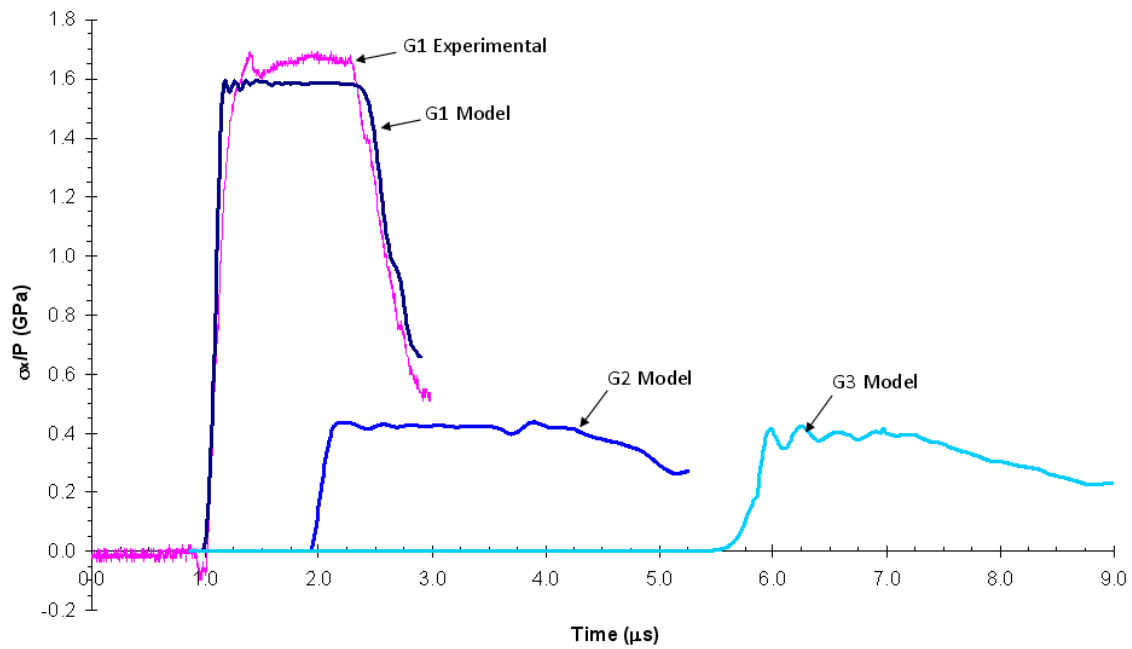
Figure 8.13: Hydrocode simulation of the soft-capture system - impacted at 216 m/s by a 10 mm Al flyer. Note: (G1) front surface of the 5 mm aluminium cover; (G2) front tissue surface; (G3) rear tissue surface

tissue. These gauges also show clearly resolved shock arrival times and near-constant Hugoniot stress states within the sample prior to release. Finally, the pulse duration of the shock at the front surface (G2) is longer than that measured at the rear of the sample (G3). This is due to release wave arrival from the rear of the flyer.

The modelled simulation of the soft-capture system provides a good indication of the nature of the loading experienced by the tissue sample. Further, given that the experimental gauge trace and numerical gauge trace within Figure 8.13 hold good agreement with one another, a reasonable level of confidence can be placed in the modelled stress-time history for the tissue sample. The ultimate goal of the soft-

204

capture system was to allow for post-shock recovery of skeletal muscle tissue following (quasi) one-dimensional loading. The system has been successful in achieving this goal. While not designed for such purpose, the exact stress imparted to the muscle tissue could be determined experimentally using the soft-capture system. However, this would most likely involve intrusive diagnostics and more complex, modified target design/manufacture. Due to time constraints, this was considered to be beyond the scope of this project.

## 8.4 Transmission Electron Microscopy Results

Transmission electron micrographs of a control and shocked sample of the middle-white tissue from a 223 m/s plate-impact experiment are shown in Figures 8.14 (a) and (b), respectively. The overall integrity of the structure present within the control sample is good, i.e. the major components comprising the structure of the sarcomere (see Section 5.1 for more details) are intact. However, evidence of myofibrillar splitting and areas of myofibrillar loss are apparent. The control sample was taken immediately before the 223 m/s shock recovery experiment. Tissue was excised from the same locus of muscle mass as the experimental sample.

Large scale disruption to the structure of the middle-white tissue can be seen following exposure to flyer-plate impact at 223 m/s (a shock pressure equivalent to approximately 0.45 GPa). The most significant change to the structure of the tissue is the damage caused to the I-band/Z-disk regions. Research into the effects of pressure upon skeletal muscle tissue by Fernandez et al. [89] and Zuckerman et al. [84], who examined the effects of both hydrostatic and hydrodynamic loading, respectively, has also shown similar site-specific damage to such material. This suggests that the I-Band/Z-Disk region is particularly prone to damage under pressurized conditions. Myofibres present within the shocked sample no longer appear to be spatially separate from one another - as was the case in the control tissue (see Figure 8.14(a)). Conversely, they more closely resemble a uniform mass of disrupted material.

Figure 8.14: (a) TEM micrograph of an un-impacted control longitudinal section through the middle-white tissue; (b) TEM micrograph of a longitudinal section through the middle-white tissue following impact at 223 m/s

Transmission electron micrographs of both a control and shocked sample of the commercially available tissue are shown in Figure 8.15. The micrograph of the shocked tissue corresponds to an experiment in which a 10 mm aluminium flyer impacted the soft-capture system at 216 m/s. In likeness with the shock-induced damage seen in the structure of the middle-white tissue (see Figure 8.14), the post-shocked sample of the commercially-available tissue clearly exhibits large scale disruption to its I-band/Z-disk regions. However, a widespread/global slip mechanism, which is not present in the shocked middle-white sample, is also predominant within the shocked structure of the commercially-available tissue. It is worth noting that the central regions of all sarcomeres present within the sample retain a high degree of directionality, i.e. remain aligned with one another. As such, it would seem that the slip mechanism seen in the tissue

was facilitated by the relative 'weakness' of the I-band/Z-disk region. While every effort was made to ensure that the sample's fibres were orientated parallel to the impact axis, it could not be guaranteed that all regions within the tissue's composition were aligned in such a manner, i.e. due to the natural anisotropic variance seen in the tissue (see Figure 5.7 in Section 5.1). As such, it is possible that the imaged section of the commercially-available tissue may correspond to: (a) a poorly aligned sample, or; (b) an area within the sample which, due to the anisotropic nature of the material, acted as a localized stress concentrator. This idea in itself is interesting, but will require rigorous and repeated testing before any form of conclusive statement may be formed.
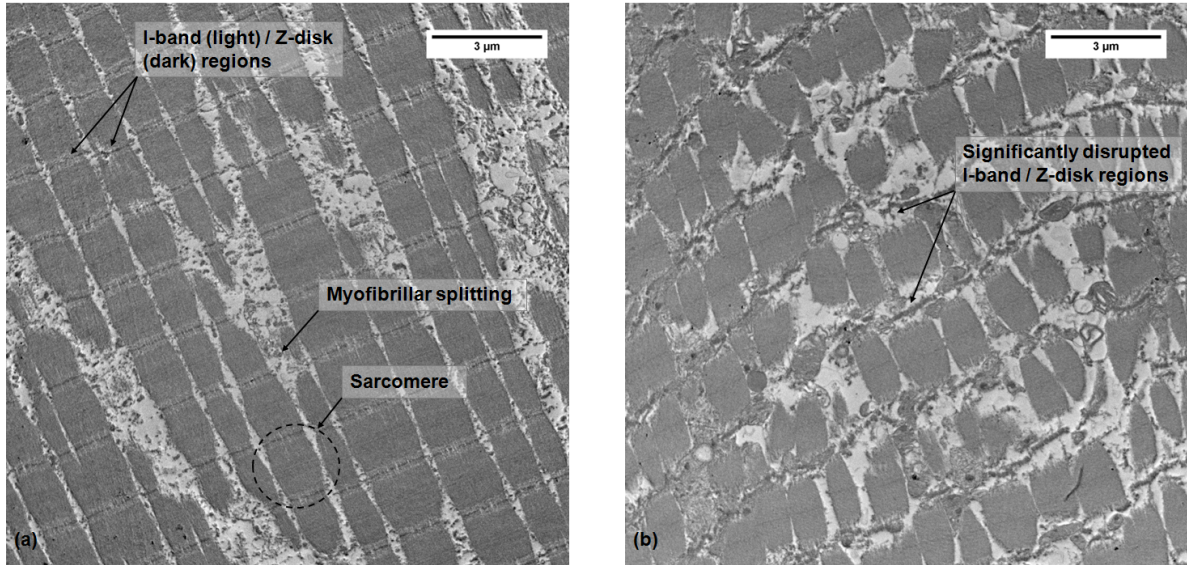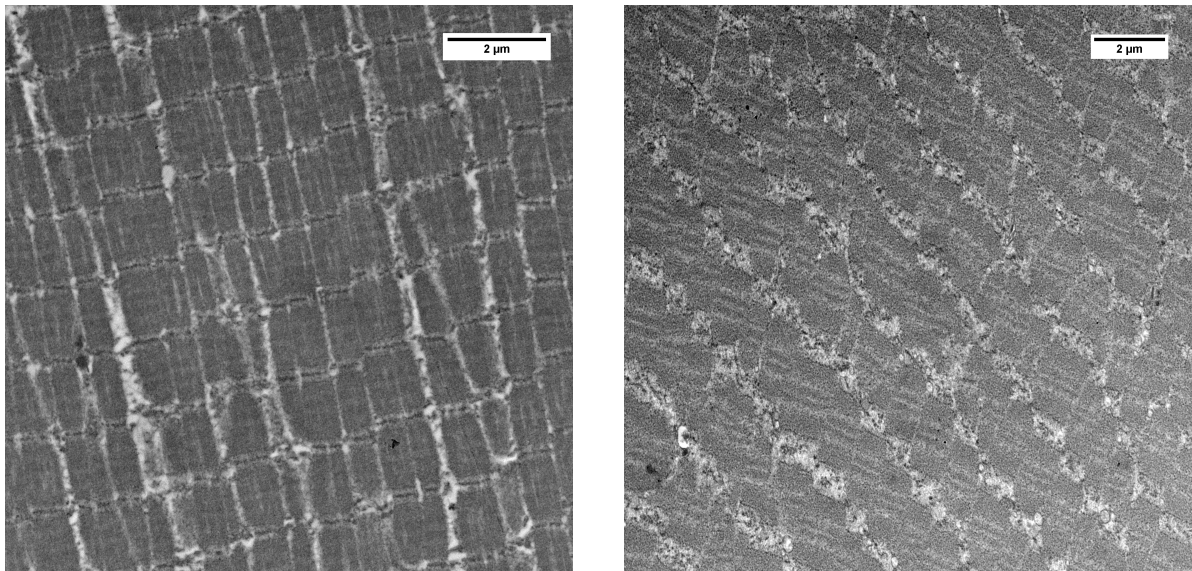


Figure 8.15: (a) TEM micrograph of an un-impacted control longitudinal section through the commercially-available tissue; (b) TEM micrograph of a longitudinal section through the commercially-available tissue following impact at 216 m/s

| Commercially-available | Control | Shocked | Alteration |
|:---:|:---:|:---:|:---:|
| *Myofibre width* ($\mu m$) | $0.71 \pm 0.07$ | $1.15 \pm 0.12$ | $\sim 60\,\%\ increase$ |
| *Sarcomere length* ($\mu m$) | $1.52 \pm 0.04$ | $1.97 \pm 0.08$ | $\sim 30\,\%\ increase$ |
| *Approx. sarcomere area* ($\mu m^2$) | $1.07 \pm 0.13$ | $2.27 \pm 0.33$ | $\sim 112\,\%\ increase$ |
| *Area of 5 sarcomeres* ($\mu m^2$) | $5.37 \pm 0.64$ | $11.35 \pm 1.67$ | $\sim 111\,\%\ increase$ |
| **Middle-White** | | | |
| *Myofibre width* ($\mu m$) | $1.30 \pm 0.50$ | $1.14 \pm 0.32$ | $\sim 19\,\%\ decrease$ |
| *Sarcomere length* ($\mu m$) | $1.813 \pm 0.08$ | $5.086 \pm 2.76$ | $\sim 180\,\%\ increase$ |
| *Approx. sarcomere area* ($\mu m^2$) | $2.357 \pm 1.00$ | $5.800 \pm 3.11$ | $\sim 146\,\%\ increase$ |
| *Area of 5 sarcomeres* ($\mu m^2$) | $11.79 \pm 4.99$ | $29.00 \pm 15.53$ | $\sim 146\,\%\ increase$ |

Table 8.5: Alteration to the commercially-available and middle-white tissue ultra-structure following shock compression to $\sim$0.4 GPa (216 and 223 m/s Al flyer impact, respectively)

Average sarcomere length and myofibre width were determined for the middle-white and commercially-available tissues both in their virgin state and following exposure to shock compression. Effort was made to account for the natural variability in size and shape seen within the tissue's structures during measurement. As such, the errors associated with the recorded values reflect this inherent variance (see Table 8.5). The errors recorded for each of the shocked tissues are somewhat larger than those for their corresponding control samples. This provides both an indication of the levels of damage caused to the tissues by the shock and the increased difficulty experienced when taking measurements from a micrograph exhibiting widespread structural damage.

Figures 8.16 and 8.17 are graphical distribution plots showing

changes in myofibrillar width and sarcomere length as a result of shock compression in the commercially-available and middle-white tissues, respectively. Both myofibre width and sarcomere length are seen to significantly increase within the commercially-available tissue. In the middle-white tissue, however, a slight reduction in myofibre width accompanies a significant increase in the overall length of sarcomeres present within the shocked sample.

Direct comparison of average sarcomere area within the shocked and control samples for each tissue type is shown in Figure 8.18. An increase in sarcomere area is seen to occur within both tissues as a result of shock compression. This is an unconventional material response. Poisson's ratio dictates that a material undergoing longitudinal compression will experience a component of lateral extension. The increase in average myofibrillar width seen to occur within the commercially-available tissue (lateral extension) suggests that this is maintained. What is unusual, however, is how sarcomere length has also increased in both the middle-white and commercially-available tissues, despite shock compression having acted along the axis of the muscle fibres/myofibres. Notably, not all materials conform to the standard definition of Poisson's ratio. Auxetic materials, for example, possess a negative Poisson's ratio and, unlike conventional materials, expand when they are stretched and contract when they are compressed. Examples of such materials include polyurethane foams, rocks, and highly-anisotropic composites [134]. In addition, both bone and skin have been predicted to exhibit auxetic behaviour [135]. The
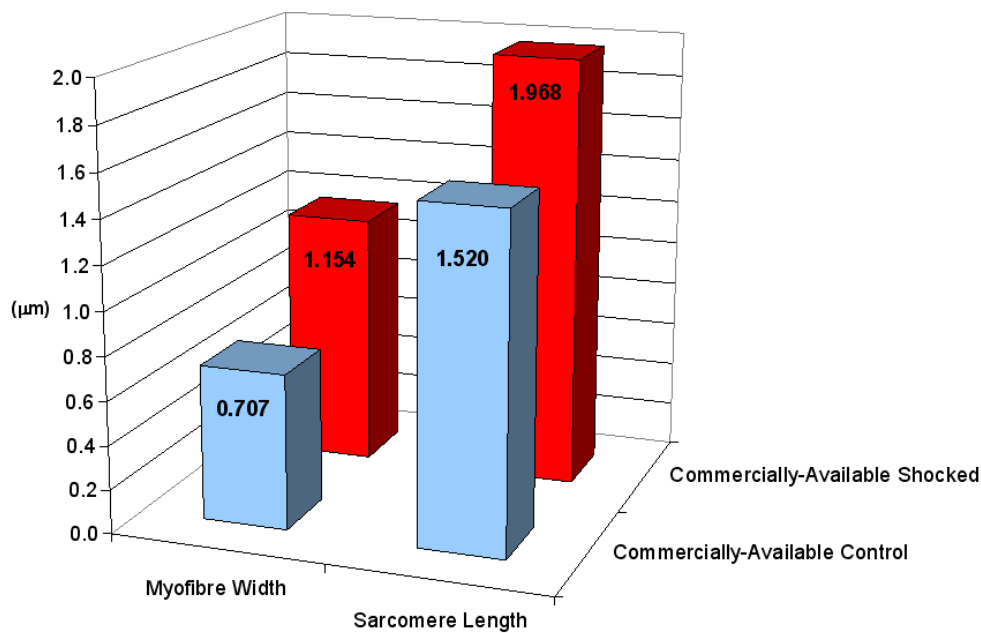
Figure 8.16: Alteration of the myofibrillar width and sarcomere length following shock compression of the commercially-available tissue at 216 m/s

idea that biological tissues could exhibit auxetic behaviour compliments the increased resistance to indentation exhibited by this class of material [136]. Specifically, this property is a clear benefit to otherwise weak material barriers such as skin and impact dampening tissues such as cartliage.

It has previously been noted (see Section 1.2) that a large percentage of muscle tissue comprises water/cellular fluid. Fluid is bound both within and around myofibres and the thick and thin filaments that comprise them. In addition, the sarcoplasmic reticulum acts as a membrane to myofibres at this level. Other membranes also exist and act to confine fluid within individual muscle fibres and fibre bundles (fascicles). It should be noted here that both the increase in
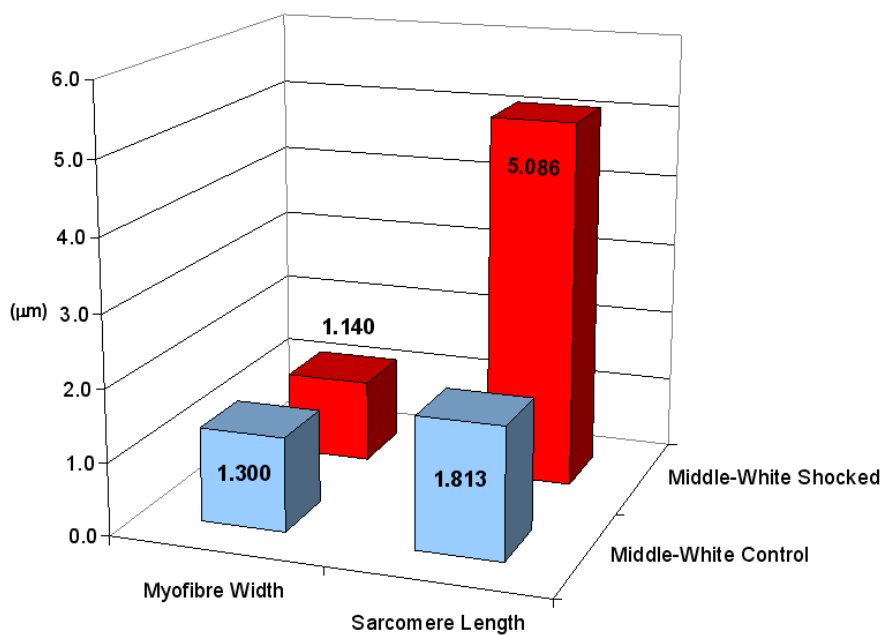
Figure 8.17: Alteration of the myofibrillar width and sarcomere length following shock compression of the middle-white tissue at 223 m/s
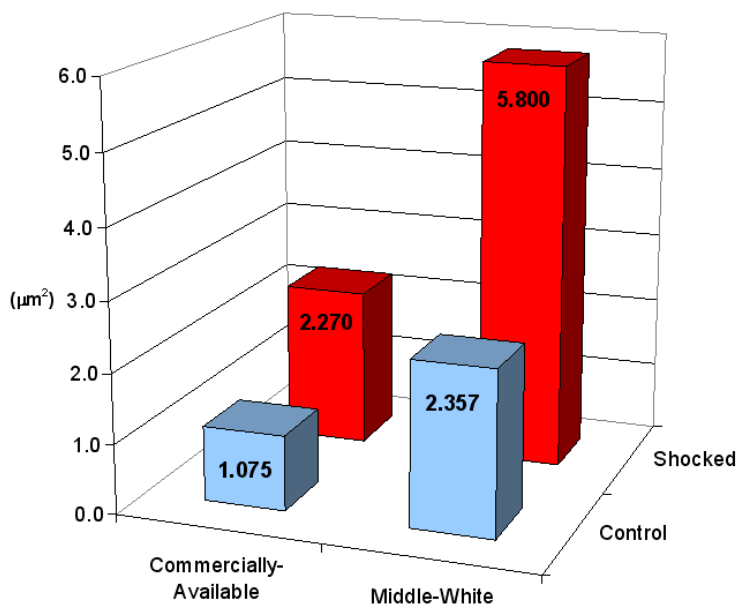


Figure 8.18: Changes to the overall area of sarcomeres present within the ultrastructure of the tested tissues due to shock compression to $\sim 0.4$ GPa

212

average sarcomere area and the damage witnessed within the tissues post-shock do not indicate the status of the material under a compressed state, but rather the combined effects of both shock-loading and release upon the tissue's structure. As such, discussion of the observed effects must bear relation to this particular loading regime and not just the compression wave.

Figure 8.19 shows three distinct phases within the loading profile. Ahead of the shock (1), tissue remains undisturbed and yet to experience any effects from loading. Behind the shock (2), material has been compressed by the wave and has reached equilibrium (Hugoniot stress). Here, it is likely that damage is caused to the I-band/Z-disk region, due to lesser material existing within this region than the A-band (thin filaments only). Damage to the cross-bridges, which connect thick and thin filaments together and act as the basic operator for the sliding filament model (i.e. muscle contraction) is also likely to occur as a result of compression. Damage to cross-bridge sites may have been facilitated by one of two possible mechanisms: (a) the rapid reduction of spacing between z-disks, thus exceeding the natural limits of the tissue, or; (b) excessive lateral expansion of myofibres into the pre-existing intermyofibrillar spacings (see Figures 8.14 (a) and 8.15 (a)). The extent of lateral flow, which might ultimately lead to the complete rupture of individual sarcomeres here, would have been controlled by the nature of the loading, i.e inertial confinement. Following shock loading, the compressed tissue is released by a tensile wave propagating from the rear of the impactor (flyer), leading to

213

phase (3). While it has been discussed that primary damage mechanisms may have taken place during compression, it seems reasonable to suggest that damage may have also been caused during release. The increase in sarcomere area during tensile attenuation (release) of the impact stress is indicative of an auxetic-like response, i.e. materials that expand laterally under tension. It is possible that the dynamic release of the material caused further damage to cross-bridges between the thick and thin filaments within the sarcomere (A-band), thus resulting in the permanently deformed state witnessed in Figure 8.14.

The shock speeds both predicted by the numerical simulation and calculated by the impedance matching technique were 2.07 and 2.08 mm/$\mu$s for the 216 and 223 m/s impact events, respectively. Further, the elastic wave speeds for the materials are 2.050 $\pm$0.100 mm/$\mu$s for the commercial tissue and 1.930 (+0.021; -0.025) mm/$\mu$s for the middle-white tissue. This suggests that, while imparting shock-like pressure upon sample tissue, the pressure wave resulting from the impact experiment involving the commercially-available tissue may not have been a discontinuity (i.e. a shock wave). Conversely, given the relatively low sound speed of the commercial tissue ($C_0 = 1.7$ mm/$\mu$s), a shock may have formed within the tissue, propagating at a velocity approximately equal to that of the elastic wave speed. It is reasonable to suggest, however, that the experiment involving the middle-white tissue would have resulted in the formation of a discontinuity, given that the calculated shock velocity exceeds that of the maximum elastic wave speed (1.951 mm/$\mu$s, determined experimentally). The forma-

tion of a shock within one experiment and not the other may provide some explanation as to why the levels of damage caused to the middle-white (shock) appear to exceed those within the commercially-available tissue. Conversely, this may reflect either: (a) a fundamental difference between the response of muscle tissue selected from two different sources and individual muscles, or; (b) that damage mechanisms imparted to skeletal muscle tissue as a consequence of shock loading are more complex than initially postulated. It is possible that some regions within the sample may exhibit greater disruption/damage than others, due to the anisotropic nature of the material. To this end, further experimentation involving the shock recovery of skeletal muscle is a recommended course of direction for future work (see Chapter 10).
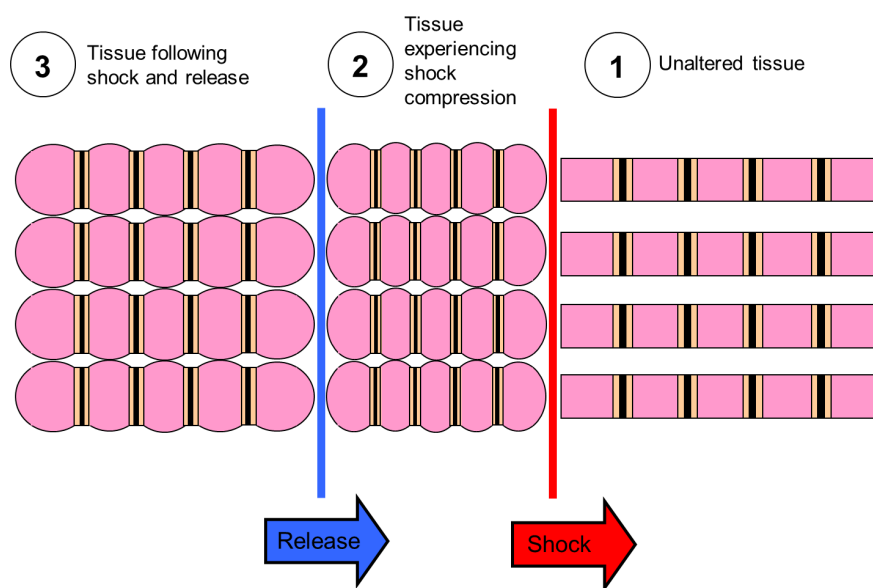
Figure 8.19: Schematic of the three distinct phases experienced by tissue samples during shock-recovery experiments [(1) Material ahead of the propagating wave remains unaltered; (2) Shocked; (3) Auxetic-like response to tensile release]

# Chapter 9

# Conclusions

A predominately linear equation-of-state has been formed for rendered porcine adipose tissue, taking the form $U_s = 1.58 + 2.47u_p$. The equations-of-state for 20 wt.% ballistic gelatin and water, which are both roughly equivalent within the principal Hugoniot plane, are dissimilar to the response of the rendered adipose tissue investigated in this study. Markedly higher shock velocities are seen to result within the adipose tissue than either the gelatin or water at shock states corresponding to particle velocities in excess of $\sim 0.35$ mm/$\mu$s. Notably, the datapoint corresponding to the lowest impact velocity for the adipose material has suggested slight curvature in its otherwise linear $U_s$-$u_p$ Hugoniot at low particle velocities. This behaviour has been seen elsewhere in polymeric materials and is discussed in greater detail within Section 8. Curvature of the Hugoniot for the adipose material at particle velocities less than $\sim 0.35$ mm/$\mu$s again highlights dissimilarity between its response and that of both 20 wt.% ballistic gelatin and water to the shock. Specifically, these materials both appear to possess entirely linear relationships.

When presented within the pressure-particle velocity and pressure-volume Hugoniot planes, the experimental data for the adipose tissue shows that the material exhibits a significantly different response to shock than either water or ballistic gelatin. Again, these materials exhibit near identical response in both the pressure-particle velocity and pressure-volume planes. While the response of both gelatin and water has been shown to be hydrodynamic in nature, i.e. each exhibiting fluid-like behaviour, the adipose material has been shown to strengthen under identical loading conditions. This apparent strengthening has been attributed to the structural similarity that exists between both the adipose tissue and polymers: a class of material also exhibiting this type of behaviour during shock compression. In particular, this type of response is believed to be the result of increased resistance to compression due to the presence of large side-groups on the carbon backbone chains, which comprise the core of the polymeric structure of the material - a phenomenon known as steric hindrance.

Lateral stress measurements within the adipose tissue were also undertaken. When combined with longitudinal EoS data, this allowed calculation of material shear strength. A reduction in lateral stress (e.g. a negative gradient) was observed within the adipose material as the shock swept past the gauge, suggesting an increase in the shear strength of the material behind the shock. Further, the rate of change in shear strength behind the shock within the tissue was seen to significantly increase between 1 and 2 GPa. Such behaviour lies in agreement with the change in response observed for the tissue in

the P-u$_p$ plane, i.e. datapoints within this region (1 - 2 GPa) were seen to shift above the hydrodynamic response curve. In addition, this behaviour has also been detected elsewhere within ballistic soap at similar pressures. It is unclear whether a significant increase in the rate of change in shear strength between 1 and 2 GPa is linked to polymeric materials in general. However, it seems reasonable to suggest that the response detected for both the adipose material and ballistic soap (each possessing polymeric structures) over this pressure range may relate to a specific structural alteration. One possible explanation for the noted change in response, which has been suggested in the literature, may be the reduction in spacing between carbon backbone atoms. It seems reasonable that this change would follow initial compression of: (i) the spacings between molecules (van der Waals interactions), and: (ii) the polymer side chains. These initial stages of compression would most likely occur at lower shock pressures and, as such, are a probable cause of curvature within the Hugoniots for polymeric materials at low particle velocities.

Using similar methods to those adpoted for the adipose material, the shock response of porcine skeletal muscle from two separate sources was investigated. Significantly, a difference in response between tissue of either middle-white (fresh) or commercially-available (consumer processed) origin was not detected. This has allowed for the formation of a generalized equation-of-state for skeletal muscle at particle velocities up to 1 mm/$\mu$s. Despite (a) the relatively high water content of

the tissues, and (b) the similarity in gradient that has been shown to exist between the equations-of-state for both water and skeletal muscle in the $U_s$-$u_p$ plane, the data obtained via plate-impact experiment here suggests that the fibrous component of the tissue provides a channel for increased velocity of shock propagation. In likeness with the rendered adipose tissue, skeletal muscle tissue has also exhibited strength during shock compression in this study. Again, such behaviour was indicated by measured data points lying above the predicted hydrodynamic response curve in the pressure-volume Hugoniot. However, the mechanism behind material strength observed within the adipose tissue and skeletal muscle is arguably dissimilar. Whereas the adipose material was shown to exhibit increased strength (resistance to compression) with impact stress, the data for the skeletal muscle suggests that it exhibits a constant flow strength which is independent of the range of impact conditions examined here. An exponential fit was plotted through the data for the skeletal muscle tissue in the pressure-volume Hugoniot. It is unknown whether this exponential relationship and the difference between predicted and measured response remains at lower shock pressures than those investigated here. However, it seems reasonable that application of a suitable strength coefficient to the linear (EoS) shock model for skeletal muscle may provide greater accuracy to future numerical shock wave simulations, e.g. modelling shock interactions within the body.

The shock behaviour of the rendered adipose material and the muscle tissues examined in this work both differ markedly from the hydro-

dynamic response of 20 wt.% ballistic gelatin, which is commonly used as a tissue simulant in high strain-rate studies. An investigation into the shock response of a homogenized variant of skeletal muscle was also conducted in this study. The response of the homogenized variant which, as a result of processing, lacked any structural resemblance to the natural state of skeletal muscle, was shown to collapse back onto the hydrodynamic response curve predicted for skeletal muscle. As such, the the strength/resistance to shock compression observed within the unaltered skeletal muscle tissue seems to be strongly linked to its fibrous structure.

It seems reasonable to suggest that the equation-of-state data generated in this work may be incorporated into numerical simulations seeking to model shock interactions within the human body. This may, for example, allow for a deeper understanding of the processes occurring within the lower limbs of both the mounted and unmounted soldier as a result of exposure to blast from improvised explosive devices (IEDs). The development of new mitigation solutions to combat the types of injury associated with such interactions may also be possible using a simulated approach. It is worth noting that the information/data presented in this thesis provides a starting point for the development of improved high strain-rate/shock models for both fatty and muscular tissues. Consequently, additional data will be required in order to both build upon the information presented in this work and to gain a more comprehensive understanding of the types of damage and tissue response expected from blast interactions. Such

information/data will likely include the addition of strength and failure models to the respective tissue types. For example, data on the dynamic tensile strength (spall behaviour) of skeletal muscle and/or hardening and softening coefficients for each soft tissue may be incorporated to suit a range of impact conditions/loading regimes. In order to determine these strain-rate dependent parameters it seems likely that a broader range of experiments than those presented in this study will be required. Specifically, experiments involving the study of 'weaker' shocks within soft tissues will likely be required.

Notably, a broad range of loading conditions may be expected within the blast environment (e.g. direct exposure, exposure despite vehicular protection, physical injury resulting from momentum transfer, etc.). As such, it seems reasonable to suggest that tissue response over a wider range of strain-rates than those afforded by shock interaction alone will also be required in order to improve current modelling capability. Only a broad-ranging study of this type will allow for accurate characterization of the highly strain-rate dependent response of soft tissues and for improvement of the current levels of protection afforded by the individual. It seems likely that a variety of techniques - including Split-Hopkinson Pressure Bar (SHPB), shock tube, and gas gun - will also be required.

A soft-capture system allowing for the shock-recovery of skeletal muscle tissue in conjunction with the plate-impact technique has been developed. While used solely for the recovery of skeletal muscle in this

study, it seems reasonable to suggest that the capsule may also allow for the soft-capture of other biological tissues of similar density (e.g. heart, lung, liver, kidney tissue, etc.). In addition, the shock-recovery of biological cell suspensions may also be possible using the developed soft-capture system. Development of the system has been aided via numerical simulation of flyer-plate impact upon various capsule designs and investigation of the wave profile imparted to the sample by the resultant shock wave interactions. These simulations have made use of the equation-of-state data obtained for both skeletal muscle tissue in this work and for ballistic gelatin, whose EoS was established elsewhere. Following development of the system, an initial study into the response of skeletal muscle to one-dimensional shock compression was performed. This involved the recovery of tissue samples from two soft-capture experiments in which fibre alignment was predominately parallel to the impact axis (i.e. fibres were aligned 'head-on'). Shock-recovery of both a middle-white and commercially-available tissue sample was undertaken. Recovered samples were imaged by transmission electron microscope (TEM) and the resultant damage was assessed. An auxetic-like response was observed in each of the recovered tissue types, i.e. the overall size of sarcomeres (the functional unit responsible for muscle contraction) was markedly increased in the shocked samples. Similar results have been seen elsewhere in studies involving hydrostatic pressurization of skeletal muscle. In addition to the auxetic-like response observed in both tissue types, disruption of the I-band/Z-disk regions within the tissues was also observed. How-

ever, this type of damage was more pronounced in the middle-white tissue. Finally, a slip mechanism was identified within the recovered commercially-available sample. It seems reasonable that this mechanism was facilitated by a combinamtion of: (a) inaccurate sample fibre alignment (i.e. not parallel to the impact axis) within the imaged region, and, (b) weakening of the tissue at the damaged I-band/Z-disk regions. It is possible that the auxetic-like response observed in the shocked muscle tissues may also be prevalent at lower magnitudes of shock pressure than those examined in this study. However, the point at which this response is not observed is unknown.

In terms of the physical injury associated with the propagation of 'weaker' shock waves within skeletal muscle, it seems reasonable to suggest that the expansion of myofibres (i.e. auxetic-like behaviour) would result in both interstitial bleeding and bruising/swelling of the muscle. However, the types of debilitating injury seen to result from exposure to land-mine blast, i.e. high shock pressure, are ultimately the response of tearing or complete rupture of the muscle.

To summarize, this project has achieved its main aims of: (i) obtaining shock data for both porcine adipose and skeletal muscle tissues, and; (ii) developing a soft-capture system allowing for the shock-recovery of skeletal muscle. Key findings include:

1. The derivation of equations-of-state for both porcine skeletal muscle and rendered porcine adipose tissue, taking the form $U_s = 1.72 + 1.88u_p$ and $U_s = 1.58 + 2.47u_p$, respectively. Further,

a non-linear response was apparent within the adipose tissue at lower particle velocities, suggesting a polynomial equation-of-state within this region.

2. The detection of non-hydrodynamic behaviour within each of the tissue types (i.e. adipose/skeletal) over the range of investigated impact conditions. While the rendered adipose tissue was seen to strengthen/exhibit increased resistance to compression with impact stress, the muscle tissues exhibited an apparent flow strength that was independent of the range of investigated shock pressures. These observed behaviours lie in direct contrast with the hydrodynamic shock response of ballistic gelatin, which was established elsewhere.

3. A regression to hydrodynamic behaviour within a homogenized variant of skeletal muscle, suggesting that it is the anisotropic, fibrous structure of the tissue that is responsible for the observed material strength (see previous Point 2).

4. The detection of an overall increase in shear strength with impact stress within the adipose tissue. In addition, an increase in the relative change between the initial and final shear strength states within the tissue was seen to result at impact stresses ranging from 1 to 2 GPa. This behaviour has also been seen to occur within ballistic soap (investigated elsewhere). It seems likely that future investigations will seek to determine whether this response is applicable to either polymers in general or only polymeric simu-

lants/gels (e.g. ballistic soap, rendered adipose tissue, physically associating gels (PAGs)).

5. The observation of damage to I-band/Z-disk regions within shocked skeletal muscle and an overall auxetic-like response to the loading profile. This auxetic-like response has been seen in hydrostatic pressurization studies on skeletal muscle elsewhere and has been attributed to increased meat toughness. As such, it seems likely that the observed structural damage may relate to the constant flow strength apparent within the pressure-volume Hugoniot for skeletal muscle (see Figure 8.9).

# Chapter 10

# Recommendations for Further Work

### 10.0.1 Adipose Tissues

Two adipose materials immediately present themselves for future shock-related research. These are: (a) un-rendered fat, i.e. the visceral fat deposits found surrounding the body's vital organs, and; (b) the human calcaneal fat pad, which is found at the base of the heel. This study has focused upon the shock response of rendered porcine adipose tissue. As such, future research may seek to establish whether or not the rendering process has a significant effect upon response of fatty tissues to shock. It seems reasonable that this could be established by examining the shock response an un-rendered fatty tissue using plate-impact methods in conjunction with both longitudinal and lateral manganin foil pressure gauges. It is postulated that the increase in shear strength with impact velocity observed within the rendered material in this study will be amplified within the shock data for un-rendered tissue. However, such assumption is speculative and provides

initial purpose to the proposed research. Future work may also wish to examine the shock response of both rendered and non-rendered adipose tissues at lower particle velocities than those examined in this body of work. This may allow for detailed assessment of: (i) the extent of curvature of the ($U_s$-$u_p$) Hugoniot at lower particle velocities for the rendered tissue, and; (ii) whether this behaviour is also observed within non-rendered adipose tissues, i.e. visceral deposits. Notably, manganin foil gauges have a limited working range, i.e. they do not function well at low shock pressures. Thus, in order to examine the behaviour of adipose tissues at lower impact stresses and particle velocities than those examined here, a diagnostic capable of higher resolution than manganin foil gauges will be required. Optical methods, such as VISAR or heterodyne velocimetery, may provide a suitable solution to this requirement. Alternatively, carbon gauges, which are better suited to lower pressures than manganin foil gauges, may be employed.

The human calcaneal fat pad and its response to high amplitude pressure/shock waves also provides an interesting avenue for future research. As the first point-of-contact following transmission of a shock/blast wave through the sole of a protective item of footwear, understanding the high strain-rate behaviour of the calcaneal pad is vital. It seems reasonable that the response of calcaneal fat at the rates of strain synonymous with direct exposure to IED-induced shock waves or shock transmission through the hull of a vehicle are of paramount importance. In order to understand the response of this

material at such rates, both Split-Hopkinson Pressure Bar (SHPB) and low-end plate impact/gas gun experiments may be of particular use. Notably, the shock pressures encountered during exposure to IED-related threats may vastly exceed the impact-mitigating properties of the human heel. However, understanding the influence of the calcaneal fat pad upon the shock as it enters the lower limbs is undoubtedly an aspect that requires consideration when tasked with accurately simulating exposure to shock/blast using material models. By examining the response of calcaneal fat at low shock pressures, it seems reasonable that a polynomial shock equation-of-state may be formed for the tissue (i.e. curvature seen at low particle velocities). This would provide a greater degree of accuracy than, say, the linear relationship established for the rendered adipose tissue examined here. Further, SHPB testing may allow for the addition of complimentary strain hardening coefficients.

### 10.0.2  Skeletal Muscle Tissue

The equation-of-state data presented for skeletal muscle tissue in this study relates to a bulk tissue response. However, the relatively high shock pressures induced within tissue samples by the plate impact methods used here appear to have exceeded the limit at which a perceptible difference in fibre alignment has an effect upon the shock. The effect of fibre alignment upon planar shock propagation within skeletal muscle is, however, an area of focus yet to appear within the

scientific literature. Notably, the effects of anisotropy are most likely only detectable at lower particle velocities and corresponding shock pressures than those examined in this work - although it does seem reasonable that the plate-impact technique may provide a platform on which the effects of the tissue's anisotropic structure upon planar shock may be determined. A study of this nature would require: (i) thin sections of muscle tissue; (ii) the utmost care in achieving accurate fibre alignment during experimental testing; (iii) the use of materials of low shock impedance in both flyer and cover-plate construction, and; (iv) a diagnostic method capable of resolving lower pressure states than those examined by manganin foil pressure gauges here. While fibre alignment would be an obvious concern during the proposed type of experiment, it is likely that thin sections of tissue would also be required in order to maintain a steady shock within samples. In addition, the use of lower impedance flyer/cover materials would ensure the generation of lower impact stresses than those investigated in this work. However, and as discussed, this would also promote the requirement for a diagnostic capable of resolving lower pressure states than manganin foil pressure gauges.

In addition to the effects of tissue anisotropy on shock propagation, it would also be interesting to investigate the change in shear strength within skeletal muscle over a range of higher shock pressures. Lateral shock data for numerous other materials including ballistic soap, the adipose material examined in this study, and various polymeric materials may be found within the literature. As such, it would be of

particular interest to note any similarities or differences between this data and the proposed dataset for skeletal muscle.

Due to the natural impedance mis-match that exists between the body's soft tissues and the skeletal frame, shock interaction within limbs typically involves shock reflection and the evolution of tensile forces from regions in which shear wave motion is generated. As such, the dynamic tensile strength of skeletal muscle tissue is an area of future interest. It is worth noting that spallation (i.e. dynamic tensile failure) is believed to be a major damage mechanism contributing to blast injury [137, 138]. In addition, gas gun systems have been widely employed as a means to examine the dynamic tensile behaviour, i.e. spall strength, of various metallic and polymeric materials. While clearly possessing a significantly lower tensile strength, and thus spall strength, than these materials, it seems reasonable to suggest that the dynamic tensile behaviour of a soft material such as skeletal muscle may be investigated using the plate-impact technique. However, as with the proposed investigations seeking to assess the effects of tissue anisotropy upon planar shock waves, investigation of the dynamic tensile strength of muscle will undoubtedly involve much lower shock pressures and impact velocities than those encountered in this research study. Consequently, the effect of the tissue anisotropy may influence spall strength.

By selecting a flyer of appropriate thickness to the impact velocity in a plate-impact experiment, it is possible to generate a spall plane within the sample material. This spall plane is generated around a

231

specific location within a sample material where the tensile release from the rear of the flyer overlaps the tensile release from the rear of the sample. In order to specify this location, the equation-of-state of both the flyer and sample material must be known. As such, the equation-of-state generated for skeletal muscle here may be of benefit to the proposed investigation of spall strength. It is worth noting that static tests have confirmed heterodyne velocimetry as a potential diagnostic for investigation of the dynamic tensile behaviour of skeletal muscle. These static tests involved the detection of a signal from the rear surface of a tissue sample when coated with a reflective silver pigment. In addition, dynamic testing involving spallation of a PMMA block with a rear surface coating of the reflective pigment also resulted in data collection.

### 10.0.3   Shock-Recovery

The design and development of a soft-capture system allowing for one-dimensional shock-recovery of skeletal muscle tissue in conjunction with the plate-impact technique has been detailed. In addition, analysis of recovered tissue from two shock recovery experiments - one involving middle-white tissue and another involving commercially-available tissue - has been conducted via transmission electron microscope. In order to begin to more deeply assess the effects of planar shock upon skeletal muscle tissue, it will be necessary to conduct both repeat experiments of those presented in this work and to examine a

broader range of impact conditions. In addition, the effect of fibre alignment upon the types of damage witnessed within the material will be of future interest. Another possible avenue for research using the developed soft-capture system may involve assessment of the level of damage witnessed within samples with respect to the shock pulse duration (e.g. is lesser or greater damage observed with reduced or extended shock pulse duration, or is the observed damage simply a result of peak Hugoniot stress?). Finally, one of the damage mechanisms observed within the shocked tissue samples in this work (increased sarcomere size) has been related to increased meat toughness within the food science literature. As such, it would be interesting to perform quasi-static (low-rate) compression tests upon both un-shocked and shock-recovered tissue. This would allow for the generation of stress-strain curves for the respective tissue types and may allow for the extent of any strain hardening imparted to sample tissue by the shock may be quantified. Such information could then be used to achieve a greater degree of accuracy in simulations, i.e. hardening coefficients may begin to be implemented.

## Publications

A number of publications have been achieved during the course of this doctoral research programme. Journal and conference proceedings publications which have been attained during the construction of this body of work include:

- J.M. Wilgeroth, P.J. Hazell, G.J. Appleby-Thomas, The Shock Response of a Rendered Porcine Fat, Journal of Applied Physics, 2010, 108 (9), art no. 093527

- J.M. Wilgeroth, P.J. Hazell, G.J. Appleby-Thomas, On the behaviour of porcine skeletal muscle under shock compression, International Journal of Impact Engineering, article in press, available online 5 August 2012, http://dx.doi.org/10.1016/j.ijimpeng.2012.07.008

- J.M. Wilgeroth, P.J. Hazell, G.J. Appleby-Thomas, The dynamic response and shock-recovery of porcine skeletal muscle tissue, AIP Conference Proceedings, 2012, 1426. pp.139-142

Additional journal publications which have either: (a) used data from the above journal papers, or; (b) the author of this thesis, James Wilgeroth, has has direct involvement with include:

- G.J. Appleby-Thomas, P.J. Hazell, D.C. Wood, J.M. Wilgeroth, J.A. Leighs, On the effects of lateral gauge misalignment in

shocked targets, Review of Scientific Instruments, 2012, 83 (6), art no. 063904

- C.J. Shepherd, G.J. Appleby-Thomas, J.M. Wilgeroth, P.J. Hazell, D.F. Allsop, On the response of ballistic soap to one-dimensional shock loading, International Journal of Impact Engineering, 2011, 38 (12), pp. 981-988

- G.J. Appleby-Thomas, P.J. Hazell, J.M. Wilgeroth, C.J. Shepherd, D.C. Wood, A. Roberts, On the dynamic behaviour of three readily available soft tissue simulants, Journal of Applied Physics, 2011, 109 (8), art no. 093527

- G.J. Appleby-Thomas, P.J. Hazell, J.M. Wilgeroth, D.C. Wood, On the interpretation of lateral manganin stress measurements in polymers, Journal of Applied Physics, 2010, 108 (3), art no. 033524

# Bibliography

[1] R. R. Seeley, T. D. Stephens, and P. Tate. *Anatomy and Physiology - Fourth Edition*. Number ISBN 0-697-41107-9. WCB McGraw-Hill, Boston, 1998.

[2] A.J. Gaudin and K.C. Jones. *Human Anatomy and Physiology*. Number ISBN: 0-15-539705-2. Harcourt Brace Jovanovich, 1989.

[3] H. E. Huxley. The ultra-structure of striated muscle. *British medical bulletin*, 12(3):171–173, 1956.

[4] H.E. Huxley and J. Hanson. The structural basis of the contraction mechanism in striated muscle. *Annals of the New York Academy of Sciences*, 81:403–408, 1959.

[5] H.E. Huxley. The mechanism of muscular contraction. *Scientific American*, 213(6):18–27, 1965.

[6] J. H. McElhaney. Dynamic response of bone and muscle tissue. *Journal of applied physiology*, 21(4):1231–1236, 1966.

[7] H. Saraf, K. T. Ramesh, A. M. Lennon, A. C. Merkle, and J. C. Roberts. Mechanical properties of soft human tissues under dynamic loading. *Journal of Biomechanics*, 40(9):1960–1967, 2007.

[8] B. Song, W. Chen, Y. Ge, and T. Weerasooriya. Dynamic and quasi-static compressive response of porcine muscle. *Journal of Biomechanics*, 40(13):2999–3005, 2007.

[9] P. Moy, T. Weerasooriya, T. F. Juliano, M. R. VanLandingham, and W. Chen. Dynamic response of an alternative tissue simulant, physically associating gels (pag). *SEM Annual Conference on Experimental Mechanics, June 5 - 7, 2006, St. Louis, Missouri*, pages 304–310, 2006.

[10] M. Van Loocke, C. G. Lyons, and C. K. Simms. Viscoelastic properties of passive skeletal muscle in compression: Stress-relaxation behaviour and constitutive modelling. *Journal of Biomechanics*, 41(7):1555–1566, 2008.

[11] D.A. Morrow, T.L. Haut Donahue, G.M. Odegard, and K.R. Kaufman. Transversely isotropic tensile material properties of skeletal muscle tissue. *Journal of the Mechanical Behavior of Biomedical Materials*, 3(1):124–129, 2010.

[12] B. R. Mackenna and R. Callander. Illustrated physiology - fifth edition. *Longman Group HK Limited, Edinburgh. ISBN 10: 0443040958 / ISBN 13: 9780443040955*, page 266, 1997.

[13] T. Nishioka and M. Irie. Evaluation method for firmness and stickiness of porcine perirenal fat. *Meat Science*, 70(2):399–404, 2005.

[14] Janice E. Miller-Young, Neil A. Duncan, and Gamal Baroud. Material properties of the human calcaneal fat pad in compression: experiment and theory. *Journal of Biomechanics*, 35(12):1523 – 1531, 2002.

[15] J. C. F. Millett and N. K. Bourne. The shock induced equation of state of three simple polymers. *Journal of Physics D: Applied Physics*, 37(20):2901–2907, 2004.

[16] W. J. Carter, S. P. Marsh, and R. G. McQueen. Hugoniot equation of state of polymers. *Los Alamos National Laboratory, Report*, LA-13006-MS, 1995.

[17] J. Kwon and G. Subhash. Compressive strain rate sensitivity of ballistic gelatin. *Journal of Biomechanics*, 43(3):420–425, 2010.

[18] T. Baumberger, C. Caroli, and D. Martina. Fracture of a biopolymer gel as a viscoplastic disentanglement process. *European Physical Journal E*, 21(1):81–89, 2006.

[19] H. Furukawa, R. Kuwabara, Y. Tanaka, T. Kurokawa, Y.-H. Na, Y. Osada, and J.P. Gong. Tear velocity dependence of high-strength double network gels in comparison with fast and slow relaxation modes observed by scanning microscopic light scattering. *Macromolecules*, 41(19):7173–7178, 2008.

[20] A.A. Catherall, J.R. Melrose, and R.C. Ball. Shear thickening and order-disorder effects in concentrated colloids at high shear rates. *Journal of Rheology*, 44(1):1–25, 2000.

[21] C. P. Salisbury and D. S. Cronin. Mechanical properties of ballistic gelatin at high deformation rates. *Experimental Mechanics*, pages 1–12, 2008.

[22] Caillou J.P., Dannawi M., Dubar L., and Wielgosz C. Dynamic behaviour of a gelatine 20 *Proceedings of the Personal Armour System Symposium*, pages pp 325–331, 1994.

[23] H. D. Young. University physics - eighth edition. *Addison-Wesley, ISBN 10: 0201196514*, 1991.

[24] I. I. Glass. Shock waves on earth and in space. *Progress in Aerospace Sciences*, 17(C):269–286, 1976.

[25] M. A. Meyers. Dynamic behaviour of materials. *John Wiley and Sons Inc., New York. ISBN: 0-471-58262*, 1994.

[26] W. M. Isbell. *Shock Waves - Measuring the Dynamic Response of Materials*. Number ISBN 1-86094-471-X. Imperial College Press, 2005.

[27] S. Eliezer, A. Ghatak, and H. Hora. *Fundamentals of Equation of State.* World Scientific Publishing Co. Pte. Ltd. ISBN: 981-02-4833-4, 2002.

[28] John D. Anderson. *Modern compressible flow : with historical perspective.* McGraw-Hill, New York, 1990. Legacy Ctl. No.: G01237273; British Library A 91/00602 DSC01.

[29] I. C. Skidmore. An introduction to shock waves in solids. *Atomic Weapons Research Establishment, Aldermaston, Berks., U.K. Applied Materials Research*, pages pp.131 – pp.147, 1965.

[30] R. Courant and O. Friedrichs. Supersonic flow and shock waves. *ISBN-10: 0387902325 (Vol. 21)*, Volume 1, 1999.

[31] G. J. Appleby-Thomas, P. J. Hazell, C. Stennet, and G. Cooper. The dynamic behaviour of a modified polyurethane resin. *9th International Conference on the Mechanical and Physical Behaviour of Materials Under Dynamic Loading*, 2:1081, September 7-11, 2009 2009.

[32] J. C. F. Millett, N. K. Bourne, and J. Akhavan. The response of hydroxy-terminated polybutadiene to one-dimensional shock loading. *Journal of Applied Physics*, 95(9):4722–4727, 2004.

[33] G. J. Appleby-Thomas, P. J. Hazell, C. Stennett, G. Cooper, K. Helaar, and A. M. Diederen. Shock propagation in a cemented tungsten carbide. *Journal of Applied Physics*, 105(6), 2009.

[34] J.C.F. Millett, N.K. Bourne, and D.P. Dandekar. Lateral stress measurements and shear strength in shock loaded tungsten carbide. *Journal of Applied Physics*, 96(7):3727–3732, 2004.

[35] Dennis Grady. Impact failure and fragmentation properties of tungsten carbide. *International Journal of Impact Engineering*, 23(1, Part 1):307 – 317, 1999.

[36] S. P. Marsh. *LASL Shock Hugoniot Data.* University of California Press, Los Angeles, CA, 1980.

[37] D. P. Dandekar. Spall strength of tungsten carbide. *Report No. ARL-TR-3335. Available online at http://www.dtic.mil/cgi-bin/GetTRDoc?AD=ADA427318 on 10/09/12.*, 2004.

[38] D. E. Grady. Shock profile studies on selected silicon carbide ceramics with application to dynamic yield mechanisms. *AIP Conference Proceedings - Shock Compression of Condensed Matter - 1999*, pages 629 – 632, Copyright 2000.

[39] S. Hayun, M.P. Dariel, N. Frage, and E. Zaretsky. The high-strain-rate dynamic response of boron carbide-based composites: The effect of microstructure. *Acta Materialia*, 58(5):1721–1731, 2010.

[40] D.E. Grady. Shock-wave compression of brittle solids. *Mechanics of Materials*, 29(3-4):181–203, 1998.

[41] P.L. Hereil, S. Bonnan, and F. Collombet. Experimental characterization of shock wave behaviour of porous aluminium. *J.PHYS IV FRANCE 7 (1997)*, Colloque C3, Supplement au Journal de Physique III d'aout 1997, 1997.

[42] J. E. Field, S. M. Walley, W. G. Proud, H. T. Goldrein, and C. R. Siviour. Review of experimental techniques for high rate deformation and shock studies. *International Journal of Impact Engineering*, 30(7):725 – 775, 2004. Fifth International Symposium on Impact Engineering.

[43] N.K. Bourne. A 50 mm bore gas gun for dynamic loading of materials and structures. *Measurement Science and Technology*, 14(3):273, 2003.

[44] P. J. Hazell, C. Stennett, and G. Cooper. The shock and release behavior of an aerospace-grade cured aromatic amine epoxy resin. *Polymer Composites*, 29(10):1106–1110, 2008.

[45] T.J. Ahrens. Shock wave techniques for geophysics and planetary physics. *Methods in Experimental Physics*, 24(PART A):185–235, 1987.

[46] A.B. Wenzel. A review of explosive accelerators for hypervelocity impact. *International Journal of Impact Engineering*, 5(1-4):681–692, 1987.

[47] M.W. Greenaway, W.G. Proud, J.E. Field, and S.G. Goveas. A laser-accelerated flyer system. *International Journal of Impact Engineering*, 29(1-10):317–321, 2003.

[48] L.M. Barker and R.E. Hollenbach. Laser interferometer for measuring high velocities of any reflecting surface. *Journal of Applied Physics*, 43(11):4669–4675, 1972.

[49] N.R. Routley, E. Price, P.T. Keightley, J.C.F. Millett, N.K. Bourne, and G.T. Brown, E.N. abd Gray III. An investigation of surface velocimetry of shocked polyethylene using hetv. volume 955, pages 1131–1134, 2007.

[50] J.C.F. Millett and N.K. Bourne. Development of magnetic gauges for the measurement of particle velocities during one-dimentional shock loading. *Measurement Science and Technology*, 14(5):601–606, 2003.

[51] C. Stennett, G.A. Cooper, P.J. Hazell, and G. Appleby-Thomas. Initiation of secondary explosives measured using embedded electromagnetic gauges. volume 1195, pages 267–270, 2009.

[52] J.M. Walsh, M.H. Rice, R.G. McQueen, and F.L. Yarger. Shock-wave compressions of twenty-seven metals. equations of state of metals. *Physical Review*, 108(2):196–216, 1957.

[53] G.T. Gray III, P.S. Follansbee, and C.E. Frantz. Effect of residual strain on the substructure development and mechanical response of shock-loaded copper. *Materials Science and Engineering: A*, 111(0):9 – 16, 1989.

[54] F. Llorca and F. Buy. Shock wave effects in copper: Design of an experimental device for post recovery mechanical testing. *AIP Conference Proceedings - Shock Compression of Condensed Matter - 2001*, pages 319 – 322, 2002.

[55] F. Llorca, F. Buy, and J. Farre. Experimental analysis of shock wave effects in copper. *AIP Conference Proceedings - Shock Compression of Condensed Matter - 2001*, pages 638–641, 2002.

[56] N. K. Bourne and G. T. Gray III. Computational design of recovery experiments for ductile metals. *Proceedings of the Royal Society A: Mathematical, Physical and Engineering Sciences*, 461(2062):3297–3312, 2005.

[57] N. K. Bourne and G. T. Gray III. Soft-recovery of shocked polymers and composites. *Journal of Physics D: Applied Physics*, 38(19):3690–3694, 2005.

[58] G. Raiser, R. J. Clifton, and M. Ortiz. A soft-recovery plate impact experiment for studying microcracking in ceramics. *Mechanics of Materials*, 10(1-2):43–58, 11/30 1990.

[59] T. Kurita, H. Matsumoto, K. Sakamoto, T. Shimada, T. Osada, K. Ojima, and H. Abe. Effects of shock compression on powder mixtures of nickel and boron. *Journal of Alloys and Compounds*, 396(1-2):133–138, 6/21 2005.

[60] P. J. Hazell, C. Beveridge, K. Groves, and G. Appleby-Thomas. The shock compression of microorganism-loaded broths and emulsions: Experiments and simulations. *International Journal of Impact Engineering*, 37(4):433–440, 2010.

[61] Z. Rosenberg, D. Yaziv, and Y. Partom. Calibration of foil-like manganin gauges in planar shock wave experiments. *Journal of Applied Physics*, 51(7):3702–3705, 1980.

[62] E. Barsis, E. Williams, and C. Skoog. Piezoresistivity coefficients in manganin. *Journal of Applied Physics*, 41(13):5155–5162, 1970.

[63] Z. Rosenberg and Y. Partom. Lateral stress measurement in shock-loaded targets with transverse piezoresistance gauges. *Journal of Applied Physics*, 58(8):3072–3076, 1985.

[64] Z. Rosenberg and N. S. Brar. The influence of the elasto-plastic properties of piezoresistance gauges on their loading-unloading characteristics as lateral shock stress transducers. *Journal of Applied Physics*, 77(4):1443–1448, 1995.

[65] J. C. F. Millett, N. K. Bourne, and Z. Rosenberg. On the analysis of transverse stress gauge data from shock loading experiments. *Journal of Physics D: Applied Physics*, 29(9):2466–2472, 1996.

[66] Z. Rosenberg and Y. Partom. The pressure dependence of the yield strength of shock-loaded manganin gauges. *Journal of Applied Physics*, 57(11):5084–5086, 1985.

[67] Ultrasonic transducer technical notes (pdf). Accessed from http://www.olympus-ims.com/en/knowledge/ on 13/02/2012.

[68] C. A. Sewry. Electron microscopy of human skeletal muscle: role in diagnosis. *Current Diagnostic Pathology*, 8(4):225–231, 8 2002.

[69] J. B. Harris and M. J. Cullen. Muscle necrosis caused by snake venoms and toxins. *Electron microscopy reviews*, 3(2):183–211, 1990.

[70] J. M. Gutierrez, V. Arce, F. Brenes, and F. Chaves. Changes in myofibrillar components after skeletal muscle necrosis induced by a myotoxin isolated from the venom of the snake bothrops asper. *Experimental and molecular pathology*, 52(1):25–36, 1990.

[71] A.R. Clarke and C.N. Eberhardt. *Microscopy Techniques for Materials Science*. Woodhead Publishing Limited, Abington Hall, Abington, Cambridge, England. CB1 6AH, 2002. ISNB: 1 85573 587 3.

[72] Vernon John. *Introduction to Engineering Materials*. PALGRAVE MACMILLAN - Houndmills, Basingstoke, Hampshire, England. RG21 6XS, 4th edition edition, 1972, 1983, 1992, 2003. ISBN: 0-333-94917-X.

[73] Peter J. Goodhew, John Humphreys, , and Richard Beanland. *Electon and Microscopy Analysis*. Taylor & Francis. 11 New Fetter Lane, London, England, EC4P 4EE, third edition edition, 2001. ISBN: 0 7484 0968 8.

[74] C.Y. Tham. Reinforced concrete perforation and penetration simulation using autodyn-3d. *Finite Elements in Analysis and Design*, 41(14):1401 – 1410, 2005.

[75] M.M. Dehghan Banadaki and B. Mohanty. Numerical simulation of stress wave induced fractures in rock. *International Journal of Impact Engineering*, 40 - 41(0):16 – 25, 2012.

[76] C.Y. Tham, V.B.C. Tan, and H.P. Lee. Ballistic impact of a kevlar helmet: Experiment and simulations. *International Journal of Impact Engineering*, 35(5):304 – 318, 2008.

[77] H.A. Ai and T.J. Ahrens. Simulation of dynamic response of granite: A numerical approach of shock-induced damage beneath impact craters. *International Journal of Impact Engineering*, 33:1 – 10, 2006.

[78] C.E. Anderson Jr. An overview of the theory of hydrocodes. *International Journal of Impact Engineering*, 5(1-4):33–59, 1987.

[79] J. D. Kemp, D. L. Gammon, W. G. Moody, and J. A. Jacobs. Effect of fresh ham quality on aged ham quality. *Journal of Anumal Science*, 27:366, 1968.

[80] L. R. Miller, V. A. Garwood, and M. D. Judge. Factors affecting porcine muscle fiber type, diameter and number. *Journal of animal science*, 41(1):66–77, July 1 1975.

[81] R. Sakata, T. Oshida, H. Morita, and Y. Nagata. Physico-chemical and processing quality of porcine m. longissimus dorsi frozen at different temperatures. *Meat Science*, 39(2):277–284, 1995.

[82] Y. Ono, M. B. Solomon, C. M. Evock-Clover, N. C. Steele, and K. Maruyama. Effects of porcine somatotropin administration on porcine muscles located within different regions of the body. *Journal of animal science*, 73(8):2282–2288, August 1 1995.

[83] S. M. Roth, G. F. Martel, F. M. Ivey, J. T. Lemmer, B. L. Tracy, D. E. Hurlbut, E. J. Metter, B. F. Hurley, and M. A. Rogers. Ultrastructural muscle damage in young vs. older men after high-volume, heavy-resistance strength training. *Journal of applied physiology*, 86(6):1833–1840, 1999.

[84] H. Zuckerman and M. B. Solomon. Ultrastructural changes in bovine longissimus muscle caused by the hydrodyne process. *Journal of Muscle Foods*, 9(4):419–426, 1998.

[85] C. Henssge, Huijun Wang, and B. Hoppe. Light microscopical investigations on structural changes of skeletal muscle as artifacts after postmortem stimulation. *Forensic science international*, 125(2-3):163–171, 2/18 2002.

[86] Craig D. Byron, Mark W. Hamrick, and Christopher J. Wingard. Alterations of temporalis muscle contractile force and histological content from the myostatin and mdx deficient mouse. *Archives of Oral Biology*, 51(5):396 – 405, 2006.

[87] M.D. Ayala, O. Lopez Albors, A. Blanco, A. Garcia Alcazar, E. Abellan, G. Ramirez Zarzosa, and F. Gil. Structural and ultrastructural changes on muscle tissue of sea bass, dicentrarchus labrax l., after cooking and freezing. *Aquaculture*, 250:215 – 231, 2005.

[88] T. Kolczak, E. Pospiech, K. Palka, and J. Lacki. Changes in structure of psoas major and minor and semitendinosus muscles of calves, heifers and cows during post-mortem ageing. *Meat Science*, 64(1):77–83, 2003.

[89] F. Fernandez-Martin, L. Otero, M. T. Solas, and P. D. Sanz. Protein denaturation and structural damage during high-pressure-shift freezing of porcine and bovine muscle. *Journal of Food Science*, 65(6):1002–1008, 2000.

[90] S.R. Ward and R.L. Lieber. Density and hydration of fresh and fixed human skeletal muscle. *Journal of Biomechanics*, 38(11):2317–2320, 2005.

[91] J. Mendez and A. Keys. Density and composition of mammalian muscle. *Metabolism*, 9:184–188, 1960.

[92] T. Koch, S. Lakshmanan, K. Raum, M. Wicke, D. Morlein, and S. Brand. Sound velocity and attenuation of porcine loin muscle, backfat and skin. volume 25 IFMBE, pages 96–99, 2009.

[93] A. Sarvazyan, A. Tatarinov, and N. Sarvazyan. Ultrasonic assessment of tissue hydration status. *Ultrasonics*, 43(8):661–671, 2005.

[94] H. Masugata, K. Mizushige, S. Senda, A. Kinoshita, H. Sakamoto, S. Sakamoto, and H. Matsuo. Relationship between myocardial tissue density measured by microgravimetry and sound speed measured by acoustic microscopy. *Ultrasound in Medicine and Biology*, 25(9):1459–1463, 1999.

[95] C. J. Shepherd, G. J. Appleby-Thomas, P. J. Hazell, and D. F. Allsop. The dynamic behaviour of ballistic gelatin. *AIP Conference Proceedings*, 1195:1399–1402, 2009.

[96] Frank M. White. Fluid mechanics - third edition. *McGRAW-HILL, INC., ISBN-10: 0072281928 (6th edition)*, 1994.

[97] Q. Xue, V.F. Nesterenko, and M.A. Meyers. Evaluation of the collapsing thick-walled cylinder technique for shear-band spacing. *International Journal of Impact Engineering*, 28(3):257–280, 2003.

[98] D.E. Eakins and N.N. Thadhani. Instrumented taylor anvil-on-rod impact tests for validating applicability of standard strength models to transient deformation states. *Journal of Applied Physics*, 100(7), 2006.

[99] G.J. Appleby-Thomas, P.J. Hazell, J.M. Wilgeroth, C.J. Shepherd, D.C. Wood, and A. Roberts. On the dynamic behavior of three readily available soft tissue simulants. *Journal of Applied Physics*, 109(8), 2011.

[100] L.M. Barker and R.E. Hollenbach. Shock-wave studies of pmma, fused silica, and sapphire. *Journal of Applied Physics*, 41(10):4208–4226, 1970.

[101] J.C.F. Millett and N.K. Bourne. The deviatoric response of polymethylmethacrylate to one-dimensional shock loading. *Journal of Applied Physics*, 88(12):7037–7040, 2000.

[102] Indium Corporation of America. Indium corporation of america. *http://www.indium.com/low-temperature-solders/ (Accessed on 07/07/2012)*, 2012.

[103] R. Pethig and D.B. Kell. The passive electrical properties of biological systems: Their significance in physiology, biophysics and biotechnology. *Physics in Medicine and Biology*, 32(8):933–970, 1987.

[104] A. Koji. Characterization of heterogeneous systems by dielectric spectroscopy. *Progress in Polymer Science*, 27(8):1617 – 1659, 2002.

[105] A. Di Biasio and C. Cametti. Effect of shape on the dielectric properties of biological cell suspensions. *Bioelectrochemistry*, 71(2):149 – 156, 2007.

[106] N. K. Bourne, G. T. Gray, and J. C. F. Millett. On the shock response of cubic metals. *Journal of Applied Physics*, 106(9), 2009.

[107] G. J. Appleby-Thomas, P. J. Hazell, and C. Stennett. The variation in lateral and longitudinal stress gauge response within an rtm 6 epoxy resin under one-dimensional shock loading. *Journal of Materials Science*, 44(22):6187–6198, 2009.

[108] G. J. Appleby-Thomas, P. J. Hazell, J. Millett, and N. K. Bourne. Deviatoric response of an armour-grade aluminium alloy. *AIP Conference Proceedings*, 1195:533–536, 2009.

[109] D.C. Wood, P.J. Hazell, G.J. Appleby-Thomas, and N.R. Barnes. Shock behaviour of a phenolic resin. *Journal of Materials Science*, 46(18):5991–5999, 2011.

[110] J. C. F. Millett, G. Whiteman, and N. K. Bourne. Lateral stress and shear strength behind the shock front in three face centered cubic metals. *Journal of Applied Physics*, 105(3), 2009.

[111] N. K. Bourne and Z. Rosenberg. On the ringing observed in shock-loaded piezoresistive stress gauges. *Measurement Science and Technology*, 8(5):570–573, 1997.

[112] K. Nagayama, Y. Mori, Y. Motegi, and M. Nakahara. Shock hugoniot compression data for several bio-related materials. *AIP Conference Proceedings*, 845 II:1547–1550, 2006.

[113] A. Delalleau, G. Josse, J. M Lagarde, H. Zahouani, and J. M Bergheau. Characterization of the mechanical properties of skin by inverse analysis combined with the indentation test. *Journal of Biomechanics*, 39(9):1603–1610, 2006. Cited By (since 1996): 3.

[114] J. J. Elsner and A. Gefen. Is obesity a risk factor for deep tissue injury in patients with spinal cord injury? *Journal of Biomechanics*, 41(16):3322–3331, 2008. Cited By (since 1996): 4.

[115] A. P. del Palomar, B. Calvo, J. Herrero, J. Lopez, and M. Doblar. A finite element model to accurately predict real deformations of the breast. *Medical Engineering and Physics*, 30(9):1089–1097, 2008.

[116] Cuiping Li, Nebojsa Duric, Peter Littrup, and Lianjie Huang. In vivo breast sound-speed imaging with ultrasound tomography. *Ultrasound in medicine & biology*, 35(10):1615–1628, 10 2009.

[117] Ho-Chul Shin, Richard Prager, Henry Gomersall, Nick Kingsbury, Graham Treece, and Andrew Gee. Estimation of speed of sound in dual-layered media using medical ultrasound image deconvolution. *Ultrasonics*, 50(7):716–725, 6 2010.

[118] D. N. Schmidt and M. W. Evans. Shock wave compression of 'plexiglas' in the 2.5 to 20 kilobar region. *Nature*, 206(4991):1348–1349, 1965.

[119] Jarlath Mc Hugh. *Ultrasound Technique for the Dynamic Mechanical Analysis (DMA) of Polymers*. PhD thesis, von der Fakultat III - Prozesswissenschaften der Technischen Universitat Berlin zur Erlangung des akademischen Grades, 2007. ISSN 1613-4249 ISBN 978-3-9812072-0-0.

[120] J.C.F. Millett, N.K. Bourne, Y.J.E. Meziere, R. Vignjevic, and A. Lukyanov. The effect of orientation on the shock response of a carbon fibre-epoxy composite. *Composites Science and Technology*, 67(15-16):3253–3260, 2007.

[121] L. Davison and R. A. Graham. Shock compression of solids. *Physics Reports*, 55(4):255–379, 1979.

[122] J. C. F. Millett and N. K. Bourne. The shock induced equation of state of three simple polymers. *Journal of Physics D: Applied Physics*, 37(20):2901–2907, 2004.

[123] N. K. Bourne, J. C. F. Millett, and S. G. Goveas. The shock response of polyoxymethylene and polyethylene. *Journal of Physics D: Applied Physics*, 40(18):5714–5718, 2007.

[124] R.E. Winter, G.D. Owen, and E.J. Harris. Experimental measurement of stress perturbations caused by lateral gauges. *Journal of Physics D: Applied Physics*, 41(20), 2008.

[125] J. C. F. Millett, G. T. Gray III, and N. K. Bourne. Measurement of the shear strength of pure tungsten during one-dimensional shock loading. *Journal of Applied Physics*, 101(3), 2007.

[126] J. C. F. Millett, G. Whiteman, S. M. Stirk, and N. K. Bourne. The shock induced shear strength in a silastomer. *Society for Experimental Mechanics - SEM Annual Conference and Exposition on Experimental and Applied Mechanics 2009*, 1:498–503, 2009.

[127] R. E. Winter and E. J. Harris. Simulations of embedded lateral stress gauge profiles in shocked targets. *Journal of Physics D: Applied Physics*, 41(3), 2008.

[128] C.J. Shepherd, G.J. Appleby-Thomas, J.M. Wilgeroth, P.J. Hazell, and D.F. Allsop. On the response of ballistic soap to one-dimensional shock loading. *International Journal of Impact Engineering*, 38(12):981–988, 2011.

[129] G.J. Appleby-Thomas, P.J. Hazell, J.M. Wilgeroth, C.J. Shepherd, D.C. Wood, and A. Roberts. On the dynamic behavior of three readily available soft tissue simulants. *Journal of Applied Physics*, 109(8), 2011.

[130] M.D. Furnish, G.T. Gray III, and J.F. Bingert. Line visar and post-shot metallography comparisons for spall analysis. volume 1, pages 351–352, 2011.

[131] W.F. Hemsing, A.R. Mathews, R.H. Warnes, and G.R. Whittemore. Visar: Line-imaging interferometer. volume 1346, pages 133–140, 1990.

[132] T.J. Vogler, W.M. Trott, W.D. Reinhart, C.S. Alexander, M.D. Furnish, M.D. Knudson, and L.C. Chhabildas. Using the line-visar to study multi-dimensional and mesoscale impact phenomena. *International Journal of Impact Engineering*, 35(12):1844–1852, 2008.

[133] J. M. Wilgeroth, P. J. Hazell, and G. J. Appleby-Thomas. The shock response of a rendered porcine fat. *Journal of Applied Physics*, 108(9), 2010.

[134] Wei Yang, Zhong-Ming Li, Wei Shi, Bang-Hu Xie, and Ming-Bo Yang. Review on auxetic materials. *Journal of Materials Science*, 39:3269–3279, 2004.

[135] Yunan Prawoto. Seeing auxetic materials from the mechanics point of view: A structural review on the negative poisson's ratio. *Computational Materials Science*, 58(0):140 – 153, 2012.

[136] K.L. Alderson, A.P. Pickles, P.J. Neale, and K.E. Evans. Auxetic polyethylene: The effect of a negative poisson's ratio on hardness. *Acta Metallurgica et Materialia*, 42(7):2261 – 2266, 1994.

[137] K.A. Brown, C. Bo, S.D. Masouros, A. Ramasamy, N. Newell, T.J. Bonner, J. Balzer, A.M. Hill, J.C. Clasper, A.M.J. Bull, and W.G. Proud. Prospects for studying how high-intensity compression waves cause damage in human blast injuries. volume 1426, pages 131–134, 2012.

[138] I.M.J. Mackenzie and B. Tunnicliffe. Blast injuries to the lung: Epidemiology and management. *Philosophical Transactions of the Royal Society B: Biological Sciences*, 366(1562):295–299, 2011.